LA-UR-20-22665
Approved for public release; distribution is unlimited.

Title: Discrete Fracture Network Modeling to Estimate Upscaled Parameters for the Topopah Spring, Lava Flow, and Tiva Canyon Aquifers at Pahute Mesa, Nevada National Security Site

Author(s): Makedonska, Nataliia
Kwicklis, Edward Michael
Hyman, Jeffrey De'Haven
Bourret, Suzanne Michelle

Intended for: Report

Issued: 2020-05-19 (rev.1)

LA-UR-20-22665

Discrete Fracture Network Modeling to Estimate Upscaled Parameters for the Topopah Spring, Lava Flow, and Tiva Canyon Aquifers at Pahute Mesa, Nevada National Security Site

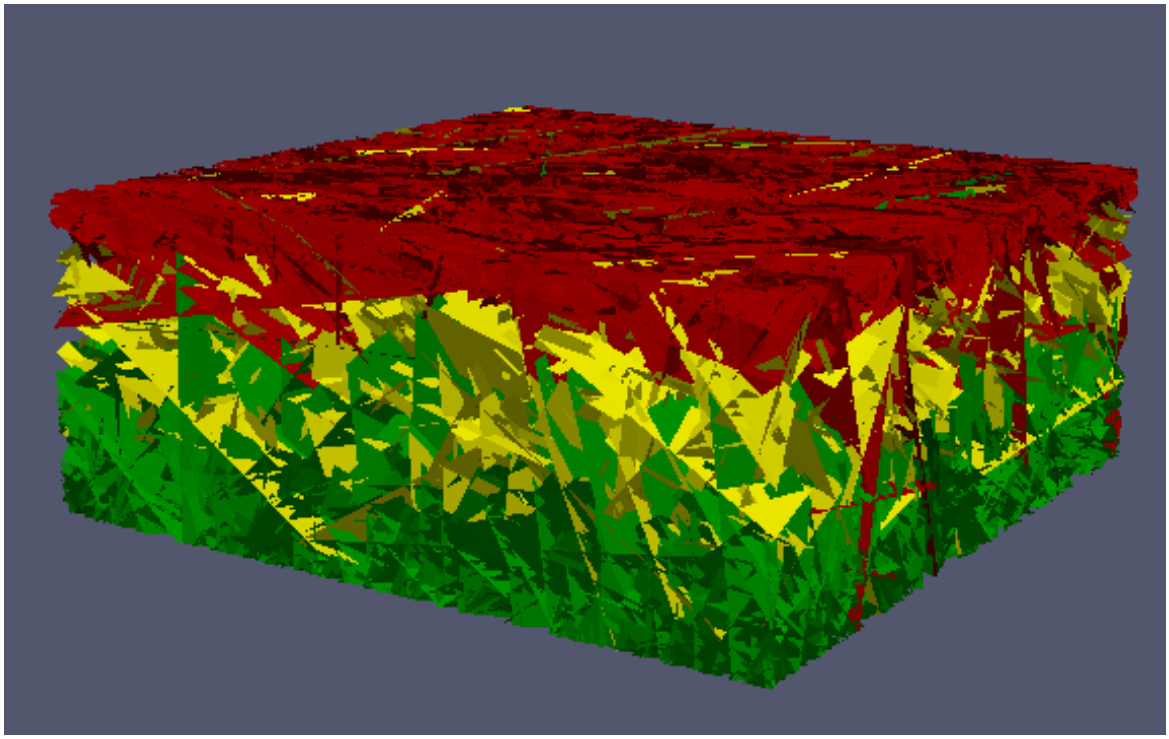

Nataliia Makedonska, Edward Kwicklis, Jeffrey D. Hyman, and Michelle Bourret

Los Alamos National Laboratory

May 2020

This page intentionally left blank.

CONTENTS

Figure Captions

Table Captions

ABSTRACT

This report describes the results of Discrete Fracture Network (DFN) simulations for the Topopah Spring Aquifer (TSA), Lava Flow Aquifer, and Tiva Canyon Aquifer (TCA), at Pahute Mesa on the Nevada National Security Site (NNSS), formerly the Nevada Test Site. The research focuses on calculating upscaled groundwater flow and contaminant transport parameters using DFNs generated according to fracture characteristics observed in the TSA, LFA and TCA at Pahute Mesa. The highly fractured and heterogeneous nature of these aquifers makes them candidates for stochastic DFN modeling of radionuclide transport on a small scale with subsequent upscaling. One hundred independent DFN realizations are generated for each aquifer, and the upscaled parameters for continuum simulations of subsurface flow and transport in fractured media at Pahute Mesa are calculated. Our goal is to implement a modeling approach that can translate parameters to larger-scale models that account for local-scale flow and transport processes, such as channelization of flow and transport along a few well connected, large fractures. Additionally, to simulate advective and advective-diffusive transport through the fracture networks, the Time Domain Random Walk (TDRW) approach is applied to account for matrix diffusion into a finite half-space. Moreover, a novel approach to calculate dynamic (active) fracture surface area to reflect flow channeling is implemented. This work will improve the representation of radionuclide transport processes in large-scale, regulatory-focused models by providing estimates of hard-to-measure flow and contaminant transport parameters at large scales.

In this report, we (1) show recent results of flow and transport simulations on multiple DFN realizations of the TSA, LFA, TCA; (2) discuss the resulting distributions of estimated upscaled parameters; (3) describe the estimation of upscaled parameters for an equivalent parallel-plate continuum model and (4) present a comparison between simulated transport from the equivalent continuum model and an actual DFN.

1 INTRODUCTION

Discrete fracture network (DFN) modeling is being used by the Underground Test Area (UGTA) project to investigate contaminant transport in fractured aquifers at Pahute Mesa on the Nevada National Security Site (NNSS), formerly known as the Nevada Test Site (NTS). Pahute Mesa was the location of 85 underground nuclear tests between 1965 and 1992, many of which were large-yield, deeply buried tests that released radionuclides directly into the groundwater [Laczniack et al.,1996]. Hydraulic gradients measured in wells at and south of Pahute Mesa indicate that groundwater moves south-southwest out of the testing areas toward Oasis Valley (Fenelon et al., 2016). The saturated-zone hydrostratigraphy at Pahute Mesa includes fractured welded tuff and lava flow aquifers, which alternate with low permeability zeolitic confining units (NSTec, 2014). The fractured welded tuff and lava flow aquifers are suspected to be the dominant transport pathways for radionuclides leaving the testing areas. These hydrostratigraphic units (HSUs) are offset across north-south trending normal faults, northwest trending structural zones, and arcuate caldera boundaries, each of which may also affect large-scale flow and transport patterns.

The recently developed computational suite *dfnWorks* [Hyman et al., 2015a] is used to model steady-state, fully-saturated flow, and particle movement through a DFN. In the *dfnWorks* model, planar objects randomly placed in a three-dimensional domain intersect each other to represent fracture networks. Fractures are statistically assigned their size, shape, location, orientation, and aperture based on site-specific data from Pahute Mesa. The generation of fractures is performed via the FRAM algorithm, described in detail in [Hyman et al., 2014]. These fractures are subsequently used to generate a high-quality computational mesh with LaGriT [LaGriT, 2013]. The control volume cells are formed based on Delaunay triangulations. The highly-parallel, multiphysics code, PFLOTRAN [Lichtner et al., 2015], is used as the control volume solver to obtain the steady-state flow solution with applied pressure boundary conditions. The Lagrangian particle tracking model *dfnTrans* [Makedonska et al., 2015] is applied to simulate advective transport through three-dimensional DFNs. A package of Python codes was developed for post-processing the transport results and calculating upscaled parameters. The workflow of *dfnWorks* is briefly described in Section 2. We refer the reader to [Hyman et al., 2015a] for further details of the *dfnWorks* software. *dfnWorks* has been applied to a number of different subsurface flow and transport studies. For example, a one-km^3 DFN was generated according to the fractured rock characteristics of the proposed nuclear repository site in Forsmark, Sweden [SKB, 2011]. The effect of particle injection mode on transport properties in the large-scale DFN was studied in Hyman et al, [2015b]. Moreover, we are able to model in-fracture variability of aperture and transmissivity in each individual fracture in a network of thousands of fractures [Makedonska et al, 2016]. *dfnWorks* also was applied to CO_2 sequestration problems to estimate the potential leakage from CO_2 subsurface storage operations [Makedonska et al., 2018b; Hyman et al., 2020].

Our earlier progress report [Makedonska et al., 2018c] shows preliminary results of using *dfnWorks* for flow and transport modeling at Pahute Mesa. Appendix A in Makedonska et al. (2018c) shows successful verification of the *dfnWorks* results with analytical results on a simple DFN with parallel fractures. As described in Makedonska et al (2018c), generating large scale DFNs according to field observation data brings computational challenges, such as the large number of cells in the computational grid and an unreasonably high computational runtime. In order to overcome those difficulties, the analysis on the role of small fractures on simulated advective transport was performed [Appendix B in Makedonska et al., 2018c]. We found that eliminating fractures with a length less than three meters doesn't significantly

change the original fracture network intensity and has no effect on 50% of transport breakthrough. The analysis described in this report is based on a slightly sparser network than initially prescribed in Golder Associates (2014; 2015) that allows us to generate hundreds of DFN realizations with nearly as high an intensity in reasonable computational time.

In the current study, *dfnWorks* software is used to model fracture networks observed at Pahute Mesa in the Topopah Spring Aquifer (TSA), the Lava Flow Aquifer (LFA), and the Tiva Canyon Aquifer (TCA). Fractures are generated according to fracture characteristics data provided by *Golder Associates (2014; 2015)*, that describe parameter distributions for fracture orientations and length, network intensities P_{32} (the ratio between the total fracture area and the volume of the simulation domain), and fracture conductive characteristics, such as aperture and transmissivity. These parameters are presented in Appendix L of NSTec (2014) and in Golder Associates (2014; 2015).

One-hundred DFN realizations of each of these aquifers at Pahute Mesa were generated and flow and transport simulations allowed us to develop probability distributions of upscaled parameters, such as effective permeability, volumetric and transport porosity ,and longitudinal dispersivity in different flow directions: East – West, North – South, and Top-Bottom.

This work is intended to improve the representation of radionuclide transport processes in large-scale, regulatory-focused models with the goal of reducing pessimistic bounding approximations and providing contaminant transport parameters that capture the behavior of contaminant movement through fracture networks developed from field observations. Our goal is to develop a modeling approach that can translate parameters to larger-scale models that account for local-scale flow and transport processes. In order to meet the goal, we have developed a new approach based on the concept of dynamic fracture network intensity to calculate estimates of effective fracture spacing and fracture aperture that can be used in an equivalent continuum models with fracture/matrix diffusion based on equivalent parallel plate assumptions. The first tests of the upscaling approach for the equivalent continuum models is presented in the current report.

The current report is organized as following. Section 2 gives a brief description of our DFN modeling tool, *dfnWorks*. The fracture network characteristics of TSA, LFA, and TCA aquifers at Pahute Mesa with short explanation of geological specifics are presented in Section 3. The methodology used to simulate subsurface flow and transport on DFNs, calculation of upscaled parameters in full DFN and equivalent parallel plate DFN model is described in Section 4. Section 5 shows a comparison between an equivalent continuum model with upscaled parameters from the DFN and actual particle breakthrough from the DFN, both with and without the effects of matrix diffusion. Section 6 presents a discussion of results of our upscaled parameters and shows a comparison of our results with parameters calibrated by the Navarro team using a one-dimensional, equivalent dual-continuum model that was calibrated against field-scale ^3H observations at Pahute Mesa. In Section 7, the main findings are summarized and future steps are discussed.

2 COMPUTATIONAL SUITE FOR MODELING FLOW AND TRANSPORT IN 3-D DISCRETE FRACTURE NETWORKS, *dfnWorks*

An overview of the entire *dfnWorks* workflow is illustrated in Figure 1 (corresponds to Fig. 2 in Hyman et al., 2015a). The workflow has three principal pieces, *dfnGen*, *dfnFlow*, *dfnTrans*, for generating the fracture network and corresponding computational mesh, simulating flow fields, and simulating particle transport through the network, respectively. Each of these pieces consists of three primary workflow steps as described below. The inputs for *dfnWorks* are the site fracture characteristics which include distributions of fracture orientations, radii, and spatial locations.

dfnGen: DFN construction and mesh generation

- FRAM [Hyman et al., 2014] – Using the site fracture characteristics, DFNs are constructed using the feature rejection algorithm for meshing (FRAM). In FRAM, each DFN is constructed so that all features in the network (e.g., the length of intersections between fractures and the distance between lines of intersection of a fracture) are larger than a user-defined minimum length scale. This restriction provides a firm lower bound on the required mesh resolution, and special care is taken so that prescribed fracture statistics are not affected by this restriction. Also, all isolated fractures from the network are removed because isolated fractures do not contribute to flow and transport across the network, and their inclusion adds unused computational cells to the mesh.
- LaGriT – The LaGriT meshing toolbox is used to create a conforming Delaunay triangulation of the fracture network.

dfnFlow: Flow Field Simulation

- The first step is to reformat the mesh geometric information into control-volume information suitable for input to PFLOTRAN.
- Next, the steady-state pressure solution in the DFN is obtained using PFLOTRAN [Lichtner et al., 2015].

dfnTrans: Transport Simulation

- The Darcy fluxes obtained using *dfnFlow* are used to reconstruct the local velocity field, which is used for particle tracking on the DFN.
- Lagrangian transport simulation (particle tracking) is then performed an extension of the WalkAbout method [Painter et al., 2012] to determine pathlines through the network and simulate transport. It is important to note that *dfnTrans* originally only solved for advective transport. However, as part of this study, a Time Domain Random Walk (TDRW) approach was added to *dfnTrans* to account for matrix diffusion.
- The package of python scripts was developed to post-process the transport simulation results and to estimate upscaled parameters: effective permeability, volumetric and transport porosities, longitudinal dispersivity, dynamic fracture network intensity, and fracture spacing and aperture for reduced order DFN simulations.

Communication between the different pieces of the *dfnWorks* workflow is carried out using files that allow for restarts between the different modules of the code. Various Python scripts are used to format the output from one stage of the workflow into the required input format of the next stage. Coupling between the pieces of the workflow is fully automated and does not require user actions. One of the key features of dfnWorks is that it combines existing software, e.g., LaGriT and PFLOTRAN, in a novel workflow. The primary benefits of this choice are that the combined codes have already been optimized with respect to their efficiency, and that verification and validation have already been performed and documented [Hyman et al., 2015a].

Verification of the workflow for flow and contaminant transport modeling using *dfnWork*s is presented in [Appendix A, Makedonska et al., 2018c]. In the first test, the simple DFN, which contains of 10 parallel fractures, is generated followed by flow and transport simulations. The results are compared with analytical solutions. The DFN in the second test includes two sets of fractures, orthogonal to each other. The role of fracture intersections on advective transport through fracture networks is shown and upscaled parameters are calculated.

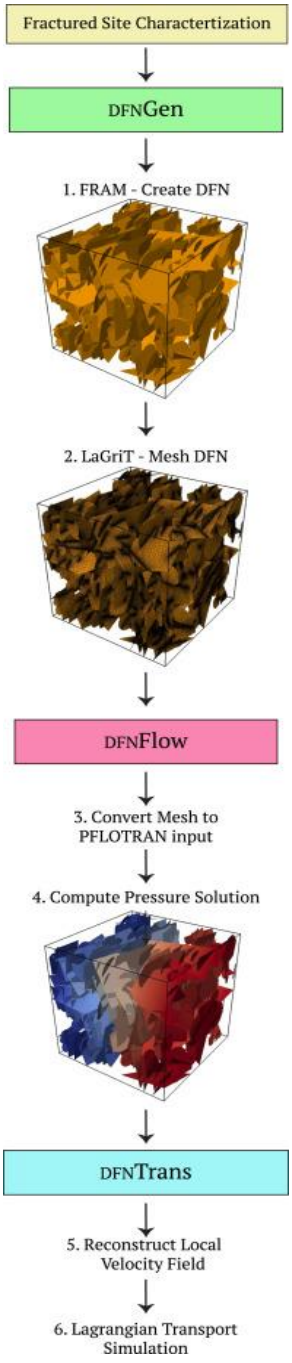

Figure 1 dfnWorks Workflow

3 CHARACTERISTICS OF FRACTURE NETWORKS IN AQUIFERS AT PAHUTE MESA

The Golder Associates team provided the statistical data for fracture characteristics obtained from field observations of the TSA, LFA and TCA [Golder Associates, 2014; NSTec, 2014 (Appendix L); Golder associates, 2015]. The aquifers at Pahute Mesa are densely fractured and highly heterogeneous. Multiple welding zones are identified within the different aquifers, with each welding zone containing several sets of cooling joints (CJ) and sets of tectonic (T1 & T2) fractures that cross-cut the welding zones. The DFN models for each aquifer at Pahute Mesa are constructed individually and their fracture characteristics are described below.

3.1 Topopah Spring Aquifer (TSA)

The TSA is made up of multiple welding zones, including: (1) a thick, moderately to densely welded central zone (DWZ) (indicated by extreme flattening of pumice and lithic fragments within the ash deposit); (2) a thinner, upper partially welded zone (PWZu); and (3) a lower partially welded zone (PWZl) (Figure 2). Because the Hydrostratigraphic Framework Model (HFM) for Pahute Mesa (NSTec, 2014) does not differentiate between the moderately to densely welded and partially-welded zones within the TSA, the three welding zones are considered together in the DFN models of the TSA to investigate its composite behavior. The proportion of the moderately to densely welded central zone tends to increase with overall thickness of the TSA, with the partially welded margins becoming more dominant where the TSA is thinnest. Where present, the TSA has been observed to vary in thickness between 20 m and 100 m. In this study, we use the maximum observed thickness of 100 m, so that the moderately-to-densely welded central zone has a thickness of 60 m, and the upper and lower partially welded zones have thicknesses of 10 m and 30 m. Each welding zone is characterized by the same five fracture sets (three sets of cooling joints and two sets of tectonic fractures). Fracture orientations are similar in each welding zone. The primary difference between zones is in fracture intensity, with the partially welded upper and lower zones having lower intensity of cooling joints (CJ1, CJ2 and CJ3) which are assumed not to extend beyond the welding unit boundaries. In contrast, tectonic fracture sets (T1 and T2) are able to cross welding zone boundaries and thus form the principal pathways for flow between welding zones. The fracture characteristic data used as input for the DFN modeling of the TSA are shown in Table 1. We refer to our previous report publication (Makedonska et al., 2018c) for a detailed description of the fracture parameters and how they are being applied to the fracture network generation.

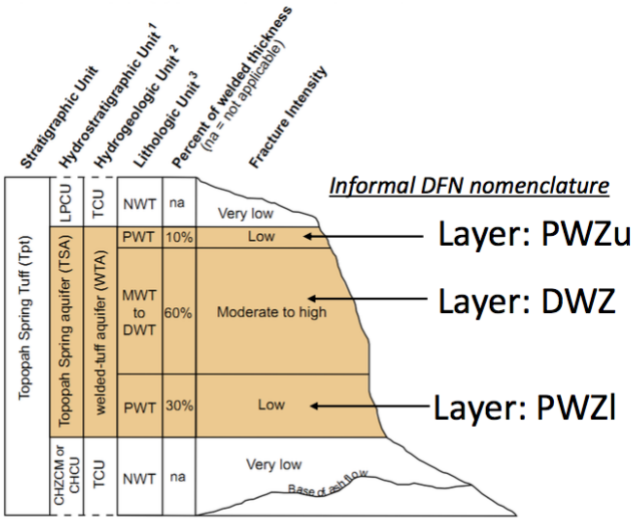

Figure 2 **Conceptual model for fracture facies / cooling sub-units within the Topopah Springs Aquifer (TSA) HSU (from Golder Associates, 2014). [PWZu - upper partially-welded zone; DWZ – central densely-welded zone; PWZl – lower partially-welded zone]**

Table 1
Statistical parameters of TSA fracture network used for DFN modeling

Orientation and probability model for cooling joints and tectonic joints (Table 7 of NSTec (2014))							
HSU ID	**CSU ID**	**Fracture Set**	**Probabilistic Distribution**	**Mean Pole (°)**		**Fisher Concentration**	
				Trend	**Plunge**	**K**	
TSA	All	CJ1	Univariate Fisher*	95.47	23.32	25.78	
TSA	All	CJ2	Univariate Fisher	1.42	26.81	32.0	
TSA	All	CJ3	Univariate Fisher	9.52	80.82	10.37	
TSA	All	T1	Univariate Fisher	135.16	21.76	29.04	
TSA	All	T2	Univariate Fisher	43.04	29.55	30.75	
Size model for cooling joints and tectonic fractures (Table 3 of Golder Associates (2014))							
HSU ID	**CSU ID**	**Fracture Set**	**Probability Distribution**	**Parameter Names**	**Distribution Parameters**	**Size Truncation**	**Aspect Ratio**
TSA	All	CJ1	Unit Thickness		n/a	n/a	5
TSA	All	CJ2	Unit Thickness		n/a	n/a	5
TSA	All	CJ3	Exponential	Mean	3.373	Min = 1 m	1
TSA	All	T1	Power Law	k_r, r_0	2.6, 1	Min = 1m, Max = 250 m	5
TSA	All	T2	Power Law	k_r, r_0	2.01, 1	Min = 1m, Max = 250 m	5

Alternative size model for cooling joints based on outcrops of similar welded tuff units (Table 4 of Golder Associates (2014))							
HSU ID	**CSU ID**	**Fracture Set**	**Probability Distribution**	**Parameter Names**	**Distribution Parameters**	**Size Truncation**	**Aspect Ratio**
TSA	All	CJ1	Lognormal	Mean, Std. Dev.	1.250, 0.877	Min = 1 m, Max = CSU thickness	5
TSA	All	CJ2	Lognormal	Mean, Std. Dev.	1.250, 0.877	Min = 1 m, Max = CSU thickness	5
TSA	All	CJ3	Exponential	Mean	3.373	Min = 1 m	1
Fracture intensity models as a function of HSU and CSU (Table 5 of Golder Associates (2014))							
HSU ID	**CSU ID**	**Fracture Set**	**Probability Distribution**	**A****	**B****	**P_{32}****	
TSA	PWZu	CJ1	Exponential	5.000	0.150	1.11565	
TSA	PWZu	CJ2	Use CJ1 fit				
TSA	PWZu	CJ3	Use CJ3 from PWZl fit				
TSA	PWZu	T1	Use T1 from PWZl fit				
TSA	PWZu	T2	Exponential	0.300	0.050	0.18195	
TSA	DWZ	CJ1	Exponential	0.080	0.022	0.02137	
TSA	DWZ	CJ2	Exponential	1.000	0.060	0.02732	
TSA	DWZ	CJ3	Exponential	0.500	0.035	0.06122	
TSA	DWZ	T1	Exponential	1.000	0.025	0.22313	
TSA	DWZ	T2	Exponential	0.009	0.021	0.002552	
TSA	PWZl	CJ1	Exponential	3.000	0.050	0.66939	
TSA	PWZl	CJ2	Exponential	1.000	0.070	0.122456	
TSA	PWZl	CJ3	Exponential	0.500	0.050	0.111565	
TSA	PWZl	T1	Exponential	0.500	0.050	0.111565	
TSA	PWZl	T2	Exponential	0.400	0.380	0.12792	

Note: Data in Table 1 are from the original reference, Golder Associates (2014). The terms HSU and CSU refer to the Hydrostratigraphic Unit (in this case the TSA) and the Cooling Stratigraphic Unit; the fracture sets include three sets of cooling joints (CJ1, CJ2 and CJ3) and two sets of tectonic joints (T1 and T2).

* Univariate Fisher distribution [Fisher, 1953] is a noncentral hypergeometric distribution.

** Fracture network intensity within each CSU is an exponential function, calibrated to well data and correlated to the thickness of the unit: $P_{32}=A*\exp^{(-B*Thickness)}$ [Golder Associates, 2014].

3.2 Lava Flow Aquifer (LFA)

In lava flow aquifers (LFA), fracture intensity is a function of fracture facies (stratigraphic intervals with unique fracture geometric characteristics), which in turn is a function of the rate of cooling (Figure 3). Within the specific hydrostratigraphic units encountered at Pahute Mesa, the lava flow aquifers have been divided into four textural facies (cooling sub-units, abbreviated CSU): a highly fractured stoney lava center (SL) surrounded by upper and lower vitrophyric layers (UV, LV), and

underlain at its base by a rapidly-cooled flow breccia (FB) [Golder Associates, 2015]. The DFN input parameters for each layer at LFA are listed in Table 2.

For lava-flow aquifers, it was determined that the Bottom Surface Reference Frame (BSRF) model was the most appropriate model for describing fracture orientations. The following fracture sets were defined in LFAs [NSTec, 2014]:

- DP: (Bedding or Bottom Surface) Dip azimuth-parallel fractures
- SP: Bedding strike azimuth parallel fracture set
- BP: Bedding dip subparallel fracture set
- T1: First tectonic set, NNE to NE-striking
- T2: Second tectonic set, WNW to NW-striking

The implication of the conceptual model is that fluid flow is likely to occur primarily within cooling joints, shrinkage cracks, and sheet joints within the dense stony lavas and vitrophyric layers of a lava flow. The basal flow breccias and pumiceous lavas at the top and bottom of the flow, in combination with the bedded tuffs of the overlying and underlying tuff confining units (TCU), act as confining units in each lava flow. However, at Pahute Mesa, the tuff units may act as aquifers or confining units based on the degree of alteration and secondary mineralization. Connectivity between lava flows and thick confining units are likely to occur only through tectonic fractures and small faults large enough to cross-cut entire flows; these types of structures are thought to be rare at Pahute Mesa [Golder Associates, 2015].

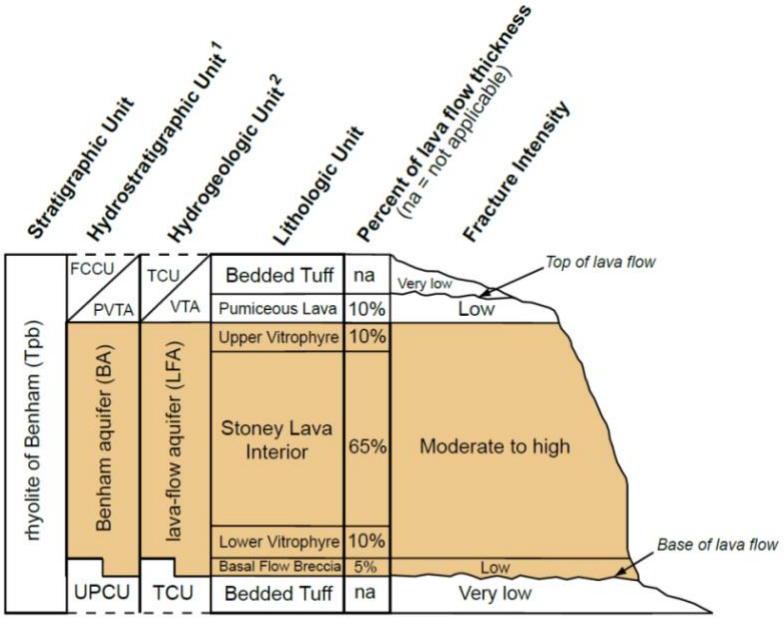

Figure 3 Conceptual model for fracture facies and lithofacies within a typical Lava Flow aquifer (LFA) at Pahute Mesa, from [Golder Associates, 2015].

Table 2

Statistical parameters of LFA fracture network used for DFN modeling

Orientation and probability model for cooling joints and tectonic joints (Table 1 of Golder Associates (2015))						
HSU ID	**CSU ID**	**Fracture Set**	**Probabilistic Distribution**	**Mean Pole (°)**		**Fisher Concentration**
				Trend	**Plunge**	**K**
LFA	All	SP	Univariate Fisher	89.12	27.32	18.34
LFA	All	DP	Univariate Fisher	350.48	28.06	26.24
LFA	All	BP	Univariate Fisher	19.39	53.21	35.0
LFA	All	T1	Univariate Fisher	319.06	18.73	35.0
LFA	All	T2	Univariate Fisher	48.39	7.85	35.0

Size model for cooling joints and tectonic fractures (Table 2 of Golder Associates (2015))							
HSU ID	**CSU ID**	**Fracture Set**	**Probability Distribution**	**Parameter Names**	**Distribution Parameters**	**Size Truncation**	**Aspect Ratio**
LFA	All	SP	Unit Thickness		n/a	n/a	0.2
LFA	All	DP	Unit Thickness		n/a	n/a	0.2
LFA	All	CJ3	Exponential	Mean	3.373	Min = 1 m	1
LFA	All	BP	Power Law	k_r, r_0	2.6, 1	Min = 1m, Max = 250 m	5
LFA	All	T2	Power Law	k_r, r_0	2.01, 1	Min = 1m, Max = 250 m	5

Fracture intensity models as a function of HSU and CSU (Table 3 & Table 4 of Golder Associates (2015))							
HSU ID	**CSU ID**	**Fracture Set**	**Mean P_{32}**	**A**	**B**	Relative Set Intensity (%)	**P_{32}**
LFA	UV	SP	0.8841	2.5	0.0067	50 %	0.44205
LFA	UV	DP	0.8841	2.5	0.0067	13 %	0.1149
LFA	UV	BP	0.8841	2.5	0.0067	4 %	0.03536
LFA	UV	T1	0.8841	2.5	0.0067	32 %	0.2829
LFA	UV	T2	0.8841	2.5	0.0067	1 %	0.08841
LFA	SL	SP	0.4459	2.0	0.016	50 %	0.2225
LFA	SL	DP	0.4459	2.0	0.016	13 %	0.05796
LFA	SL	BP	0.4459	2.0	0.016	4 %	0.01783
LFA	SL	T1	0.4459	2.0	0.016	32 %	0.14268

LFA	SL	T2	0.4459	2.0	0.016	1 %	0.04459
LFA	LV	SP	0.3508	1.5	0.1	50 %	0.1754
LFA	LV	DP	0.3508	1.5	0.1	13 %	0.0456
LFA	LV	BP	0.3508	1.5	0.1	4 %	0.01403
LFA	LV	T1	0.3508	1.5	0.1	32 %	0.112256
LFA	LV	T2	0.3508	1.5	0.1	1 %	0.03508
LFA	BFB	ALL	0.0005	0.0005	0.0005	N/A	0.0005

3.3 Tiva Canyon Aquifer (TCA)

As in the TSA, the conceptual model for fracturing within the Tiva Canyon Aquifer (TCA) postulates that fracture intensity is a function of the cooling rate. The TCA at Pahute Mesa also contains lithophysae-rich zones. Lithophysae are bubblelike voids found in tuffs that are formed due to de-gassing of the still molten lava. While there are few published studies of the effects of lithophysae on fracture initiation, growth, and persistence, the presence of lithophysae in tuffs appear to have several effects on the growth and propagation of fractures [NSTec, 2014], including:

- Strain accommodation by deformation of lithophysae means that lithophysae-rich welded tuff aquifers (WTAs) are generally less fractured than non-lithophysal WTAs. Exposures of the TSA at Yucca Mountain (Sweetkind and Williams-Stroud, 1996) support this hypothesis;

- Lithophysae influence on the orientation and direction of new fractures, based on stress-intensity concentrations around irregularly-shaped lithophysae; and

- Lithophysae arrest the growth of cooling joints and propagation of tectonic joints resulting in fewer through-going fractures compared to zones without lithophysae.

The result is a conceptual model for fracturing within the TCA that features reduced fracture intensity in the densely welded core of the tuff when it is lithophysal. Cooling structures are concentrated in the upper and lower portions of the flow (“cooling sub-units”), termed the Upper Highly Fractured Layer (UHFL) and Lower Highly Fractured Layer (LHFL). The assumption is that the majority of the fractures in the Sparsely Fractured Center Layer (SFCL) of the TCA are tectonic in nature, not cooling-related. This conceptual model (Figure 4) is supported by surface outcrop observations and observed fracture densities in image logs [NSTec, 2014]. The TCA is divided into three cooling sub-units:

- Upper Highly Fractured Layer (UHFL): Assigned as 12% of total TCA thickness

- Sparsely Fractured Center Layer (SFCL): Assigned as 58% of total TCA thickness

- Lower Highly Fractured Layer (LHFL): Assigned as 30% of total TCA thickness

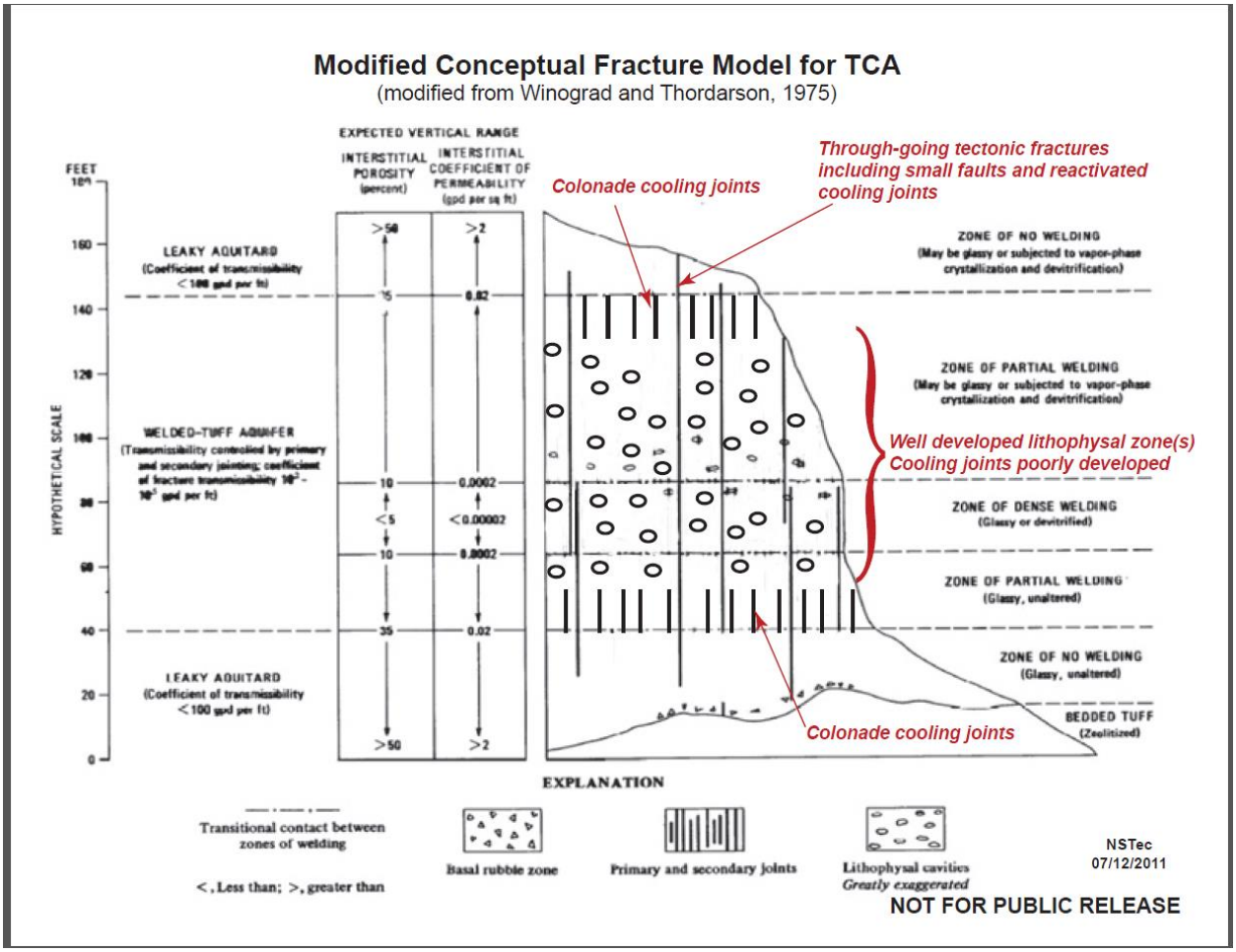

Figure 4 Schematic basic conceptual model for TCA.

The input DFN parameters for TCA are presented in Table 3.

Table 3
Statistical parameters of TCA fracture network used for DFN modeling

Orientation and probability model for cooling joints and tectonic joints (Table 7 of NSTec (2014))						
HSU ID	**CSU ID**	**Fracture Set**	**Probabilistic Distribution**	**Mean Pole (°)**		**Fisher Concentration**
				Trend	**Plunge**	**K**
TCA	All	CJ1	Univariate Fisher	87.89	25.94	25.4
TCA	All	CJ2	Univariate Fisher	179.32	32.42	40.3
TCA	All	CJ3	Univariate Fisher	354.73	67.68	19.18
TCA	All	T1	Univariate Fisher	126.43	67.68	19.18

TCA	All	T2	Univariate Fisher		44.61	12.2	9.92
Size model for cooling joints and tectonic fractures (Table 13 of NSTec (2014))							
HSU ID	**CSU ID**	**Fracture Set**	**Probability Distribution**	**Parameter Names**	**Distribution Parameters**	**Size Truncation**	**Aspect Ratio**
TCA	All	CJ1	Unit Thickness		n/a	n/a	5
TCA	All	CJ2	Unit Thickness		n/a	n/a	5
TCA	All	CJ3	Exponential	Mean	3.373	Min = 1 m	1
TCA	All	T1	Power Law	k_r, r_0	2.6, 1	Min = 1m, Max = 250 m	5
TCA	All	T2	Power Law	k_r, r_0	2.01, 1	Min = 1m, Max = 250 m	5
Alternative size model for cooling joints based on outcrops of similar welded tuff units (NSTec (2014))							
HSU ID	**CSU ID**	**Fracture Set**	**Probability Distribution**	**Parameter Names**	**Distribution Parameters**	**Size Truncation**	**Aspect Ratio**
TCA	All	CJ1	Lognormal	Mean, Std. Dev.	1.250, 0.877	Min = 1 m, Max = CSU thickness	5
TCA	All	CJ2	Lognormal	Mean, Std. Dev.	1.250, 0.877	Min = 1 m, Max = CSU thickness	5
Fracture intensity models as a function of HSU and CSU (Table 17 of NSTec (2014))							
HSU ID	**CSU ID**	**Fracture Set**	**Probability Distribution**	**A**	**B**		**P_{32}**
TCA	UHFL	CJ1	Exponential	0.500	0.090		0.12962
TCA	UHFL	CJ3	Exponential	0.500	0.140		0.061228
TCA	UHFL	T1	Exponential	0.500	0.080		0.15
TCA	UHFL	T2	Exponential	0.500	0.090		0.12962
TCA	SFCL	CJ1	Exponential	0.400	0.025		0.10113
TCA	SFCL	CJ2	Exponential	0.275	0.019		0.096715
TCA	SFCL	CJ3	Exponential	0.400	0.015		0.175294
TCA	SFCL	T1	Exponential	0.600	0.015		0.26294
TCA	SFCL	T2	Exponential	0.200	0.020		0.06657
TCA	LHFL	CJ1	Exponential	0.300	0.030		0.12197
TCA	LHFL	CJ2	Exponential	5.000	0.060		0.82649
TCA	LHFL	CJ3	Exponential	5.000	0.085		0.39
TCA	LHFL	T1	Exponential	0.500	0.050		0.111565
TCA	LHFL	T2	Exponential	0.300	0.045		0.077772

3.4 Challenges in DFN Generation

Information for the fracture characteristics (Table 1- Table 3) is required to generate fracture networks: statistical parameters of fracture length distribution, statistical parameters of fracture orientation

distribution, and fracture intensity. The subsurface media at Pahute Mesa is very fractured. The statistical data, obtained from field observations [Golder Associates, 2014; NSTec, 2014; Golder Associates, 2015] indicates high fracture network intensity. The fracture network intensity, P_{32}, is defined as a ratio of total fracture area to volume of the considered simulation domain, $P_{32} = \frac{\sum_{i=1,..,N} A_i}{V} \left[\frac{m^2}{m^3}\right]$. High DFN intensity leads to high number of fractures, which creates difficulties in computational modeling by increasing number of control volume cells. In order to overcome the computational limits, the analysis of role of the fractures with the length of 1 to 3 m on statistical distributions and simulated breakthrough curves was performed and described in our previous study [Makedonska et al., 2018c]. The analysis shows that, in general, the generated DFNs honor the statistical parameters of fractures length of the classes of distribution types, and that, visually, distributions generated assuming both the 1-m and 3-m minimum fractures length are similar to both the analytical distributions and to each other. The fractures at or below the minimum length were eliminated when generating the DFNs of TSA, LFA and TCA at Pahute Mesa. The DFNs with the following attributes are obtained from the resulting stochastic realizations, where the simulation domain size is 250 x 250 x 100 m^3:

- TSA (Figure 5):
    - Approximately 16,000 fractures
    - Approximately 40,000,000 computational cells
    - The minimum fracture length is 3 meters
- LFA (Figure 6):
    - Approximately 13,000 fractures
    - Approximately 35,000,000 computational cells
    - The minimum fracture length is 2 meters
- TCA (Figure 7):
    - Approximately 20,000 fractures
    - Approximately 40,000,000 computational cells
    - The minimum fracture length is 2 meters

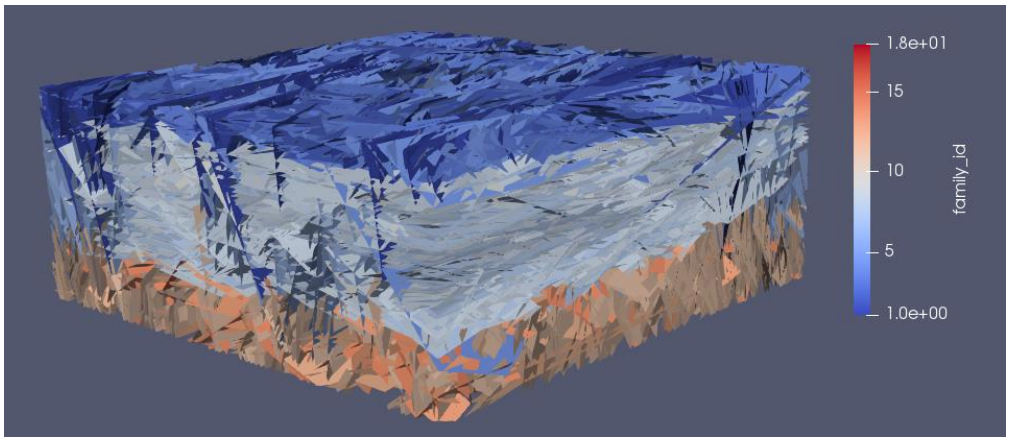

Figure 5 **Example of a DFN realization for the Topopah Spring Aquifer. Each fracture is colored by fracture family ID and the three horizontal zones are observed.**

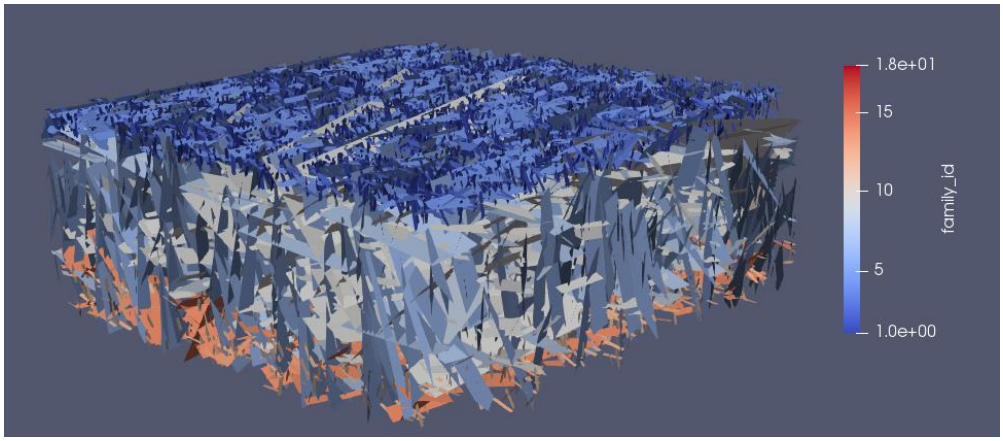

Figure 6 **Example of a DFN realization for the Lava Flow Aquifer. Each fracture is colored by fracture family ID and the horizontal layers are observed.**

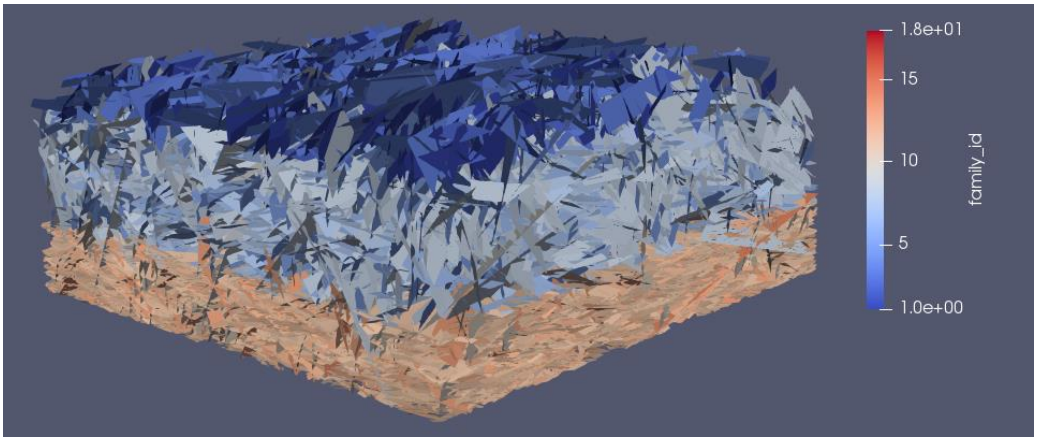

Figure 7 **Example of a DFN realizations for the Tiva Canyon Aquifer. Each fracture is colored by fracture family ID and the three horizontal layers are observed.**

4 METHODOLOGY OF UPSCALED PARAMETERS CALCULATION

4.1 Flow and Transport Simulations

4.1.1 Flow Simulation

The same approach to calculate the conductive properties of the DFN is applied to all three aquifers at Pahute Mesa, the TSA, LFA, and TCA. The detail description of the method can be found in our previous report [Makedonska et al, 2018c]. Here we present the basic formulations.

Fracture aperture, transmissivity and permeability are defined as function of fracture length and calculated according to the relationships defined for the Pahute Mesa fracture network (Appendix L of NSTec, 2014; Golder Associates, 2014).

The fracture transmissivity, T, is correlated to fracture length, L, and given as:

$$T = 1.0x10^{-7}L^{1.3681}, \text{ [m}^2\text{/s]} \quad (1)$$

Fracture hydraulic aperture, b_h, is calculated from T given in Eq. (1) using the cubic law:

$$b_h = \left(\frac{12\,\mu\,T}{\rho g}\right)^{1/3} \text{ [m]} \quad (2)$$

where μ = 8.9 e-4 [Pa s] is the dynamic viscosity if water at 20 °C;

g is a gravity acceleration, *g* = 9.8 [m/s^2];

ρ is a water density at 20 °C, ρ = 997 [kg/m^3].

Hydraulic fracture permeability, k_h, is defined as a function of hydraulic fracture aperture, b_h, and calculated using the cubic law:

$$k_h = \frac{{b_h}^2}{12} \text{ , [m}^2\text{]} \quad (3)$$

Mechanical fracture aperture, b_m, is defined as a function of hydraulic fracture aperture b_h:

$$b_m = \mathrm{m} \cdot b_h \text{ , [m]} \quad (4)$$

where *m* is a random integer number, chosen from uniform distribution in [1,..,3]. A random number *m* is chosen for each fracture in DFN to calculate the mechanical aperture and an updated fracture permeability, k', is derived to preserve the T versus L relation given by equation (1):

$$T = k_h b_h = k' b_m \quad (5)$$

Figure 8 shows the CDF distributions of hydraulic (a) and mechanical (b) fracture aperture for one of the DFN realizations for each considered aquifer. Since hydraulic fracture aperture and hydraulic fracture permeability are defined as function of fracture length, the distributions show rapid concentration

increase on the certain values of aperture and permeability. The smooth behavior is observed in aperture and permeability distributions of fracture networks generated according to TSA and TCA fracture characteristics (Table 1 & Table 3), where all the fracture sizes are sampled from the statistical distributions. The step-like behavior of hydraulic aperture and permeability distributions in DFNs of Lava Flow Aquifer is explained by the fracture characteristics of the LFA, in particular, the fracture size distributions. Fracture sets SP and DP in all horizontal layers (UV, SL, LV, and BFB) define fracture lengths as unit thickness with the same aspect ratio (see Table 2). It leads to DFNs with multiple fractures of equal size and hence, T and hydraulic aperture. The step-like nature of the hydraulic aperture CDF (Figure 8a) is muted by the randomness of converting hydraulic to mechanical aperture (Figure 8b). Figure 9a shows the initial permeability distributions for one of the DFN realizations for each considered aquifer, and Figure 9b shows the adjusted permeabilities (k') that result when the initial fracture permeability is adjusted according to equation 5.

The PFLOTRAN [Lichtner et al., 2015] multiphysics code is used to obtain steady-state pressure solutions for fully saturated flow on the DFNs. Constant pressure boundary conditions are applied to inflow and outflow boundary faces, and no-flow boundary conditions are applied on all remaining boundaries. We calculate flow and transport in each of the three principal directions separately. Each simulation assumes the same pressure head gradient, 0.0102 m/m (density and gravity are not included):

- Top – Bottom, vertical flow along z direction (100 m), pressure difference: ΔP = 10,000 Pa.
- North – South, horizontal flow along y direction (250 m), pressure difference: ΔP = 25,000 Pa.
- East – West, horizontal flow along x direction (250 m), pressure difference: ΔP = 25,000 Pa.

Figure 10 shows the steady-state flow pressure solution in North-South direction of flow for each of the three aquifers. Figure 11 shows the fracture permeability distributions for the same DFNs used to generate the pressure solutions shown in Figure 10. A comparison of the two figures illustrates how longer, higher permeability fractures affect the gradient across the domain, essentially introducing heterogeneity into the pressure field at a given distance along the flow direction. The longer, higher permeability fractures are typically tectonic fractures that cross-cut the entire thickness of the domain.

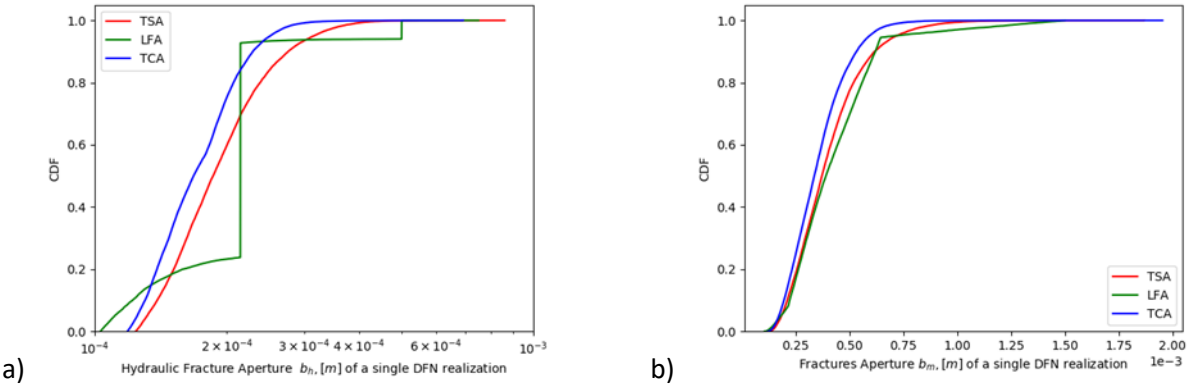

a) b)

Figure 8 **Hydraulic fracture aperture distributions, Eq.2 (a) and mechanical fracture aperture, Eq.4 (b) for one of the DFN realizations in each considered aquifer in Pahute Mesa.**

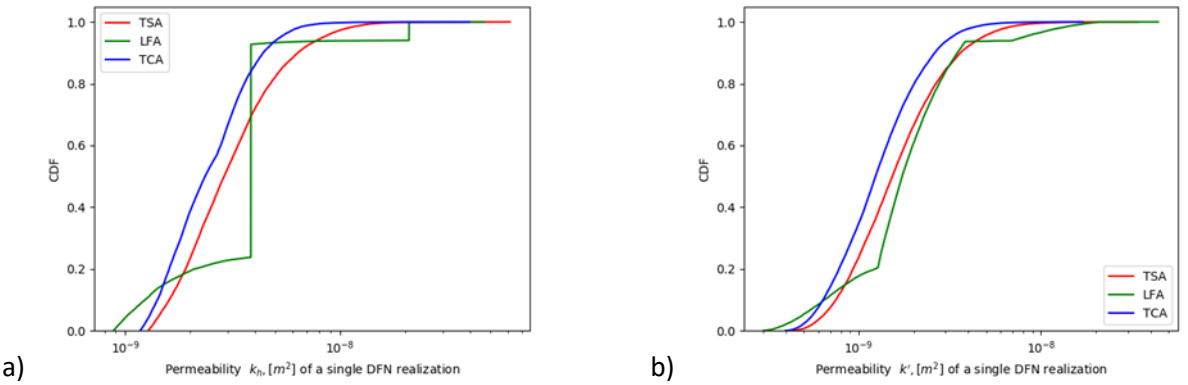

a) b)

Figure 9 **Hydraulic fracture permeability distribution, Eq.3 (a), and fracture permeability k' (b) for one of the DFN realizations in each considered aquifer in Pahute Mesa.**

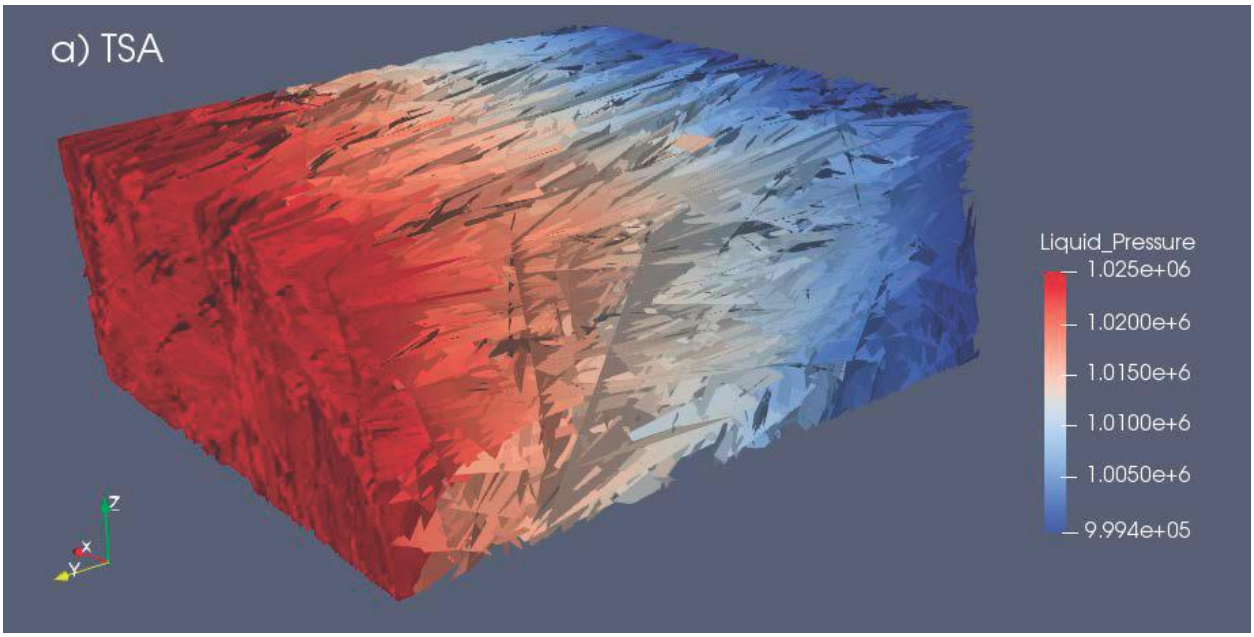
a) TSA
Liquid_Pressure
1.025e+06
1.0200e+6
1.0150e+6
1.0100e+6
1.0050e+6
9.994e+05
z
x
y

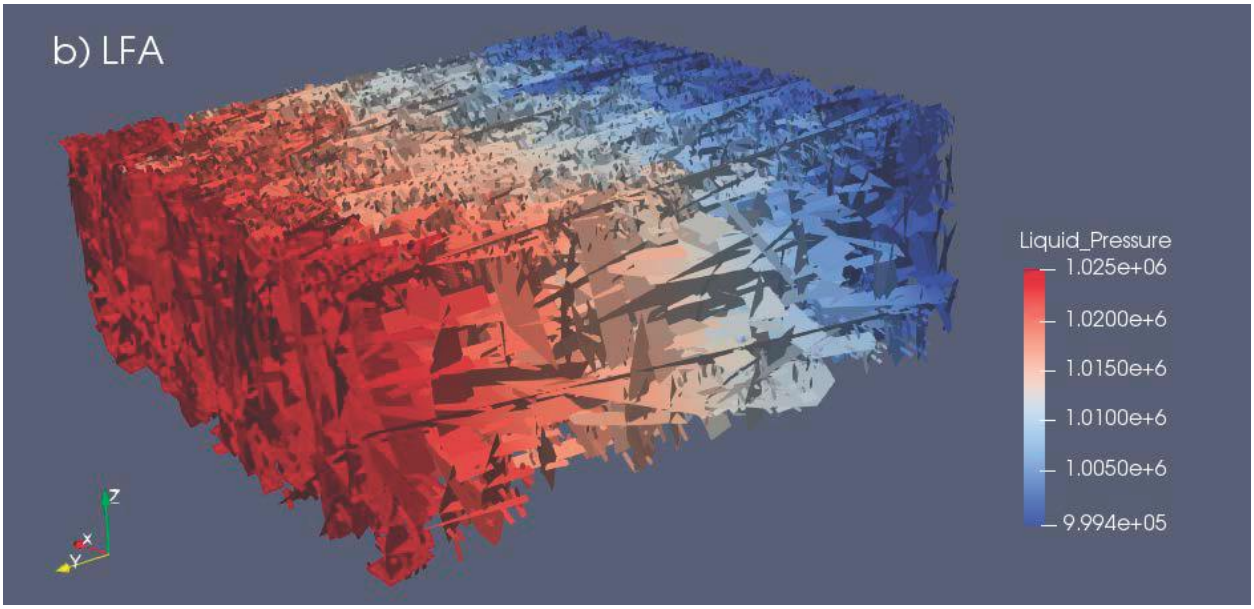
b) LFA
Liquid_Pressure
1.025e+06
1.0200e+6
1.0150e+6
1.0100e+6
1.0050e+6
9.994e+05
z
x
y

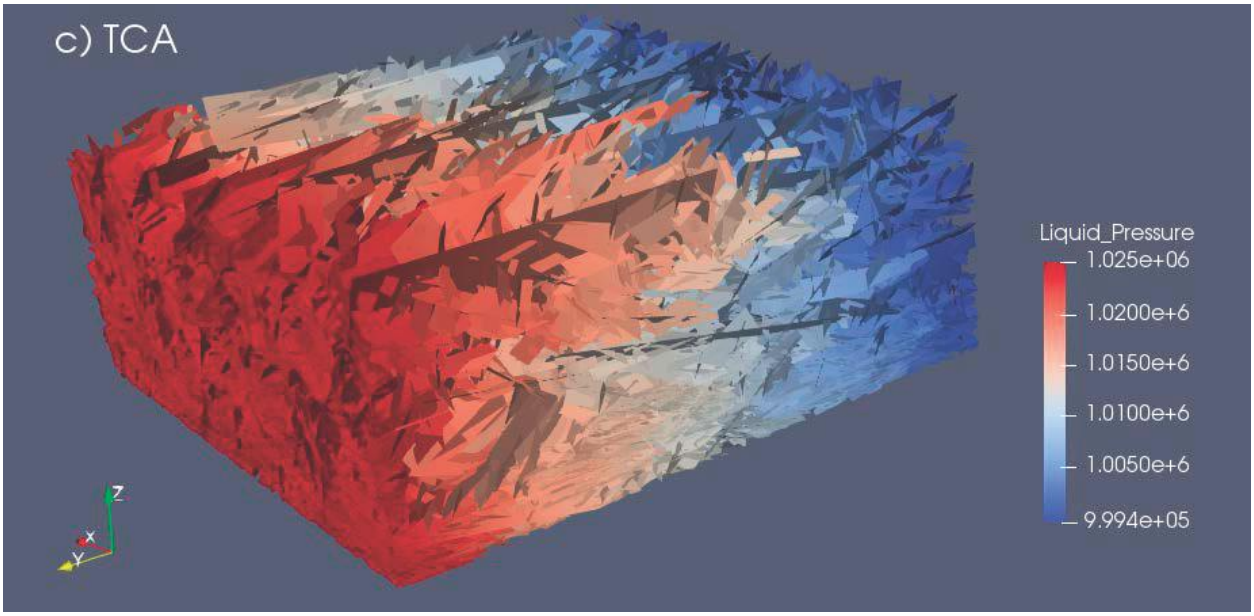

Figure 10 **Pressure solutions for fully saturated flow obtained for one DFN realization with (a) TSA, (b) LFA, and (c) TCA fracture characteristics. Blue colors represent low pressure and red colors are high pressure. Here flow direction is along the y axis, in the North-South (left to right) direction. These flow fields were generated using the DFN realizations shown in Figure 11.**

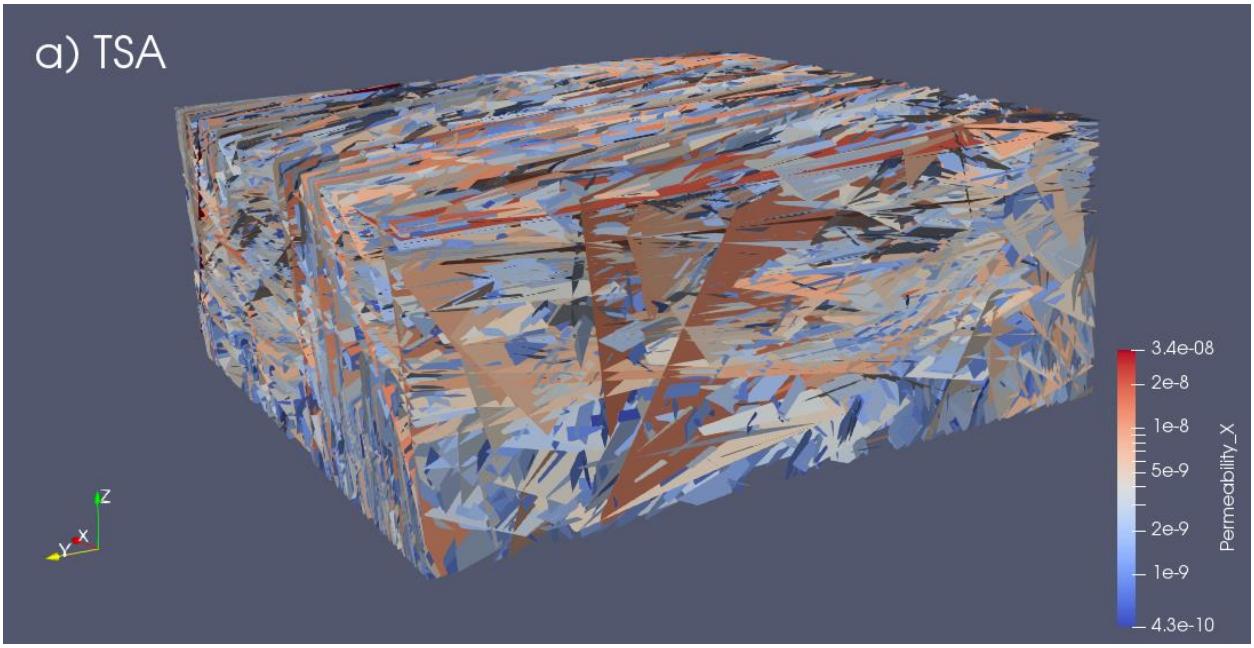

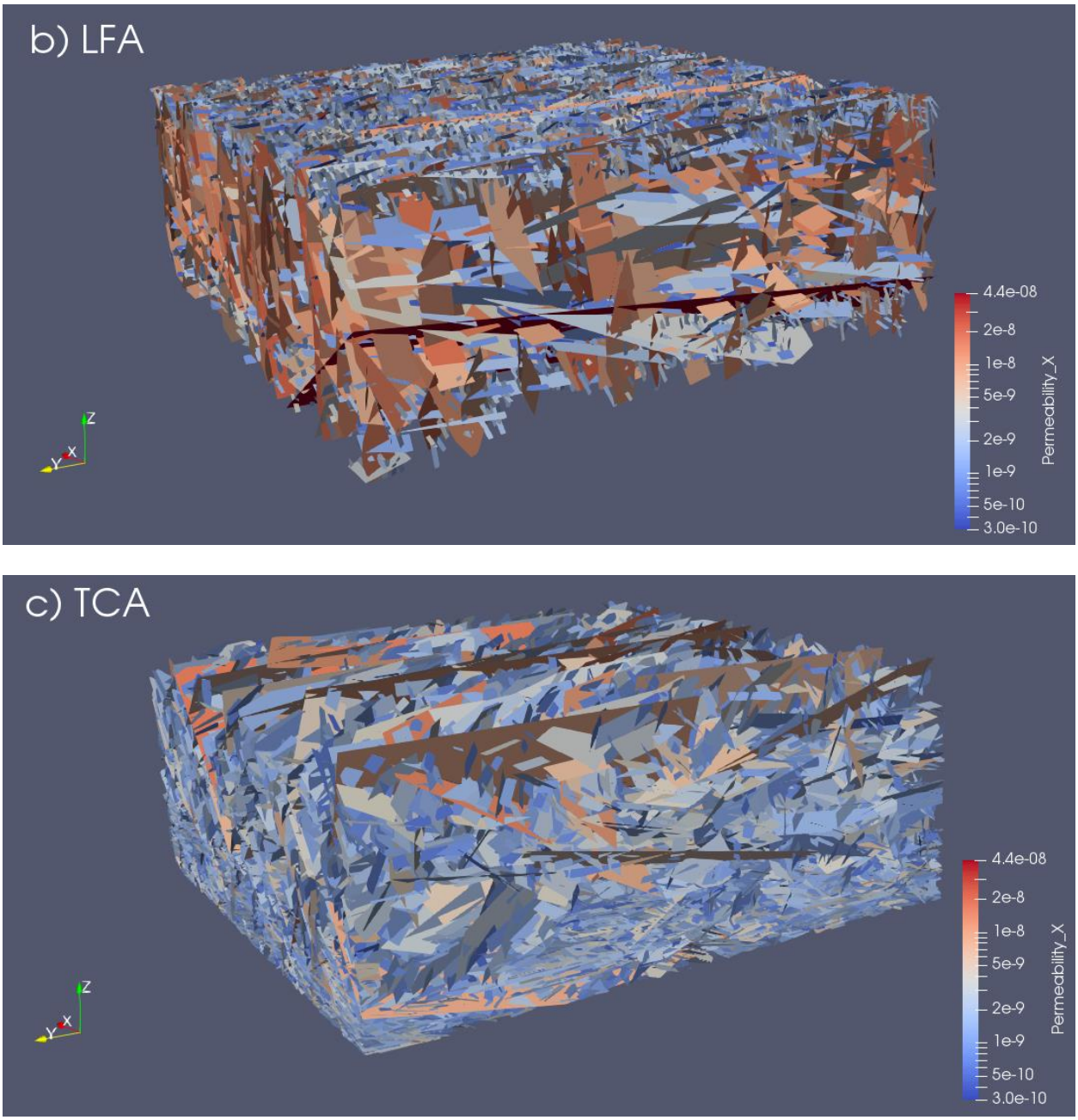

Figure 11 Distribution of fracture permeability, k', for one DFN realization with (a) TSA, (b) LFA, and (c) TCA fracture characteristics. Permeability is in meters-squared.

4.1.2 Lagrangian Transport Modeling

We use the particle tracking approach (*dfnTrans*) described by Makedonska et al. [2015] to model advective transport in three-dimensional DFNs. Particles are initially placed on fracture edges at inflow boundary face and distributed accordingly to the calculated input water flux of the boundary fracture. A fracture with higher input water flux gets a proportionately larger number of particles than a fracture with lower flux. Along an individual fracture edge, particles are seeded equidistantly. Since each particle represents the same mass of solute, all fractures have essentially the same input concentration. As

particles move through the DFN and meet fracture intersections, they tend to continue travelling through the large fractures, which have higher transmissivity. At every fracture-fracture intersection, a decision about the next path of a particle is made: the downstream cell is chosen randomly with probability proportional to the outgoing flux. This is equivalent to assuming the complete mixing of particles in cells located at fracture intersections (Sherman et al., 2019). Details of the Lagrangian particle tracking method can be found in Makedonska et al., 2015. As a result of applying flux-weighted probabilities to determine flow direction, channeling of particles through larger, higher-permeability fractures is enforced. However, there is a non-zero probability for particles to move through small fractures, which makes their cumulative travel times longer. These effects contribute to both faster and slower transport through the network, resulting in a distribution of particle breakthrough times at the down gradient boundary and longitudinal and lateral spreading.

Although *dfnWorks* is capable of introducing variability in fracture aperture, transmissivity, and permeability within, as well as between, individual fractures, this capability was not implemented in this application to the simulation of transport for aquifers at Pahute Mesa. Here, fracture properties are assumed to be uniform within individual fractures. Therefore, any channeling observed in flow and particle transport behavior is due to heterogeneity in the fracture network properties and not variability within the plane of any individual fracture. Makedonska et al. [2016] looked at both mechanisms for channeling and found that one or the other could dominate depending on the problem scale, degree of within-fracture heterogeneity and its correlation length, and whether one is concerned with early or late-time behavior. The median particle breakthrough was relatively insensitive to the inclusion of within-fracture variability. Other recent studies have found similar behavior (Frampton et al., 2019).

One hundred independent DFN realizations were generated for each Pahute Mesa aquifers - the TSA, LFA, and TCA. Transport simulations were conducted in all three principal directions across each DFN realization. For each transport simulation, 10^5 particles were released across the input face, and travel time is measured at the outflow boundary face. Because the particles released on the inflow face can only exit a single outflow face, the linear travel distance of each particle is the same for a given transport direction and DFN realization, the variability of travel times represents differences in the average velocities of individual particles through the DFN.

In analyzing the breakthrough curves (BTCs) , of transport simulations for TSA, LFA and TCA (Figures 12, 13 and 14), a dependence of BTCs on flow direction can be observed: transport in the North-South direction is faster than in the East-West direction because the largest fractures are oriented North-South and channeling in the largest fractures results in earlier breakthrough. The effect of flow direction is stronger in the TSA and TCA (Figures 12 and 14), and more subdued for the LFA (Figure 13). Breakthrough in the top-bottom direction is also relatively fast for the TSA, LFA and TCA because the model dimension is only 100 m in the vertical direction, compared to 250 m in the North-South and East-West directions. Moreover, initial breakthrough in the Top-Bottom direction can happen very quickly because flow in this direction is often dominated by a few large tectonic fractures which, unlike cooling fractures, can cross all the cooling sub-units, resulting in highly channelized flow.

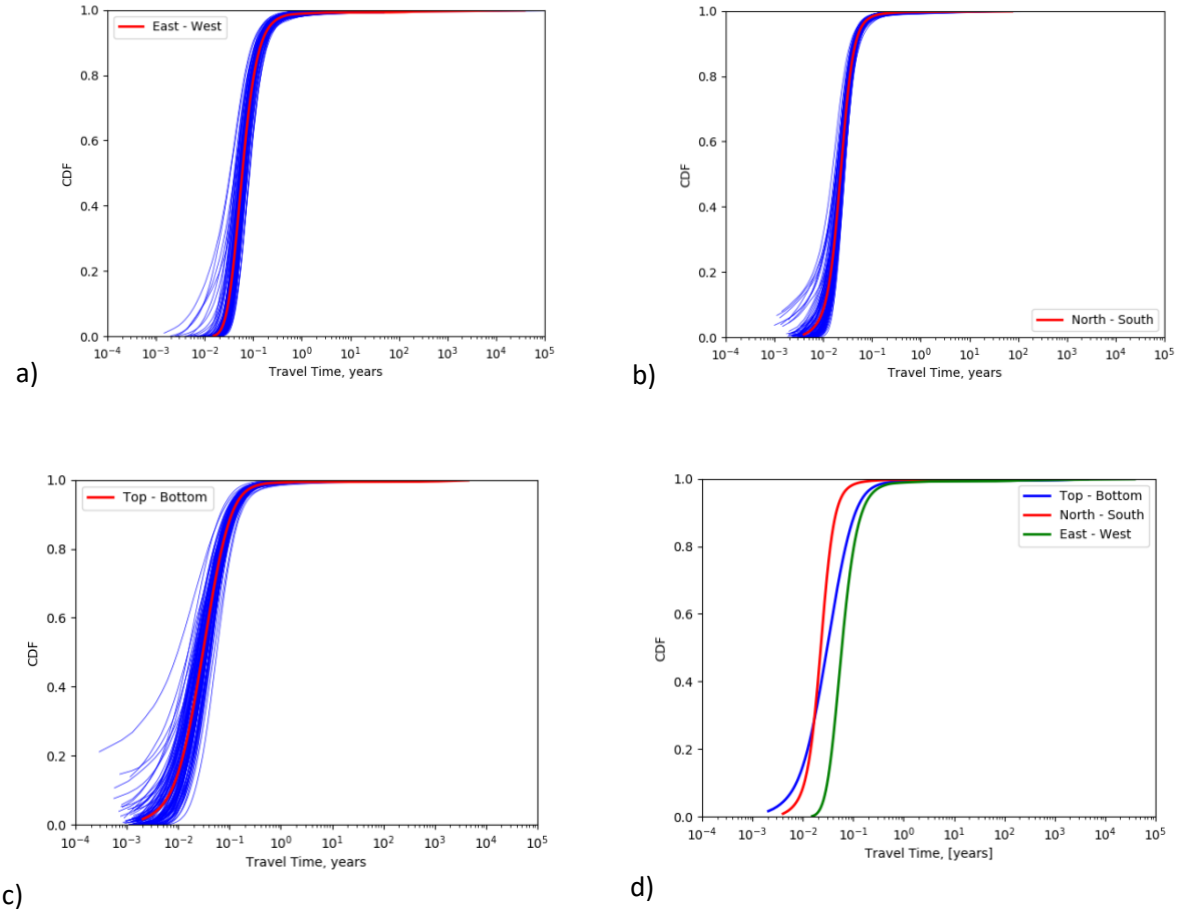

Figure 12 **BTCs of advective transport simulated for one hundred DFN realizations of TSA in all three flow directions (blue curves) along with the directional average (red): a) East - West; b) North – South; c) Top – Bottom; and d) The directional BTCs averaged over 100 independent DFN realizations of the TSA.**

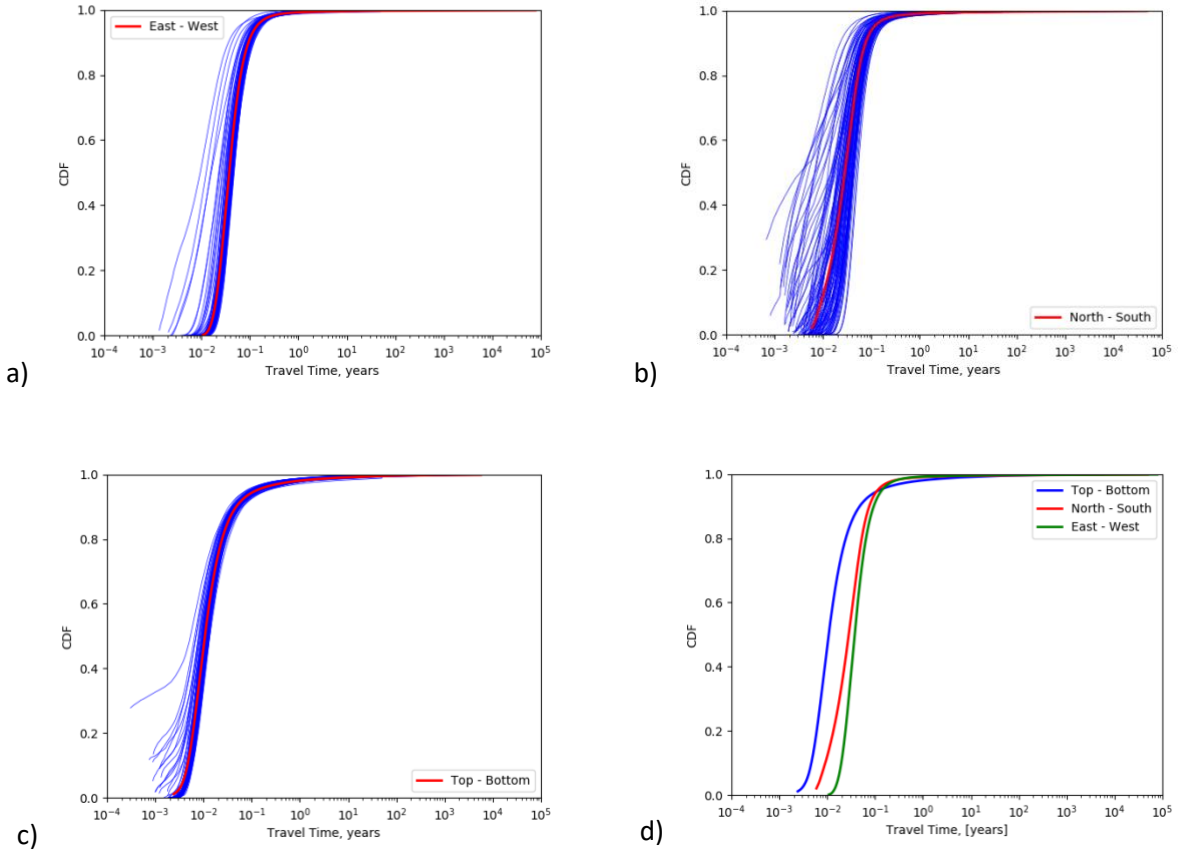

Figure 13 **BTCs of advective transport simulated for one hundred DFN realizations of LFA in all three flow directions (blue curves) along with the directional average (red curve): a) East -West; b) North – South; c) Top – Bottom; and d) The directional BTCs averaged over 100 independent DFN realizations of the LFA.**

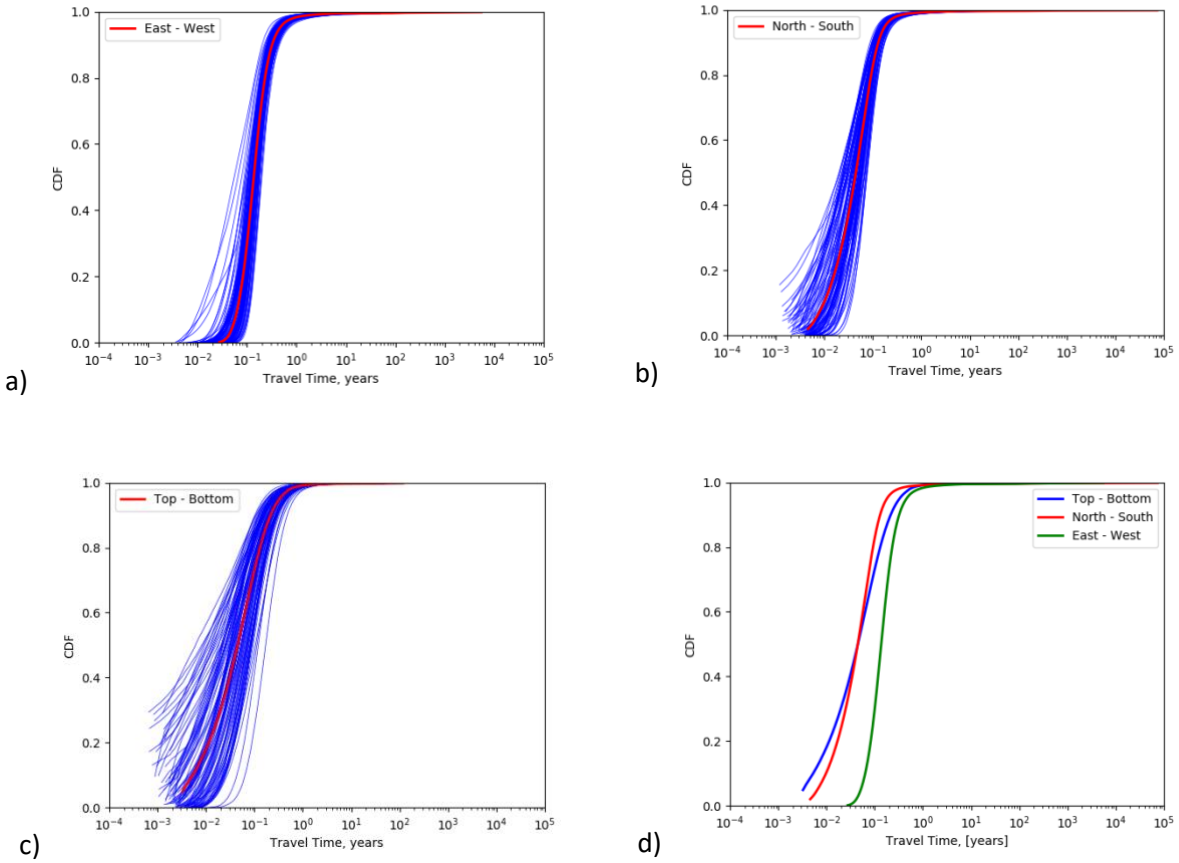

Figure 14 BTCs of advective transport simulated for one hundred DFN realizations of TCA in all three flow directions (blue curves) along with the directional average (red curve): a) East -West; b) North – South; c) Top – Bottom; and d) The directional BTCs averaged over 100 independent DFN realizations of the TCA.

4.2 Calculation of Upscaled Parameters

The flow and particle tracking results are used to upscale the following parameters in the North-South, East-West and Top-Bottom directions:

- Effective bulk permeability
- Volumetric porosity
- Transport porosity
- Longitudinal Dispersivity

The following sections describe how each of these upscaled parameters is calculated.

4.2.1 Effective Permeability

In order to estimate the **effective bulk permeability**, k [m^2], of the entire domain, we use Darcy's Law:

$$Q = \frac{-kA}{\mu}\frac{(P_2 - P_1)}{L} \quad (6)$$

where

Q is the volumetric flux in and out of the model domain [m^3/s];

μ is the water dynamic viscosity at 20 °C [8.9 10^{-4} Pa s];

L_h is a horizontal length of the domain [250 m];

L_v is a vertical length of the domain [100 m];

A_v is the total area of the in-flow boundary in the case of vertical flow (Top-Bottom) [62,500 m^2];

A_h is the total area of the in-flow boundary in the case of horizontal flow (North-South, East-West) [25,000 m^2];

ΔP_v = 10 kPa = 10,000 Pa is the pressure difference ($P_2 - P_1$) for vertical flow;

ΔP_h = 25 kPa = 25,000 Pa is the pressure difference ($P_2 - P_1$) for horizontal flow;

The input flux per unit area, q [m/s], is calculated by dividing the input volumetric flux by the inflow area A:

$$q = \frac{Q}{A} = \frac{-k}{\mu}\frac{(P_2 - P_1)}{L} \quad (7)$$

The volumetric flux (Eq.6) along a boundary is calculated as the sum of the input fluxes defined by the flow solver, PFLOTRAN, on all the fracture edges along the in-flow boundary:

$$\sum_{i=1}^{N} q_i\, a_i = Q\ , \quad (8)$$

where *N* is the number of computational cells of fractures on the in-flow boundary, q_i is an input flux defined for cell *i*, and a_i is the area of the cell face *i* on the in-flow boundary. The area of the cell face, a_i, is defined as the length of the 2D cell edge times the fracture aperture. Substituting Eq. 6 and Eq. 8 yields:

$$\sum_{i=1}^{N} q_i\, a_i = Q = \frac{-kA}{\mu}\frac{(P_2 - P_1)}{L} \quad (9)$$

From (7) effective bulk permeability of the model domain is

$$k = -\frac{Q\mu L}{A(P_2 - P_1)} \quad (10)$$

where Q is defined numerically by Eq.6 and A is the area of the flow domain in the horizontal, A_h, or vertical, A_v, direction and $P_2 - P_1$ corresponds to the pressure difference ΔP_h or ΔP_v. Results of effective permeability calculations for one hundred DFN realizations for TSA, LFA, and TCA are shown in Figures 15,

16, 17, respectively. The effective permeability in the North-South direction is higher than in the other two directions for TSA and TCA, which is consistent with the fracture orientation characteristics and the BTCs observed in Figures 12 and 14. The average North-South to East-West permeability anisotropy for the TSA is 2.4 to 1, and for the TCA it is 3.1 to 1. The LFA is essentially isotropic with respect to permeability in the horizontal direction. The average North-South permeabilities of the TSA, LFA and TCA are 9.6e-13 ± 1.64e-13, 3.47e-13 ± 2.6e-13, and 3.48e-13 ± 1.33e-13 m^2, respectively, resulting in coefficients of variation (CV = Standard Deviation/Mean) of 0.18, 0.75 and 0.38.

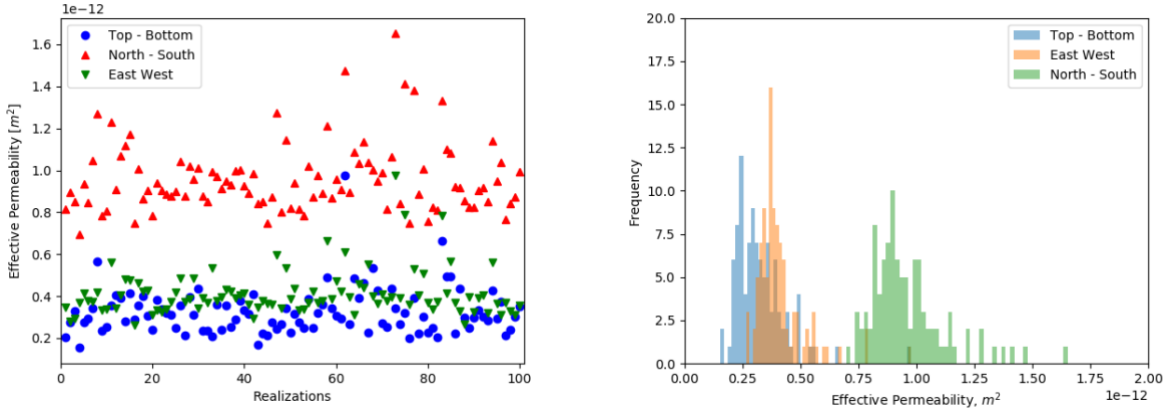

Figure 15 **Effective permeability results for 100 DFN realizations of the TSA. Effective permeability values for each DFN realization are shown in left panel; the histograms of effective permeability are shown in the right panel.**

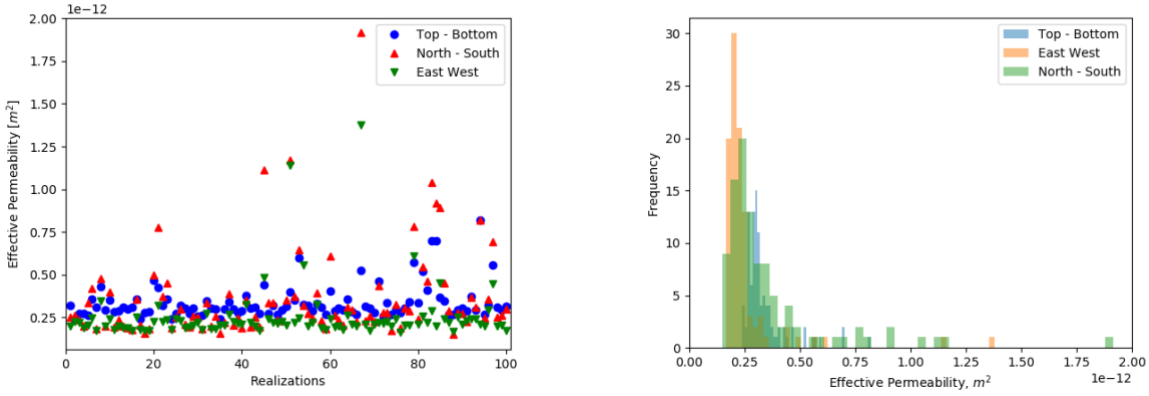

Figure 16 **Effective permeability results for 100 DFN realizations of the LFA. Effective permeability values for each DFN realization are shown in the left panel; the histograms of effective permeability are shown in the right panel.**

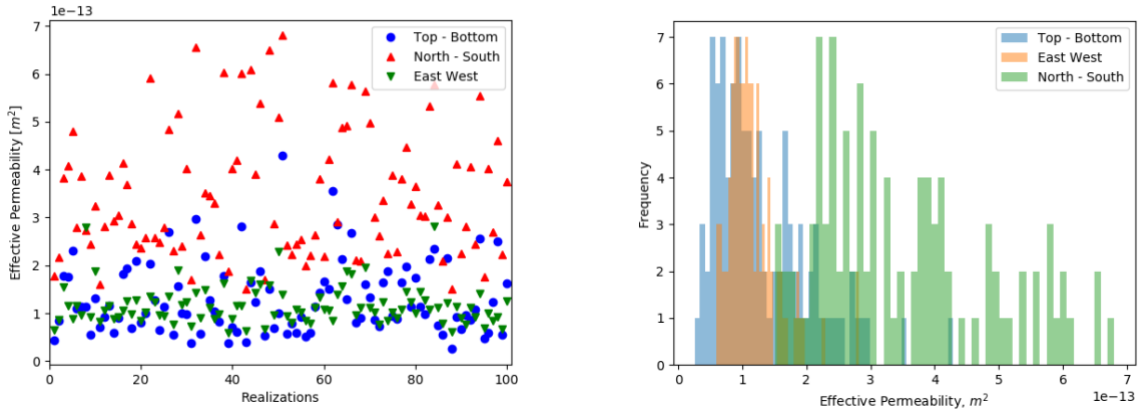

Figure 17 Effective permeability results for 100 DFN realizations of the TCA. Effective permeability values for each DFN realization are shown in the left panel; the histograms of effective permeability are shown in the right panel.

4.2.2 Volumetric Porosity

Volumetric porosity, n_v, of the domain is equal to the sum of the volumes of individual fractures divided by the volume of the domain:

$$n_v = \frac{\sum_{j=1}^{N_f} V_j}{V_d} \tag{11}$$

where N_f is the total number of fractures in the DFN, V_j is the volume of individual fracture j, defined as fracture area times fracture aperture, and V_d is a volume of the simulation domain.

4.2.3 Transport Porosity

Transport porosity (n_t) is calculated from the flux (q) through the domain and the mean particle breakthrough time (t_{50}), from which the mean transport velocity can be calculated as $v = L/t_{50}$. From the relationship $n_t = q/v$, we obtain

$$n_t = \frac{qt_{50}}{L}, \tag{12}$$

where q is an input flux calculated from Q/A (eq.7), t_{50} is estimated numerically as the time at which 50% of the particles have broken through, and L is the length of the domain in flow direction.

Results of calculated volumetric and transport porosities for 100 DFN realizations of the TSA , LFA and TCA are shown in Figures 18, 19, 20, respectively. Typically, transport porosity (n_t) is less than 25% of volumetric porosity (n_v) due to channelization, which allows the majority of the particles to bypass most of the fractures. Transport porosity displays a small directional dependence in the TSA (Figure 18) where the transport porosity in the North-South direction is slightly smaller than in the Top-Bottom or East-West directions. Conversely, the LFA has similar transport porosity in all three directions. In the TCA, transport porosity in the vertical direction is relatively low compared to either horizontal direction. This occurs

because flow in the vertical direction is dominated by longer, larger-aperture tectonic fractures which cross-cut individual cooling sub-units and tend to channelize flow.

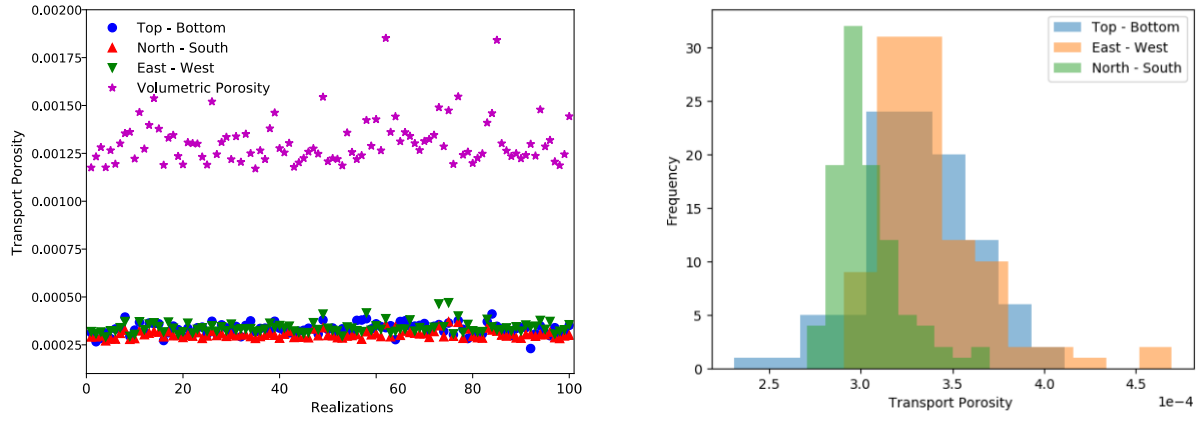

Figure 18 **Calculated volumetric porosity and transport porosity for 100 DFN realizations of the TSA. Transport porosity and volumetric porosity values for each DFN realization are shown in the left panel; the histograms of directional transport porosity are shown in the right panel.**

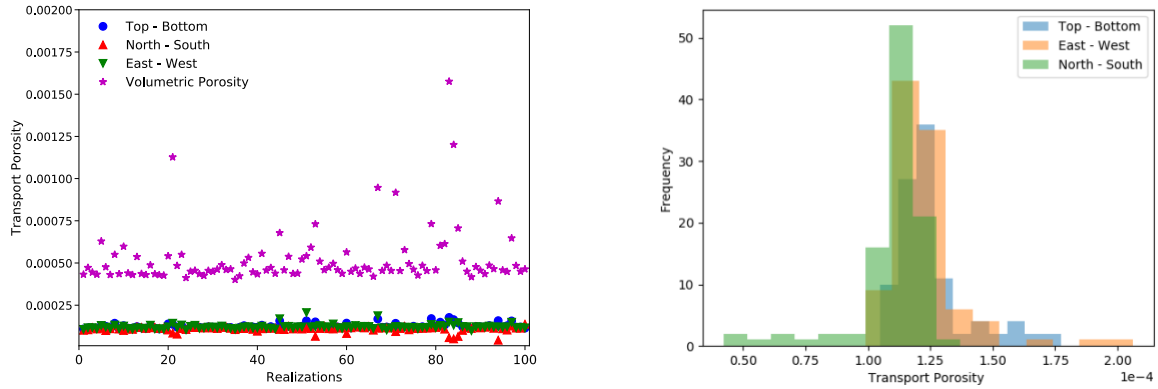

Figure 19 **Calculated volumetric porosity and transport porosity for 100 DFN realizations of the LFA. Transport porosity and volumetric porosity values for each DFN realization are shown in the left panel; the histograms of directional transport porosity are shown in the right panel.**

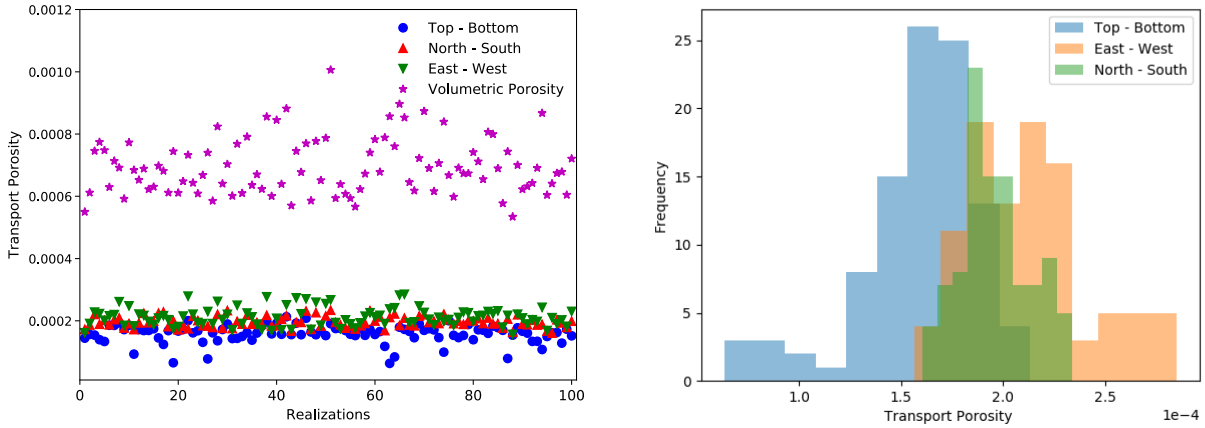

Figure 20 Calculated volumetric porosity and transport porosity for 100 DFN realizations of the TCA. Transport porosity and volumetric porosity values for each DFN realization are shown in the left panel; the histograms of directional transport porosity are shown in the right panel.

4.2.4 Longitudinal Dispersivity

We estimate the longitudinal dispersivity of the particle plume by fitting the distribution of the breakthrough times to a solution of the advection-dispersion equation (ADE) provided by Sauty (1980). The particles are inserted along the inlet plane at time *t = 0*. This corresponds to a slug of tracer injected instantaneously into a system represented by a one-dimensional column. Mathematically, this corresponds to Dirac delta impulse with mass *M* as the initial condition. The solution of the one-dimensional advection-dispersion equation with these boundary and initial conditions is

$$C_R(t_R, Pe) = \frac{K}{(t_R)^{1/2}} exp\left(-\frac{Pe}{4t_R}(1 - t_R)^2\right) \quad (13)$$

with

$$K = (t_{Rmax})^{1/2} exp\left(\frac{Pe}{4t_{Rmax}}(1 - t_{Rmax})^2\right) \quad (14)$$

where

$$t_{Rmax} = (1 + Pe^{-2})^{1/2} - Pe^{-1} \quad (15)$$

$t_R = ut/x = t/t_{50}$ is dimensionless time scaled to the median breakthrough time t_{50};

$C_r = C/C_{max}$ where C_{max} is the maximum breakthrough concentration;

t_{Rmax} corresponds to the time of maximum breakthrough concentration C_{Rmax}; and

Pe is the Peclet Number

$$Pe = \frac{ux}{D} \tag{16}$$

defined using the median velocity *u,* length of the domain *x,* and the dispersion coefficient *D.* We estimate *u* using the median breakthrough time of particles in the system (t_{50}) and the length of domain (L) as u = L/t_{50}.

Using these equations, we only need to determine the Peclet number *Pe* in the equation for $C_R(t_R,Pe)$. To do so, we minimize the difference between the $C_R(t_R,Pe)$ and the empirical particle data for the first 99% of mass through the system. We do not calibrate to data in the tail of the distribution because most of the data exhibit power-law scaling while the tail of $C_R(t_R,Pe)$ decays exponentially.

Once the best fit is determined and the value of *Pe* is calculated, and recognizing that $D = u\alpha$ where α is dispersivity, we obtain

$$\alpha = \frac{x}{Pe} \tag{17}$$

Figures 21, 22, 23 show histograms of calculated scaled dispersivity, α/L, where the dispersivity value for each realization is calculated by fitting it with the one-dimensional ADE solution, and each value is made dimensionless by dividing the dispersivity by the length of the network in the corresponding direction (100 m for Top-Bottom and 250 m for North-South and East-West). The statistics of scaled dispersivity are given for each aquifer and each direction in Table 4.

A range in behavior in scaled dispersivity is shown for the three aquifers in Figures 21, 22 and 23. In the TSA, the average scaled dispersivity is about 0.09 ± 0.01 in the North-South direction, 0.13 ± 0.02 in the East-West direction, and 0.27 ± 0.07 in the Top-Bottom direction (Table 4). The larger scaled dispersivity in the Top-Bottom direction is due to channelization in a few long, transmissive tectonic fractures that cross-cut the different cooling subunits. Scaled dispersivities in the Top-Bottom and East-West directions in the TSA and LFA are similar, but scaled dispersivities in the North-South direction in the LFA tend to be much larger and more variable (0.22 ± 0.20) than for the TSA (Table 4). The TCA and LFA have similar scaled dispersivities in the North-South (0.24 ± 0.10 vs 0.22 ± 0.20) and East-West (0.13 ± 0.04 vs 0.13 ± 0.04) directions , but the Top-Bottom scaled dispersivity in the TCA is on average much larger and more variable (0.47 ±0.27) compared to the average scaled Top-Bottom dispersivity of the TSA (0.27 ± 0.07) and LFA (0.21 ± 0.03). To calculate the actual dispersivity values in meters, the scaled dispersivities in the North-South and East-West directions should be multiplied by 250 m and the scaled dispersivities in the Top-Bottom direction should be multiplied by 100 m.

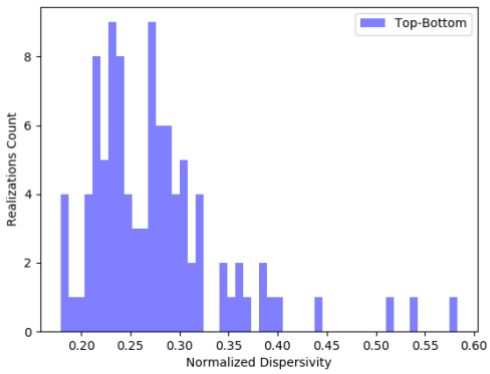

a)

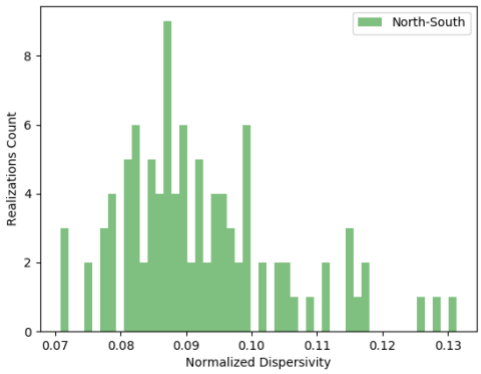

b)

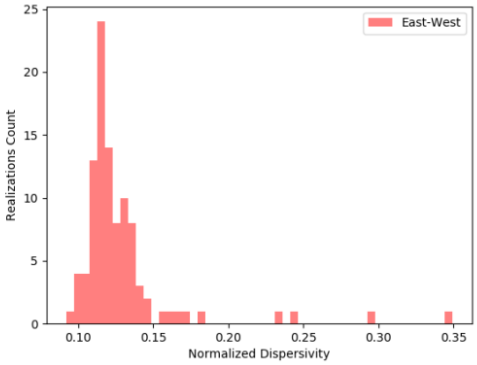

c)

Figure 21 **Histogram of dimensionless longitudinal dispersivity distribution of 100 DFN realizations of TSA: a) Top-Bottom direction of flow; b) North – South direction of flow; c) East – West direction of flow.**

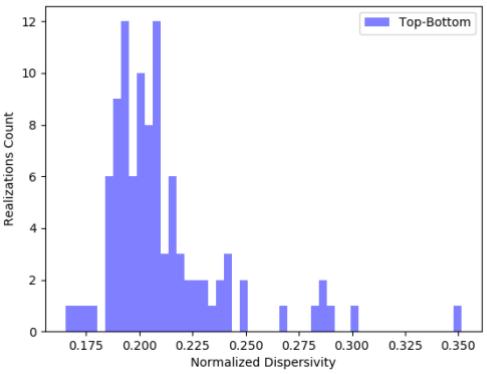

a)

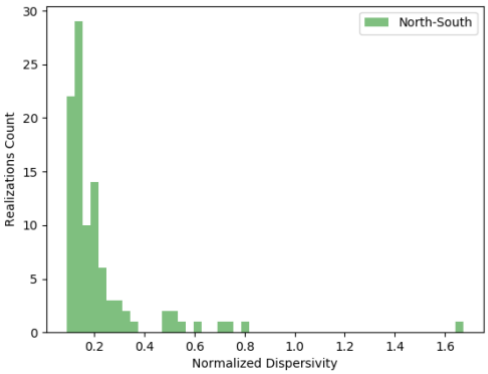

b)

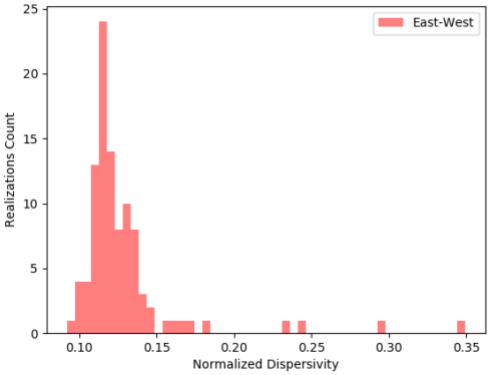

c)

Figure 22 Histogram of dimensionless longitudinal dispersivity distribution of 100 DFN realizations of LFA: a) Top-Bottom direction of flow; b) North – South direction of flow; c) East – West direction of flow.

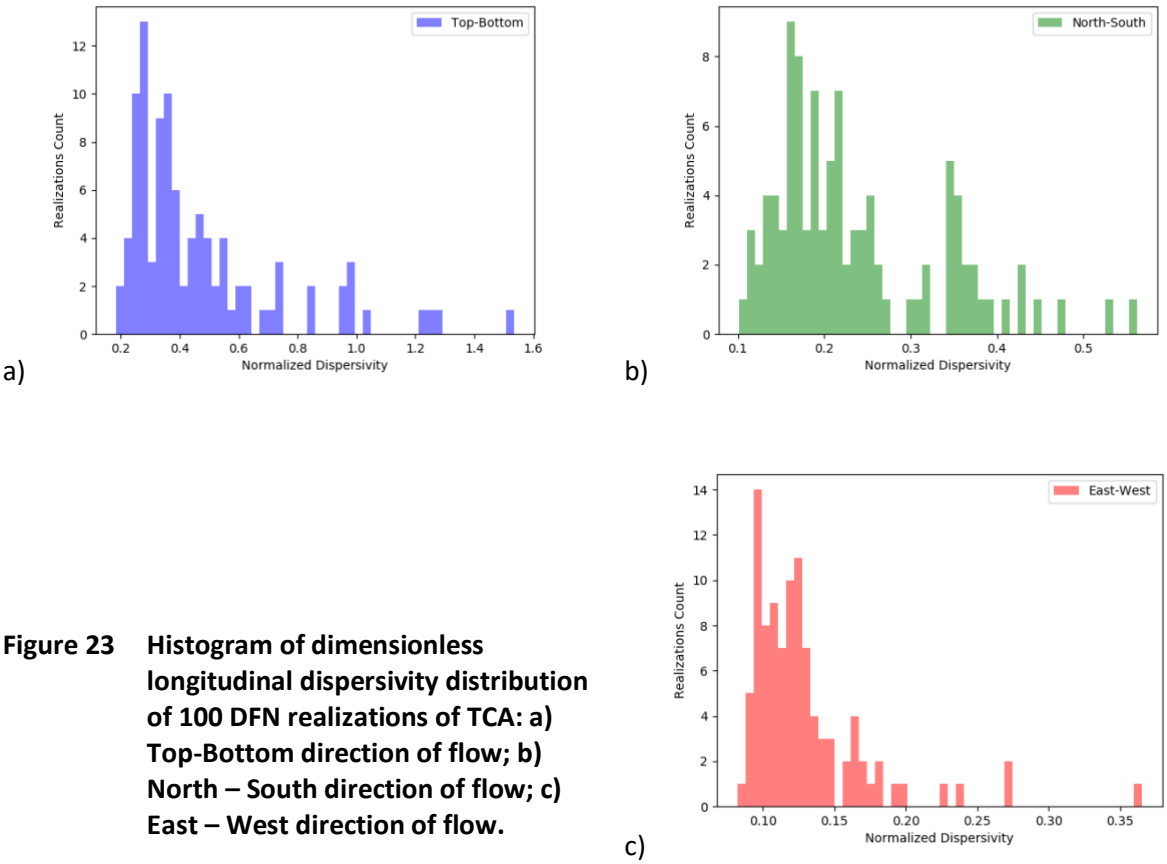

Figure 23 Histogram of dimensionless longitudinal dispersivity distribution of 100 DFN realizations of TCA: a) Top-Bottom direction of flow; b) North – South direction of flow; c) East – West direction of flow.

Table 4 summarizes the means and standard deviations (STD) for the effective permeability, transport porosity, volumetric porosity, and longitudinal dispersivity in each of the three directions run for the 100 realizations of the TSA, LFA and TCA fracture networks.

Table 4
Means and standard deviations of upscaled parameters

	Topopah Spring Aquifer					
	Top – Bottom		**North – South**		**East – West**	
	Mean	STD	Mean	STD	Mean	STD
Effective Permeability, [m^2]	3.255e-13	1.112e-13	9.600e-13	1.647e-13	4.116e-13	1.088e-13
Transport Porosity	3.321e-04	2.996e-05	3.034e-04	1.863e-05	3.386e-04	2.979e-05
Scaled Longitudinal dispersivity	0.27563	0.07096	0.09232	0.01243	0.12587	0.02045
Volumetric Porosity	Mean 1.308e-3			STD 1.201e-04		
	Lava Flow Aquifer					
	Top – Bottom		**North – South**		**East – West**	
	Mean	STD	Mean	STD	Mean	STD
Effective Permeability, [m^2]	3.377e-13	9.985e-14	3.569e-13	2.607e-13	2.530e-13	1.624e-14
Transport Porosity	1.252e-04	1.487e-05	1.096e-04	1.529e-05	1.221e-04	1.487e-05
Scaled Longitudinal dispersivity	0.21089	0.02910	0.21702	0.20304	0.12852	0.03574
Volumetric Porosity	Mean 5.232e-4			STD 1.725e-4		
	Tiva Canyon Aquifer					
	Top – Bottom		**North – South**		**East – West**	
	Mean	STD	Mean	STD	Mean	STD
Effective Permeability, [m^2]	1.303e-13	7.520e-14	3.479e-13	1.334e-13	1.156e-13	4.013e-14
Transport Porosity	1.579e-04	2.880e-05	1.959e-04	1.735e-05	2.118e-04	2.930e-05
Scaled Longitudinal dispersivity	0.46837	0.26572	0.23648	0.09849	0.12955	0.04296
Volumetric Porosity	Mean 6.935e-4			STD 8.954e-05		

Dispersivity can be calculated at a control plane any distance *x* from the inlet. To check for stability of the plume, (i.e., approach to the theoretical asymptotic Gaussian limit), one can calculate the derivative of dispersivity between two adjacent control planes to determine whether the derivative is approaching zero. A calculated derivative close to zero would indicate that a sufficient number of heterogeneous flow paths has been sampled so that the plume has stabilized. Preliminary results documented in Makednoska et al. (2018c) reported that these derivatives were still not zero near the boundaries of the flow system, indicating that a larger domain would be needed to calculate the theoretical asymptotic limit.

This study takes another approach for assessing the approach to stability in the estimate of dispersivity. Figure 24 shows the dispersivity values calculated from particle breakthrough at various control planes at different distances from the inlet boundary. The cases selected are for DFN realizations having the minimum and maximum dispersivity values at x = L for that flow direction. For the minimum dispersivity cases, the estimated dispersivities appear to have stabilized before the plane at x = L, except for the minimum East-West dispersivity of the LFA (Figure 24c). For the maximum dispersivity cases, the dispersivity value continue to increase throughout the domain, except for the maximum TSA case in the North-South direction, which shows near-constant dispersivity values in the downstream half of the flow domain (Figure 24b). For the cases where dispersivity continues to grow near x = L, it is reasonable to expect that the calculated dispersivity values would continue to increase with distance if the domain were extended further, although at a progressively smaller rate. The conclusion from this analysis is that the fitted dispersivities provide a lower bound estimate of the theoretical asymptotic limit that would be calculated if simulations at a larger scale had been feasible.

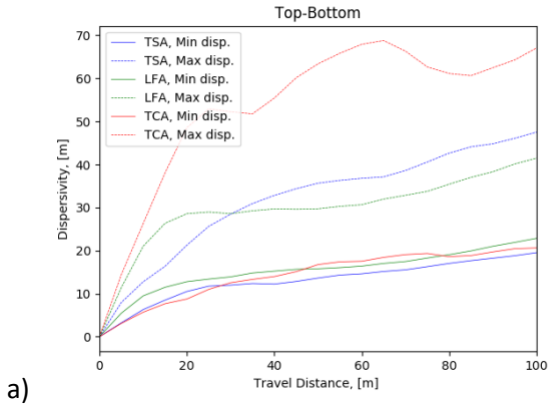

a)

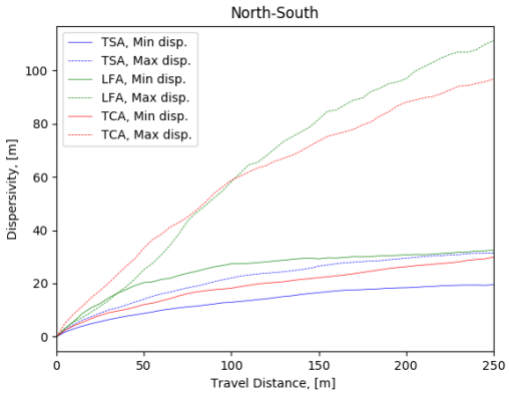

b)

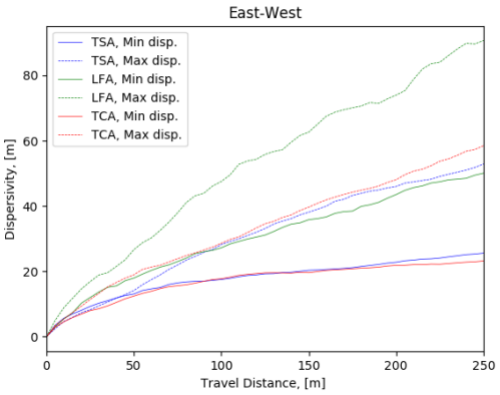

c)

Figure 24 The calculated particles dispersivity versus travel distance in (a) Top-Bottom, (b) North-South, (c) East-West directions for DFN realizations, which showed minimum and maximum values.

Figure 25 shows preliminary results of a particle-tracking calculation to investigate lateral spreading within the DFNs. The simulations were run in a North-South (y-axis) direction in each of the three aquifers. First, a 30 m x 30 m square was chosen in the middle of inflow boundary, where 1000 particles were initially placed at fracture edges which intersect the upstream face (blue circles). Then, particle x and z positions at a plane 125 m from the inlet boundary (green circles) and at the downgradient face at 250 m from the inlet boundary (red circles) are plotted. The figures indicate the tendency of particles to become concentrated in a few large fractures as they move downgradient due to flow channelization within large, more transmissive fractures.

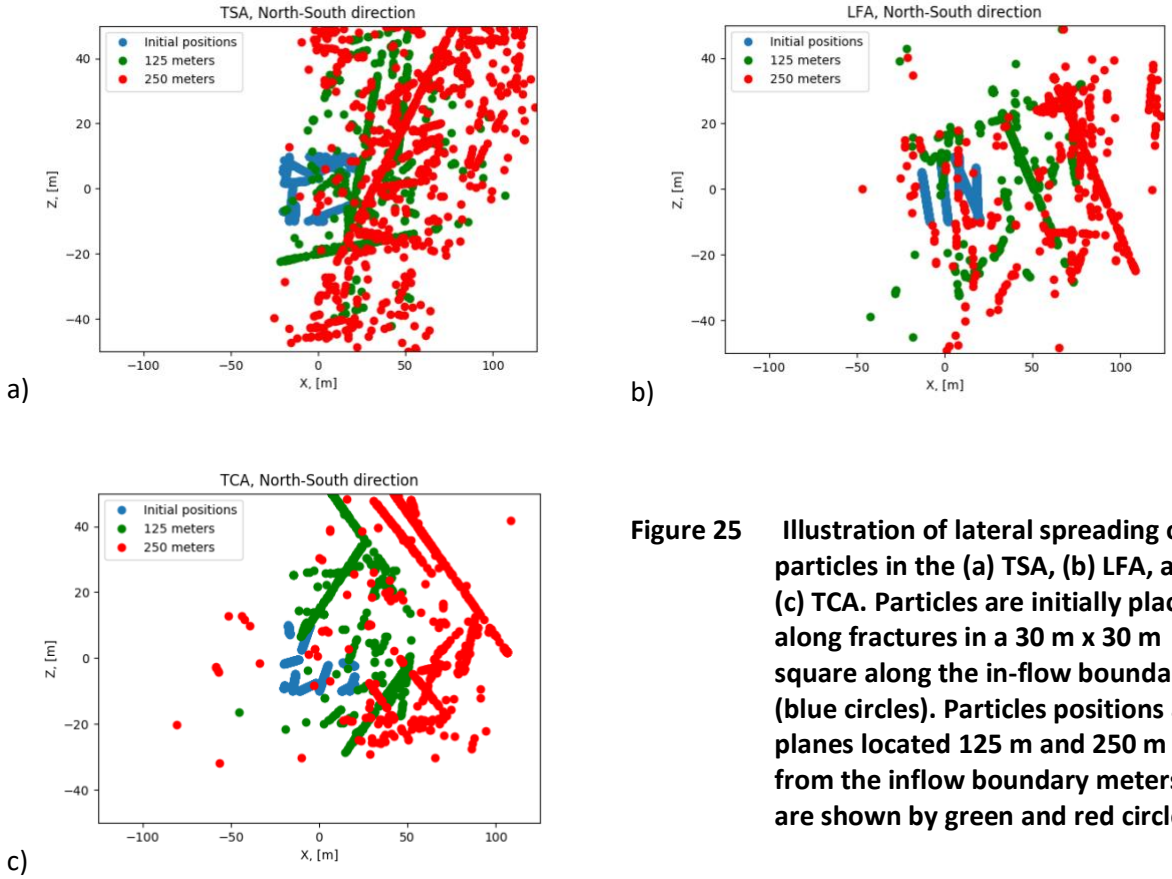

Figure 25 Illustration of lateral spreading of particles in the (a) TSA, (b) LFA, and (c) TCA. Particles are initially placed along fractures in a 30 m x 30 m square along the in-flow boundary (blue circles). Particles positions at planes located 125 m and 250 m from the inflow boundary meters are shown by green and red circles.

4.3 Upscaled Parameters for Equivalent Parallel-Plate Continuum Models

As discussed in Section 4.1, DFN modeling of the TSA, LFA, and TCA is computationally intensive and can only be performed at a relative local scale (250 m). On the other hand, the Pahute Mesa flow system spans many tens of kilometers, and can only be represented at this scale by continuum models with grid resolution comparable to the scale of the DFNs described in this report. The multiple DFNs at this local scale are generated stochastically using statistically defined fracture attributes to estimate hard-to-measure flow and transport properties, such as directional permeabilities, transport porosities, and dispersivities. Because the DFNs can include fractures whose length is a significant fraction of the model length scale, the results of this analysis can be sensitive to the details of an individual DFN realization. This indicates that sufficient spatial averaging has not taken place to produce representative element volume (REV) behavior, and that these properties will have to be represented by a statistical distribution even within an individual aquifer. A key process affecting radionuclide transport at Pahute Mesa is the diffusion of a radionuclide out of the rapidly flowing water in the fractures and into the relatively stagnant groundwater of the adjacent low-permeability rock matrix. To represent this process, many continuum groundwater flow and transport models assume an idealized fracture system consisting of parallel fractures with constant aperture and fracture spacing. Matrix diffusion in this type of idealized fracture system can be represented either with an analytical solution (e.g. Sudicky and Frind, 1982) or with a numerical approach that models the fracture system through an interconnected nodes and matrix as a

local, one-dimensional system of nodes extending from the fracture center to the center of the tabular matrix (e.g. Zyvoloski et al., 2007). In this section, we present a method for estimating the properties (fracture aperture and spacing) of an equivalent parallel-plate fracture system that will result in the same amount of diffusive fracture/matrix transfer as a more complicated DFN. First, we present the basis for the parameter estimates; then, we compare particle breakthrough calculated with this idealized fracture system to actual breakthrough from a DFN in which fracture matrix diffusion is simulated with a Time Domain Random Walk (TDRW) approach.

4.3.1 Static and Dynamic Fracture Network Intensity

In this section, we distinguish between the static and dynamic fracture intensities, which reflect the fracture area per volume under non-flowing and flowing conditions. These quantities can be different because flow channelization can cause fracture surface area to be effectively smaller than if the entire fracture area is considered. The dynamic fracture intensity essentially determines the wetted surface area of the fractures through which diffusion into the matrix can take place. Along with groundwater velocity, fracture aperture and matrix properties (porosity and tortuosity), and the species-dependent diffusion coefficient, the fracture wetted surface area determines the rate of diffusive loss to the matrix. For a given overall fracture network geometry, the fracture-wetted surface area can be higher or lower depending on whether flow is channelized into just a few fractures or whether flow is evenly distributed across more equally transmissive fractures. Thus, the dynamic fracture network intensity is a measure of the degree of channelization within a fracture network, becoming smaller with increasing channelization. In a fracture system in which fracture transmissivity is positively correlated with fracture length, such as the fracture sets identified for Pahute Mesa, the potential for channelized flow is increased compared with fracture sets in which transmissivity is independent of length. Channelized flow results in more rapid breakthrough of contaminants and non-Fickian transport behavior.

The static fracture network intensity, P_{32}, is defined as the average area of fractures per unit volume of rock and each generated DFN is conditioned on field observation data through the length and spacing distributions given in Table 1, 2, and 3 for each fracture set in the TSA, LFA, and TCA, respectively.

$$P_{32} = \frac{\sum_{i=1,..,N} A_i}{V} \left[\frac{m^2}{m^3}\right] \tag{18}$$

N = number of fractures in DFN

A_i = area of the fracture i

V = volume of the domain: 250 m x 250 m x 100 m.

Static intensity is used in fracture generation process: after each polygon (fracture) is accepted, the new accumulated P_{32} is recalculated and compared to the required intensity given by fracture characteristic data. Once the new P_{32} becomes equal to or larger than the specified value, the fracture generation process for the fracture set is stopped. After the entire DFN is formed, the isolated fractures are removed, which decreases the fracture network intensity. The histograms of final static fracture network intensity are shown in Figures 26, 27, 28 for multiple realizations of TSA, LFA, and TCA, respectively. As seen in these figures, within a given aquifer, the realization-to-realization variability in P_{32} is small. The highest

fracture intensity is in the TSA (1.05 to 1.09 m^{-1}) following by the TCA (0.86 to 0.89 m^{-1}), and finally the LFA (0.37 to 0.42 m^{-1}).

Isolated fractures or fracture clusters that are not connected to the main fracture cluster or boundary domains are not the only fractures that do not participate in the flow. There are fractures that intersect multiple fractures and belong to the main fracture clusters, but are not visited by particles due to flow channelization in the longer, more transmissive fractures. Those fractures should not be included in calculation of dynamic intensity, P_{32}', the intensity of flowing part of network, and applied to equivalent continuum models in order to compensate for the effects of channelization in the DFN. The dynamic intensity is defined as:

$$P'_{32} = \left[\frac{1}{Q}\frac{\sum_{i=1,..,N} A_i q_i}{\sum_{i=1,..,N} A_i}\right] P_{32} \tag{19}$$

$$Q = \sum_i q_i (L^3 T^{-1}),$$

q_i is the flux through fracture segment *i* (L^3T^{-1}).

Taking into account that particles follow the flow at fracture intersections, the flux is a relevant measure how many particles will flow through a fracture segment in a well-mixed segment. The histograms of dynamic fracture network intensity, P'_{32}, calculated in each flow direction for TSA, LFA and TCA, are shown in Figures 29, 30, 31, respectively. A comparison of the dynamic fracture intensities (P'_{32}) with the static P_{32} values shown in Figure 26, 27 and 28 indicates that the dynamic P'_{32} values are generally a small fraction of the static P_{32} values and display far more variability from realization to realization. In the TSA and TCA, dynamic P'_{32} values are smallest in the Top-Bottom direction and the North-South directions, reflecting channelization in cross-cutting tectonic fractures across cooling units in the Top-Bottom direction and the preferred North-South orientation of the longer tectonic fracture in the North-South direction. In both directions, these longer tectonic fractures to promote more channelization resulting in smaller P'_{32} values compared with the East-West direction. In the LFA, dynamic P'_{32} values are similar in all directions.

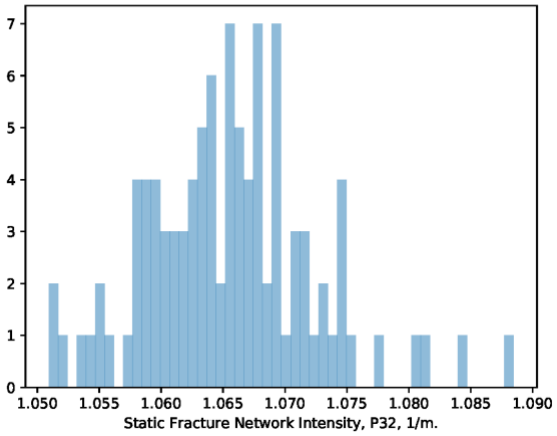

Figure 26 Histogram of static fracture network intensity of 100 DFN realizations of TSA.

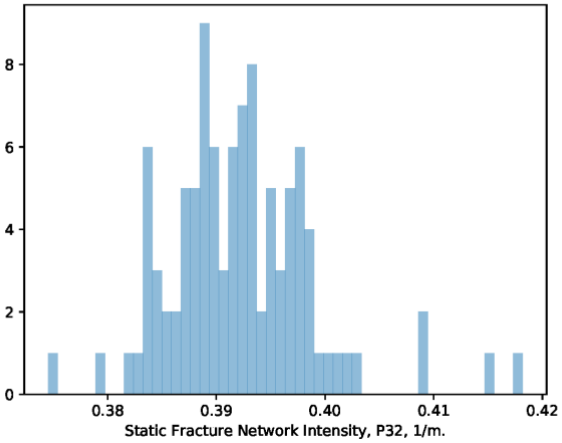

Figure 27 **Histogram of static fracture network intensity of 100 DFN realizations of LFA.**

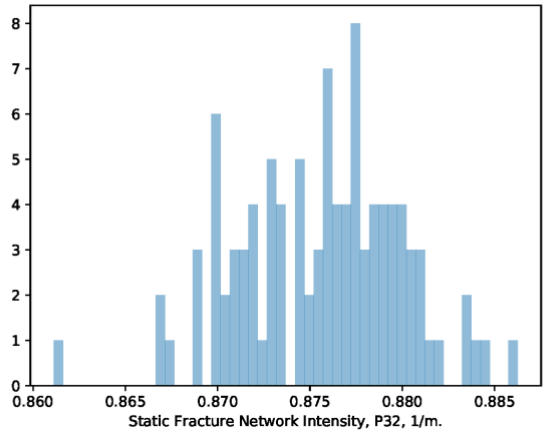

Figure 28 **Histogram of static fracture network intensity of 100 DFN realizations of TCA.**

a)

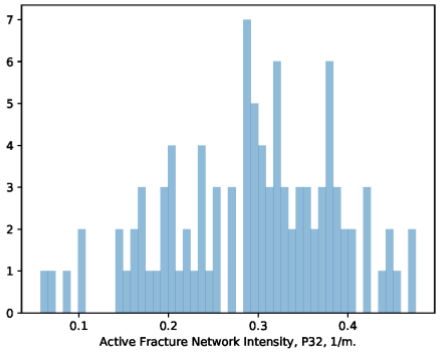

b)

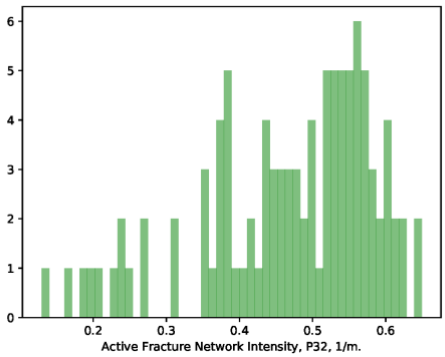

c)

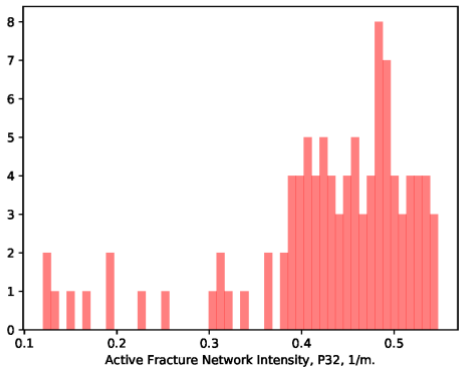

Figure 29 Histogram of dynamic fracture network intensity of 100 DFN realizations of TSA: a) Top-Bottom; b) North – South; c) East-West.

a)

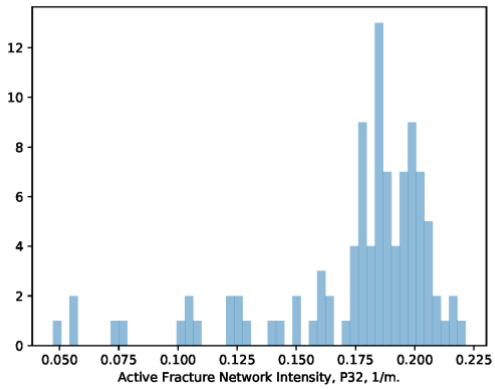

b)

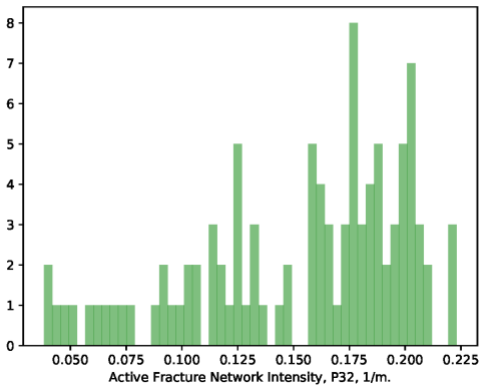

c)

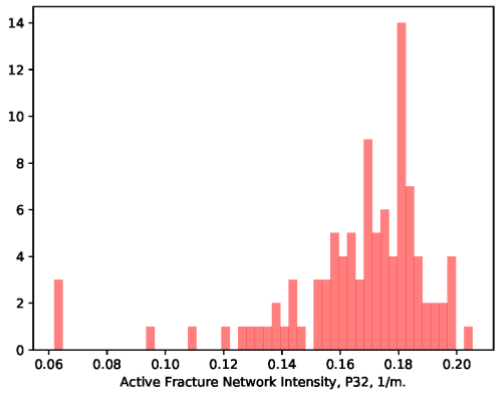

Figure 30 Histogram of dynamic fracture network intensity of 100 DFN realizations of LFA: a) Top-Bottom; b) North – South; c) East-West.

a)

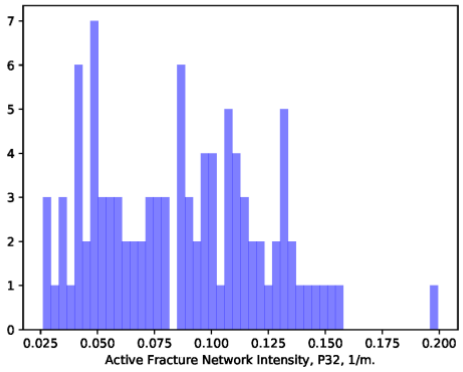

b)

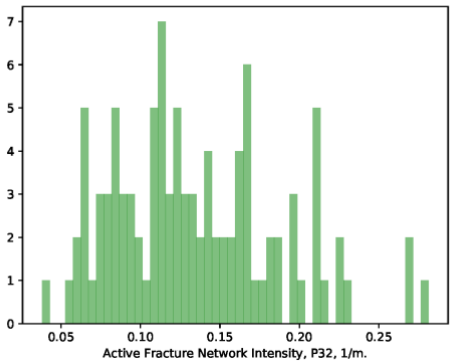

c)

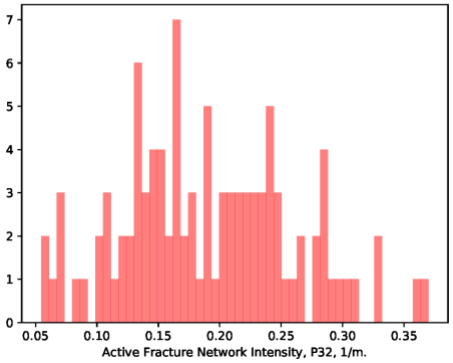

Figure 31 Histogram of dynamic fracture network intensity of 100 DFN realizations of TCA: a) Top-Bottom; b) North – South; c) East-West.

To construct a simple DFN with a network parallel plate fractures, consider an aquifer volume with length *L*, width *W* and height *H* and orthogonal vertical and horizontal fractures extending parallel to *L*. Then, a parallel plate DFN with two orthogonal fracture sets that has the same fracture network intensity (and fracture surface area) as the actual DFN can be defined as:

$$P_{32} = \frac{\mathrm{NvHL} + \mathrm{NhWL}}{\mathrm{WHL}}, \tag{20}$$

Where N_v is the number of vertical fractures, $N_v = W/\lambda_v$ where λ_v is the vertical fracture spacing;

N_h is the number of horizontal fractures, $N_h = H/\lambda_h$ where λ_h is the horizontal fracture spacing;

If $\lambda_h = n\,\lambda_v$, then

$$P_{32} = \frac{(n+1)}{n\lambda_v} \text{ or } \lambda_v = \frac{(n+1)}{n\,P_{32}} \tag{21}$$

To reflect channelization in the actual network, the dynamic intensity, P_{32}', can be used instead of static intensity P_{32}.

4.3.2 Fracture Spacing and Fracture Aperture for an Equivalent Parallel Plate Model

For an equivalent parallel plate model in which there are only vertical or horizontal fractures, the relevant relationships are

$$\lambda_v = \frac{1}{P_{32}}, \quad \text{and} \quad \lambda_h = \frac{1}{P_{32}}, \tag{22}$$

Fracture aperture, *2b*, is defined from transport porosity and spacing λ

$$2b = \lambda \cdot n_t \tag{23}$$

The fracture spacing and fracture aperture for parallel plate DFNs are calculated for each DFN realization and all three flow directions. Figures 32, 33 and 34 show the fracture spacing for TSA, LFA and TCA DFN realizations, respectively. The histograms of fracture aperture calculated for TSA, LFA, and TCA DFN realizations are shown in Figures 35, 36 and 37, respectively. The statistical summary of spacing and aperture for the TSA, LFA and TCA are given for the three principal directions in Table 5.

As seen in the Figures 32-37 and indicated in Table 5, the calculated average fracture spacing depends both on the aquifer and the flow direction. Average fracture spacing is larger in the Top-Bottom direction than in the North-South or East-West direction in the TSA and TCA because only the longer, cross-cutting tectonic fractures serve as transport pathways in the Top-Bottom direction, whereas other fracture sets contribute to transport in the horizontal directions. In the LFA, average fracture spacing is similar in all three directions. Since the equivalent continuum spacing is calculated in a way that preserves the surface area of the flowing fractures in the DFN, the larger fracture spacing indicates more channelization of flow in the vertical direction in the TSA and TCA. The standard deviation of spacing is also higher in the Top-Bottom direction for the TSA and TCA, indicating that there is more realization-to-realization variability in flow channelization in the vertical direction, as might be expected given the smaller length (100 m) in the vertical direction. The average equivalent fracture spacing in the North-South and East-West direction of the TSA is several times small than the averages calculated for the LFA or TCA, reflecting the initially higher P_{32} of the TSA (Figure 26 to Figure 28).

Effective continuum parallel-plate apertures were calculated from the direction dependent transport porosities and the calculated equivalent parallel plate fracture spacing as indicated in equation (22). They are calculated in a way that preserves not only the surface area but also the transport porosity in a given flow direction in the DFNs. The equivalent parallel-plate apertures for the individual DFNs range from several hundred microns (4.1e-4 m) to several millimeters (mm) (6.1e-3 m). Equivalent parallel plate apertures in the Top-Bottom direction are slightly greater than in the North-South or East-West direction in the TSA and TCA due to the dominance of longer, more transmissive tectonic fractures cutting across the entire flow domain in the vertical direction. In the LFA, fracture apertures are similar for all three directions.

Table 5. Summary statistics for equivalent continuum parallel plate spacing and aperture.

	Spacing (m)			Aperture (m)		
	Top-Bottom	North-South	East-West	Top-Bottom	North-South	East-West
TSA						
Min	2.1	1.54	1.83	6.505E-04	4.368E-04	5.472E-04
Max	17.5	7.74	8.34	6.073E-03	2.844E-03	3.863E-03
Average	4.03	2.4	2.6	1.357E-03	7.361E-04	9.095E-04
Standard Deviation	2.36	1.01	1.24	8.634E-04	3.869E-04	5.836E-04
LFA						
Min	4.51	4.48	4.87	5.30E-04	4.19E-04	5.66E-04
Max	21.2	26.2	16.2	2.75E-03	3.01E-03	3.32E-03
Average	6.25	7.78	6.32	7.71E-04	8.48E-04	7.80E-04
Standard Deviation	2.77	4.43	1.92	0.000379484	0.00046767	0.000392493
TCA						
Min	5.01	3.55	2.7	7.717E-04	6.059E-04	4.231E-04
Max	38.5	26.3	18.3	5.300E-03	4.219E-03	5.181E-03
Average	14.4	8.73	6.23	2.130E-03	1.724E-03	1.369E-03
Standard Deviation	7.37	3.8	3.08	8.388E-04	7.604E-04	4.231E-04

a)

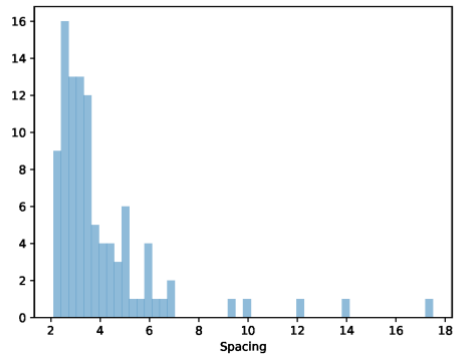

b)

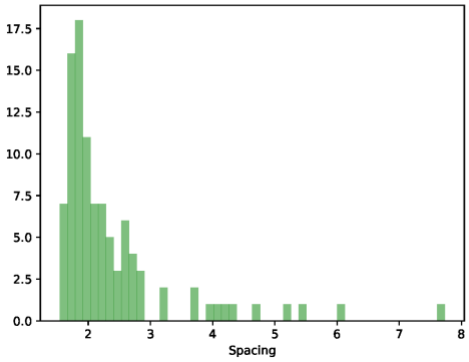

c)

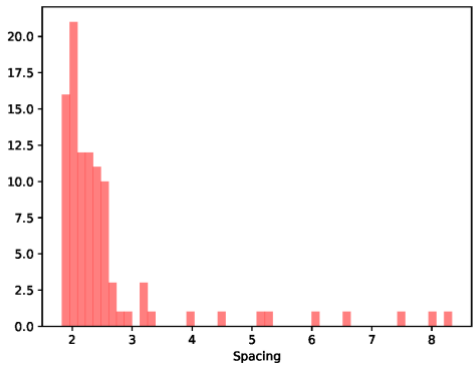

Figure 32 Histogram of fracture spacing (m) calculated for 100 DFN realizations of TSA: a) Top-Bottom; b) North – South; c) East-West.

a)

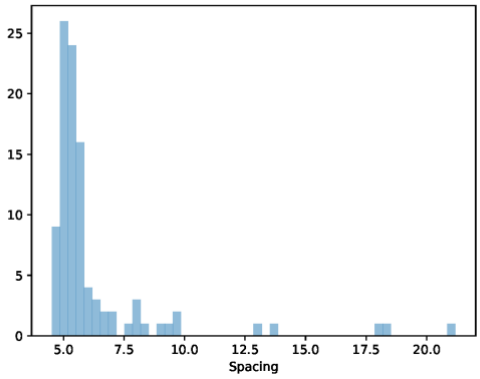

b)

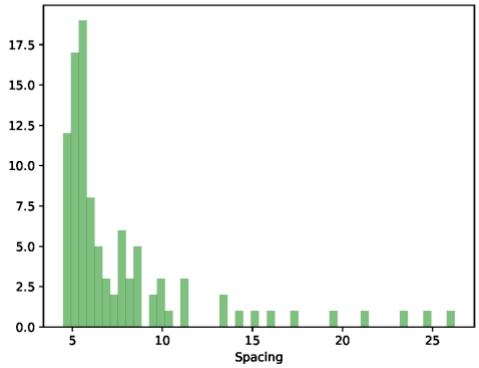

c)

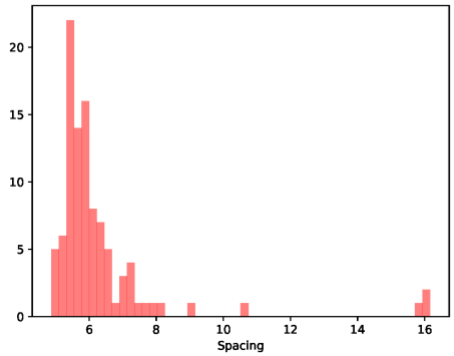

Figure 33 Histogram of fracture spacing (m) calculated for 100 DFN realizations of LFA: a) Top-Bottom; b) North – South; c) East-West.

a)

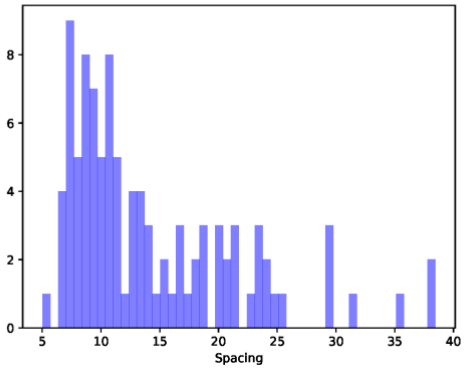

b)

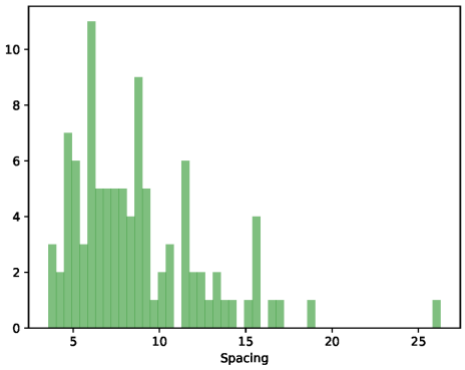

c)

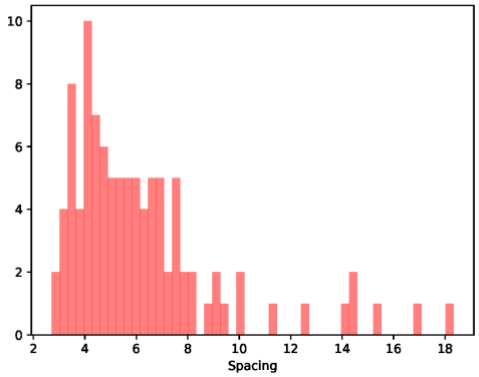

Figure 34 **Histogram of fracture spacing (m) calculated for 100 DFN realizations of TCA: a) Top-Bottom; b) North – South; c) East-West.**

a)

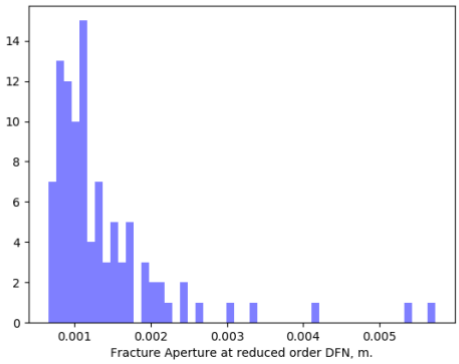

b)

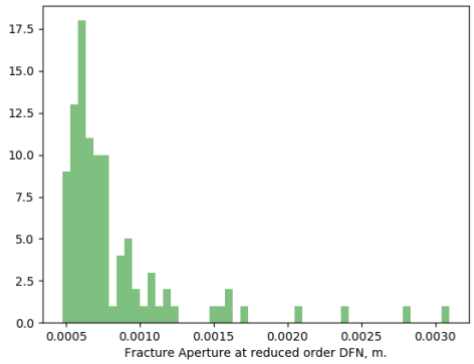

c)

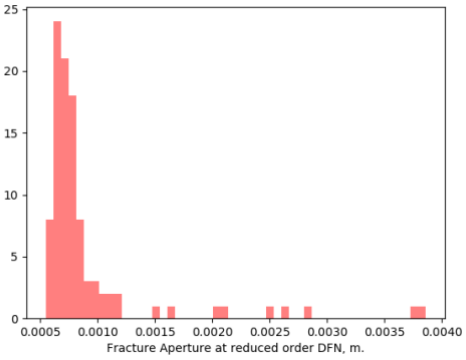

Figure 35 Histogram of fracture aperture calculated for 100 DFN realizations of TSA: a) Top-Bottom; b) North – South; c) East-West.

a)

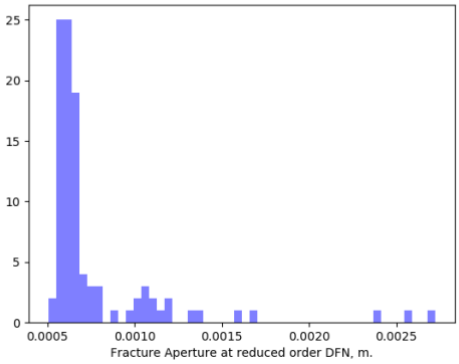

b)

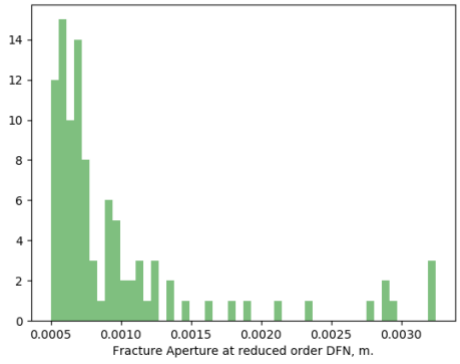

c)

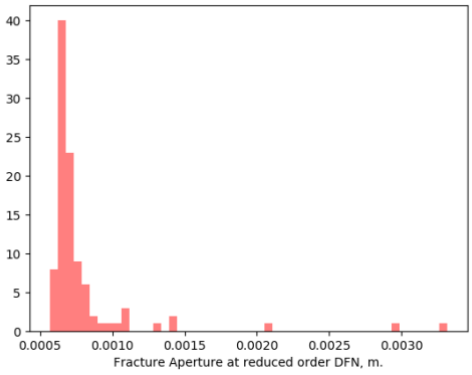

Figure 36 **Histogram of fracture aperture calculated for 100 DFN realizations of LFA: a) Top-Bottom; b) North – South; c) East-West.**

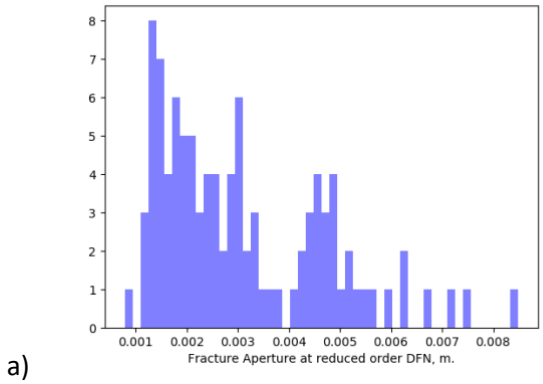

a)

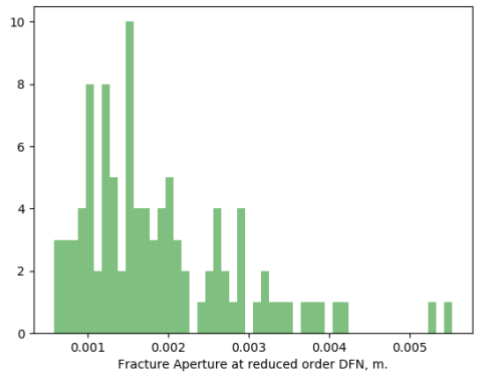

b)

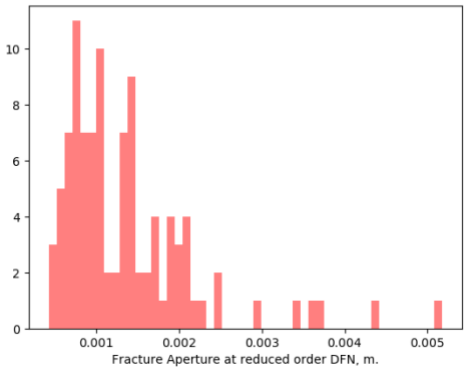

c)

Figure 37 Histogram of fracture aperture calculated for 100 DFN realizations of TCA: a) Top-Bottom; b) North – South; c) East-West.

4.4 Correlation Between Dispersivity and Fracture Network Intensity

Figure 38 shows the correlation between scaled dispersivity α/L (Section 4.2.4) and active fracture intensity P'_{32} (Section 4.3.1). The relationship between α/L and P'_{32} is linear in the TSA (Figure 38a), fit by power law curve in the LFA (Figure 38b), and exponential in the TCA (Figure 38c). Despite differences in the details of the correlation, the results indicate that to varying degrees, the fitted scaled dispersivity values increase, sometimes substantially, as the calculated P'_{32} values decrease. The relation between α/L and P'_{32} is strongest for Top-Bottom flow and transport in the LFA and TCA, and North-South flow and transport in the TCA. As discussed in Section 4.3.1, the active fracture network intensity P'_{32} is a measure of the degree of channelization within a fracture network, with smaller values indicating a larger degree of channelization in a few large, transmissive fractures and flow bypassing most of the remaining fractures. For DFNs with these characteristics, the particle breakthrough curves are characterized by both early particle breakthrough due to highly channelized flow and long tails because of limited flow and slow transport through the background fractures, resulting in large fitted dispersivity values. The largest fitted dispersivity values are probably among those discussed in Section 4.2.4 that had yet to reach their theoretical asymptotic limit and were still increasing at the downgradient end of the flow system.

a)

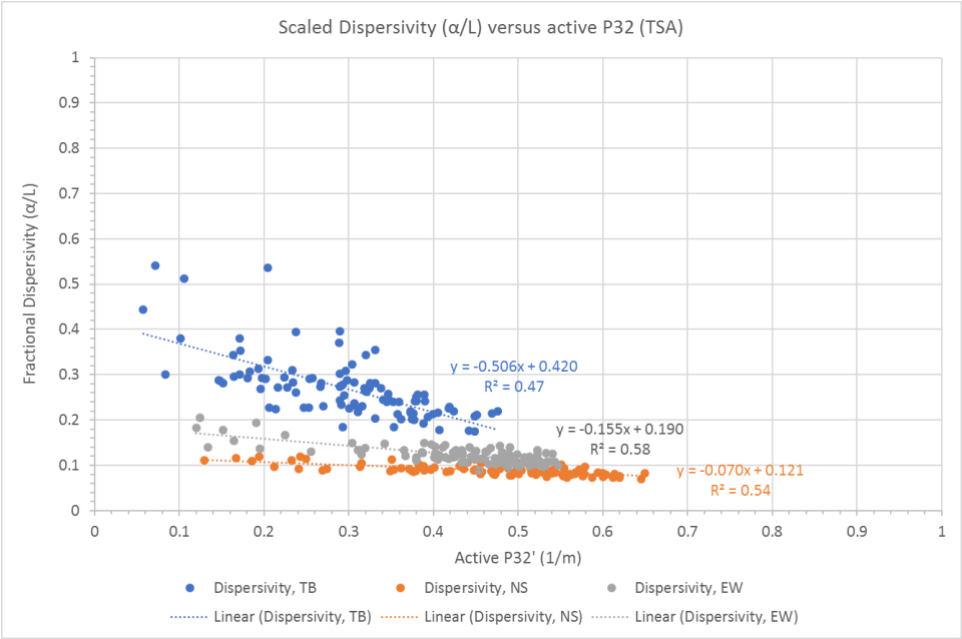
Scaled Dispersivity (α/L) versus active P32 (TSA)
Fractional Dispersivity (α/L)
Active P32' (1/m)
y = -0.506x + 0.420
R² = 0.47
y = -0.155x + 0.190
R² = 0.58
y = -0.070x + 0.121
R² = 0.54
Dispersivity, TB
Dispersivity, NS
Dispersivity, EW
Linear (Dispersivity, TB)
Linear (Dispersivity, NS)
Linear (Dispersivity, EW)

b)

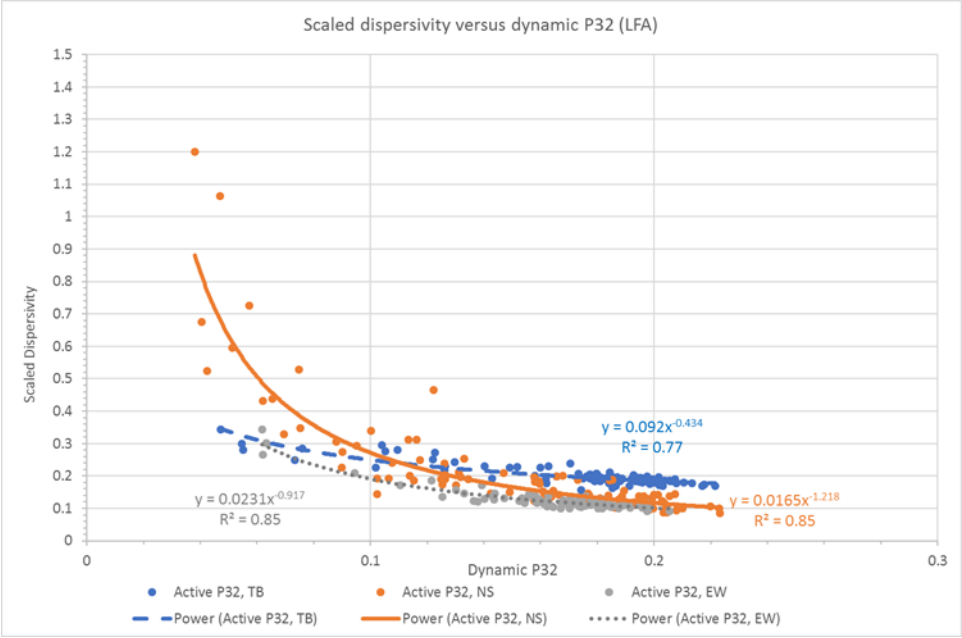
Scaled dispersivity versus dynamic P32 (LFA)
Scaled Dispersivity
Dynamic P32
y = 0.092x^-0.434
R² = 0.77
y = 0.0231x^-0.917
R² = 0.85
y = 0.0165x^-1.218
R² = 0.85
Active P32, TB
Active P32, NS
Active P32, EW
Power (Active P32, TB)
Power (Active P32, NS)
Power (Active P32, EW)

c)

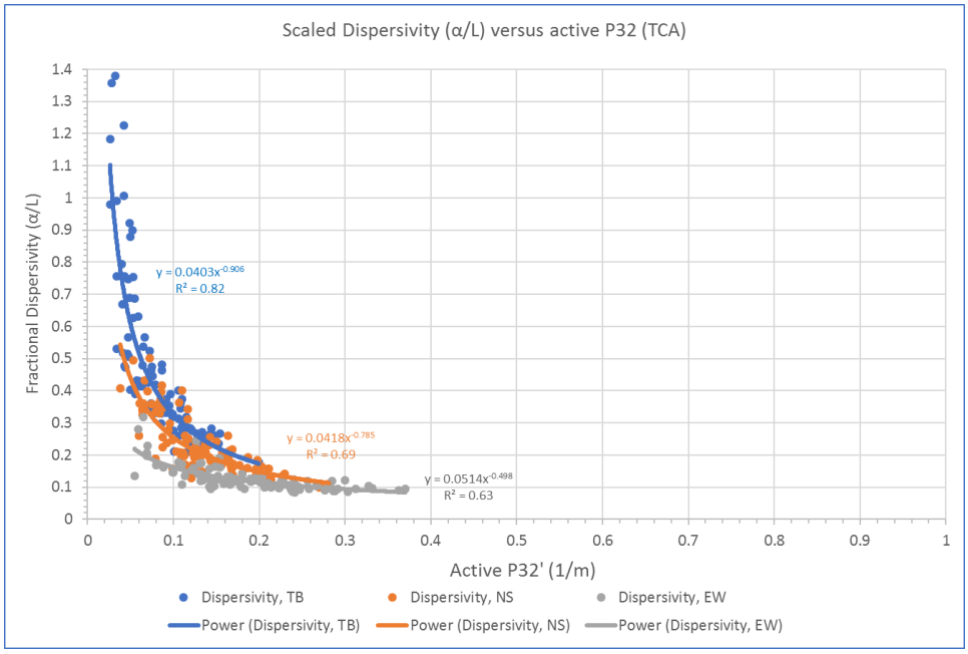

Figure 38 Correlation between scaled dispersivity (α/L) and active fracture network intensity, (P'_{32}) calculated in all three directions of flow for a) TSA; b) LFA; and c) TCA.

5 TESTING THE UPSCALING APPROACH

In this section, we test the upscaled parameters by first comparing breakthrough from the full DFN with a simplified parallel plate DFN having properties estimated from the full DFN. Then, we compare breakthrough from an equivalent continuum model that assumes matrix diffusion can be modeled using upscaled parameters and algorithms based on an equivalent parallel plate approximation such as those in widespread use in groundwater flow and transport codes such as FEHM.

5.1 Testing the Fracture Spacing and Fracture Aperture for a Parallel Plate DFN Model

A simple test is performed for a single DFN realization of TSA. The fracture spacing and fracture aperture for a simplified parallel-plate DFN model are calculated in the horizontal directions:

- North-South: 11 parallel horizontal fractures placed in simulation domain 250 x 250 x 100 m^3 with vertical spacing 9.08 m between fractures. Computational mesh is uniform, cell size is 10 m. Permeability of fractures is 9.239e-10 m^2; fracture aperture is 4.4050e-4 m.

- East-West: 10 parallel horizontal fractures placed in simulation domain 250 x 250 x 100 m^3 with vertical spacing 9.55 m between fractures. Computational mesh is uniform, cell size is 10 m. Permeability of fractures is 3.2229e-10 m^2; fracture aperture is 4.1255e-4 m.

Note that due to the difference in fracture spacing defined in the North-South and East-West examples, the different number of fractures, 11 and 10, are generated, keeping the same size of the simulation domain.

Figure 39 shows the obtained steady state flow solution for parallel plate DFN in North-South and East-West direction. Figure 40 shows simulated particle trajectories in parallel plate DFN.

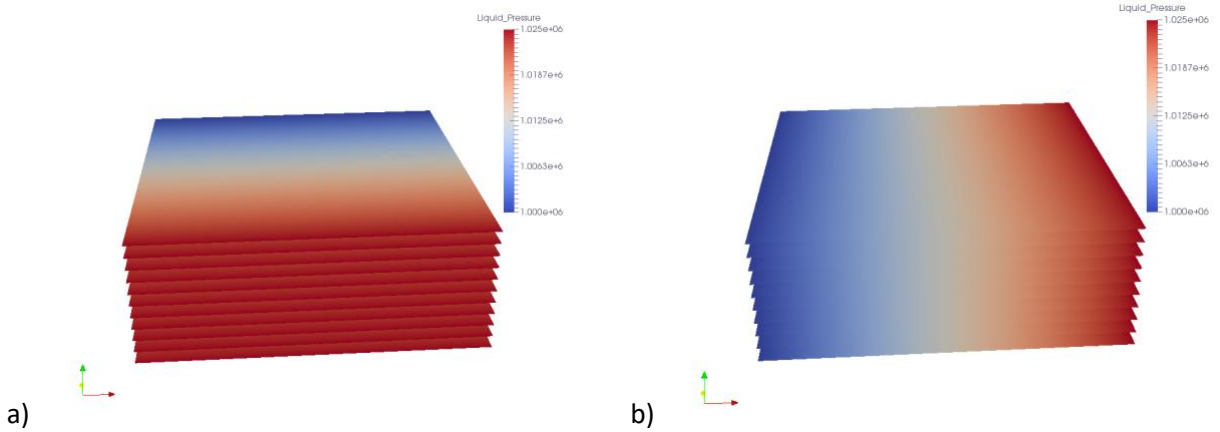

a) b)

Figure 39 Steady State pressure solution for fully saturated flow in parallel plate DFN. a) North – South; b) East-West direction of flow.

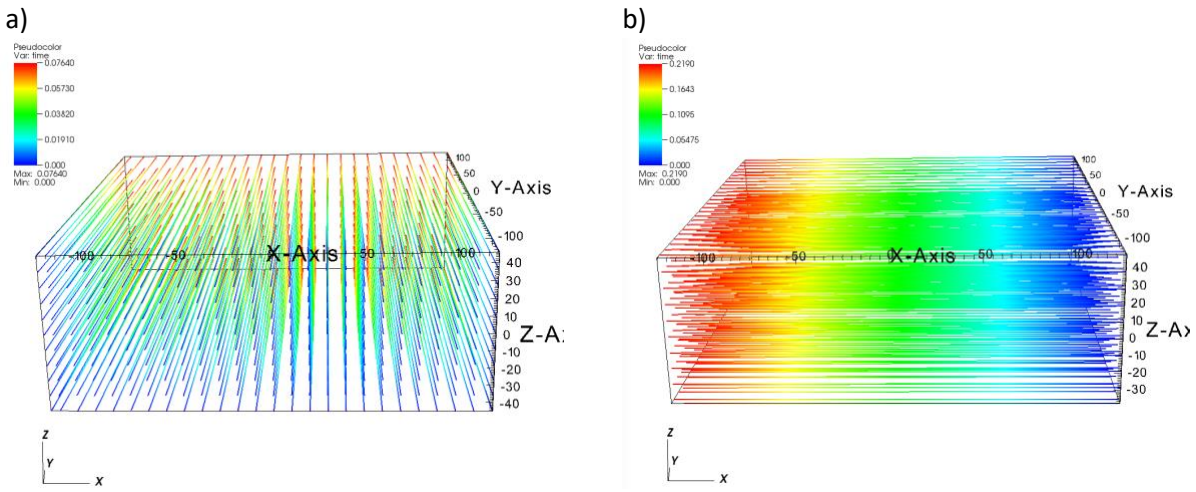

Figure 40 Particles trajectories in parallel plate DFN. Colors represent travel time of particles in the a) North – South and b) East-West direction of flow.

The particle's trajectories on parallel plate DFN are straight lines due to the fact that there are no intersecting fractures and no variability in fracture's orientations. A comparison of the BTC of transport simulated in full DFN with BTC of particles in parallel plate DFN is shown in Figure 41. Because the particle tracking capability in dfnTrans does not allow for dispersion, the particle breakthrough from the parallel plate DFN occurs all at once, whereas breakthrough from the DFN is dispersed because particles take different transport paths. However, the results of transport simulations in parallel plate DFN perfectly fit 50% of BTC obtained in DFN realization with complicated geometry, from which the dynamic intensity, fracture spacing and fracture aperture were calculated, providing a partial verification of the upscaled approach. A more complete test of upscaled parameters, including those that influence dispersion and matrix diffusion, is presented in the following section.

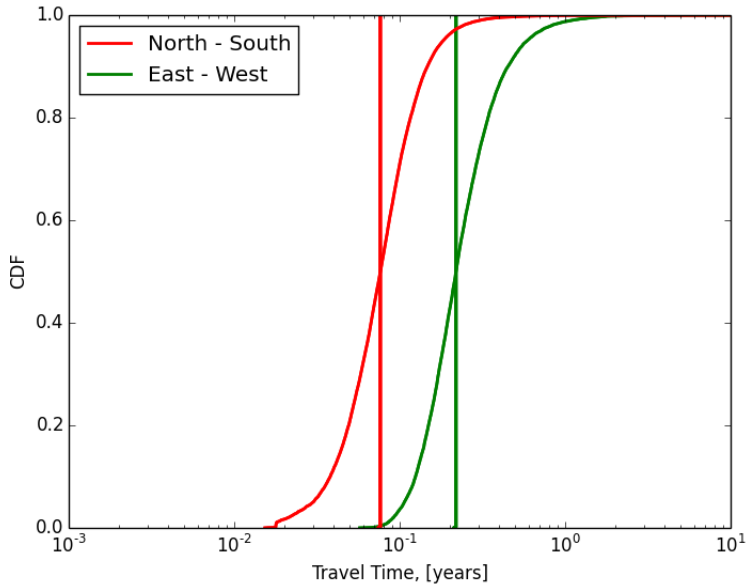

Figure 41 Comparison of breakthrough curves from a full DFN with breakthrough from a simplified DFN with fracture porosity, spacing and apertures calculated from the upscale parameters.

5.2 Testing the Upscaling Approach for an Equivalent Continuum Model

A test of the proposed approach for using upscaled parameters for use in an equivalent model was performed with and without matrix diffusion. The particle tracking breakthrough of one of DFN simulations of TSA is compared against an equivalent FEHM continuum model. The size of simulation domain of continuum model is the same as was used for DFN modeling: 250m x 250 m x 100m. FEHM uses aperture 2b = 220 µm and fracture spacing (s) of 4.5 m calculated from the P32' and porosity ϕ.

We implemented a rate-limited Time Domain Random Walk (TDRW) approach in DFN particle tracking modeling to account for diffusion of transported solutes into and out of the matrix surrounding the fracture network. The methodology is presented in detail in Hyman (2019) who tested the method against analytical solutions for matrix diffusion in simple, idealized fracture networks and in Hyman et al. (2020) who used the TDRW method to study the influence of matrix diffusion on the tailing behavior of particle BTCs. Conceptually, the method calculates and adds a delay to each particle's advective travel time in a fracture that depends on both the particle residence time in the fracture and on the diffusive properties of the rock matrix. The delay is calculated in such a way as to mimic the effects of diffusion into and out of the rock matrix. The distance a particle can move into the matrix is limited by the distance between primary flow channels in the DFN. In the DFN, the distance between flow channels is highly variable and difficult to calculate at a local scale in the DFN. As an approximation, the TDRW method uses half of the equivalent parallel-plate fracture spacing calculated in Section 4.3.2 as a representative value to approximate the maximum particle penetration depths. To summarize, in the TDRW method, the particle travel time (T_t) that a particle spends in one fracture is calculated as a sum of two terms: (1) the time that particles spends moving in fracture with fracture flow (T_{adv}), and (2) the time that particle spends in the matrix due to fracture-matrix diffusion, calculated with the second term on the right side of equation (24):

$$T_t = T_{adv} + \left[\frac{aT_{adv}}{erfc^{-1}(r)}\right]^2, where\ a = \frac{\varphi_m\sqrt{D_e}}{b} \quad (24)$$

T_{adv} is calculated at every time step using Darcy velocities at cell centers (for details in method, see [Makedonska et al. 2015]). The diffusion term is calculated at every fracture intersection and uses calculated T_{adv} accumulated at the same fracture. In equation (24), ϕ_m is a matrix porosity, D_e is a matrix diffusivity (m^2/s), b is a fracture half aperture (m), r is a random number from uniform distribution *(0,1)* that is used in the inverse complementary error function, $erfc^{-1}$.

To test the approach for calculating upscaled parameters for equivalent parallel plate flow and transport models, we performed the two sets of transport simulations in all three directions of flow for one DFN realization of the TSA:

1) Advective transport simulated by particle tracking in DFN and advective-dispersive transport by FEHM on equivalent continuum model.

2) Advection-diffusive simulations performed on DFN using TDRW approach and advection-dispersive-diffusive modeling by FEHM on an equivalent continuum model.

Figure 42 shows the comparison of transport breakthrough curves calculated directly from a DFN of the TSA with the results of an equivalent continuum model implemented in FEHM. The figure compares the results of breakthrough from the continuum model with the particle breakthrough from the DFN for all three directions and for cases that either ignore or include the effects of matrix diffusion. The cluster of curves that ignore matrix diffusion have complete breakthrough in under a year, whereas in the cases that include matrix diffusion, breakthrough is not complete for hundreds of years. The cases without matrix diffusion test the upscaling approach for calculating k, ϕ_t, and α. The cases that include matrix diffusion also test the upscaling approach for calculated aperture (2b) and fracture spacing (λ) as well as k, ϕ_t, and α.

For the cases without matrix diffusion, the continuum model with the upscaled k, ϕ_t, and α parameters (dashed curves) produces slightly earlier breakthrough than the actual DFN breakthrough (solid curves) for that direction. The continuum model results agree almost exactly with the breakthrough from the DFN model in the North-South direction, but are less exact for the East-West and Top-Bottom directions. However, even for the East-West and Top-Bottom directions, the differences are small in absolute terms: t_{50} is about 0.02 years for the equivalent continuum model and 0.07 years for the DFN in the Top-Bottom direction whereas t_{50} is about 0.2 years for the equivalent continuum model and 0.3 years for the DFN in the East-West direction. Although not exact, the differences in breakthrough from the DFN and from the equivalent continuum model are small in absolute terms, especially when considering the significant delay in particle breakthrough that occurs as a result of matrix diffusion.

The cases with matrix diffusion also test the equivalent parallel plate diffusion model and parameters, as well as the upscaled k, ϕ_t, and α parameters tested in the non-diffusive case. For these cases, the differences in t_{50} for the North-South and East-West breakthrough are relatively small: t_{50} is about 200 years for the equivalent continuum model and 150 years for the DFN in the North-South direction and 700 years for both the equivalent continuum and DFN models in the East-West direction. The DFN breakthrough shows more spreading (earlier breakthrough and later complete breakthrough) than results

from the equivalent continuum models, probably because there are a range of fracture apertures and block sizes in the DFN, whereas there is only a single aperture size and block size in the equivalent continuum model. Nonetheless, the equivalent continuum model does a fair job of reproducing the relative timing and magnitude of breakthrough of the DFN results for the North-South and East-West directions. In the Top-Bottom direction, t_{50} is about 40 years in the equivalent continuum model and 100 years in the DFN. Some of the discrepancy between the FEHM and DFN models for this case may be due to the earlier breakthrough in the FEHM model for the advection-only case.

Overall, the upscaled results capture the relative order of breakthrough in each of the three directions and the large shift in breakthrough times that occurs as a result of including matrix diffusion. More spreading (earlier initial breakthrough and later final breakthrough) is evident in the DFN breakthrough than calculated in the equivalent continuum model, probably as a result of the range of fracture apertures and block sizes that are included in the DFN and the assumed constant aperture and block sizes in the equivalent continuum model. In the Top-Bottom direction, there is relatively more difference between the DFN and equivalent continuum results. However, in large-scale models, the adjacent confining units are likely to control the amount of vertical flow across the TSA, LFA and TCA, so these differences will have no practical significance. The conclusion of the comparison is that the upscaled equivalent continuum model adequately reproduces the breakthrough from the more computationally intensive DFN in the North-South and East-West directions. However, as seen in Figure 42, there is also a strong directional dependence in the breakthrough behavior as a result of fracture properties that will far outweigh the much smaller differences between the DFN and equivalent continuum models results for a given direction.

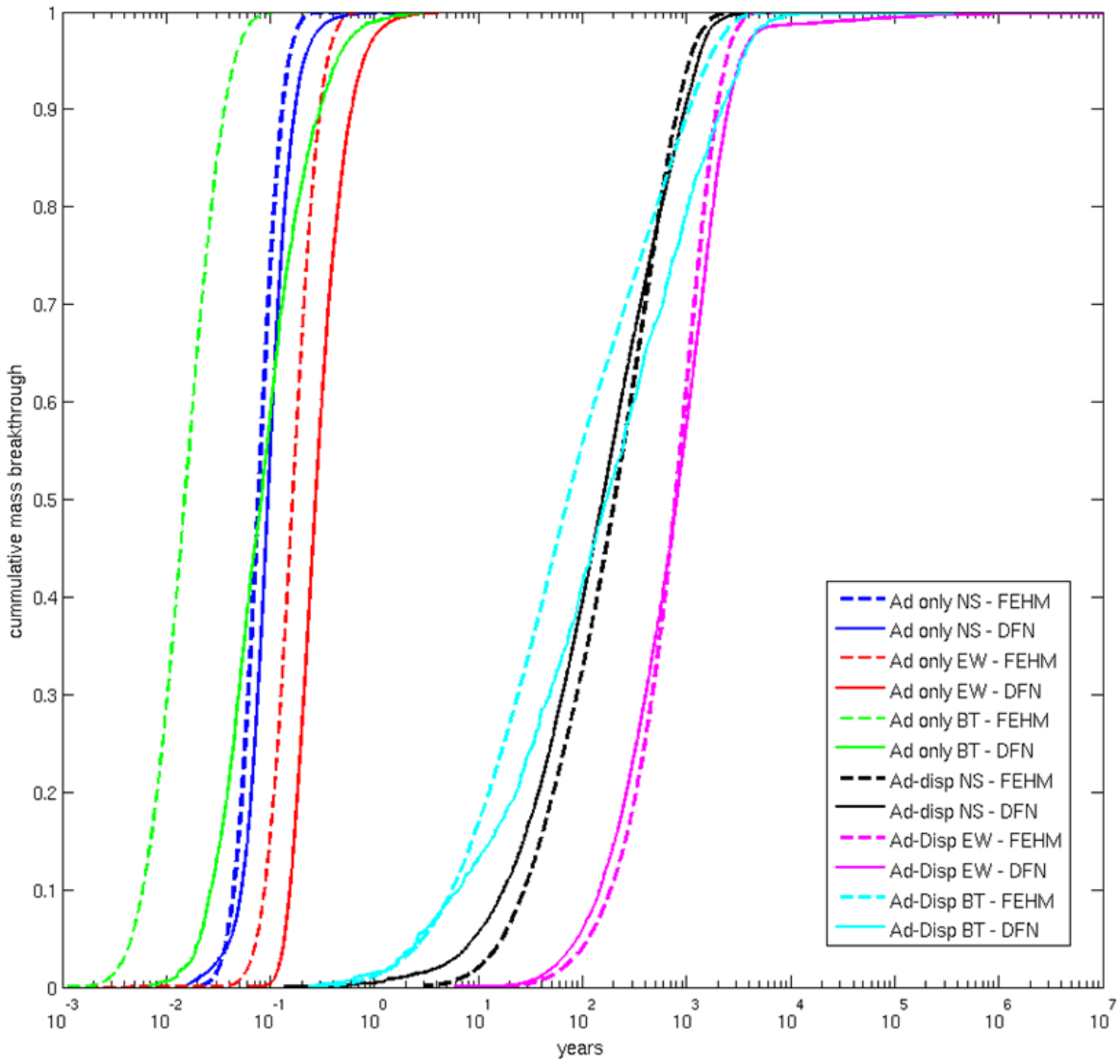

Figure 42 **A comparison of breakthrough obtained from DFN modeling with breakthrough from an FEHM equivalent continuum models run with upscaled parameters. Results are shown for all three flow directions both with and without matrix diffusion for one DFN realization of the TSA.**

6 DISCUSSION OF UPSCALED PARAMETERS FOR TSA, LFA, AND TCA OF PAHUTE MESA

In this section, we present the upscaled parameters for the TSA, LFA and TCA on a realization-by-realization basis and compare the upscaled values to parameter ranges calculated by Navarro (2019) using a 1-dimensional GOLDSIM model fitted to field observations of tritium concentrations. These tritium observations were made in the TSA and BA (a lava flow aquifer or LFA) in wells north of and along the Bench. The approach used by Navarro was to randomly draw parameters from assumed ranges for permeability and fracture spacing within each HSU, and calculate fracture aperture and effective transport porosity for the HSU using the cubic law. Those combinations of parameters that best fit the tritium observations were then retained. The parameter ranges, identified by Navarro as being consistent with the observed tritium concentrations, are shown in the figures 43-46 below for comparison with the upscaled parameter values calculated in this report. The GOLDSIM model considered a large (km) scale, where the pipe elements, which represented a single HSU, are greater than a km in length. Thus, some differences in the two sets of parameters could be expected because the GOLDSIM parameters rely on the cubic law and may also be incorporating the effects of larger-scale features such as faults that are not represented in the DFNs.

6.1 Effective Permeability

The upscaled permeabilities calculated for the TSA, LFA and TCA are typically at or below the lower end of the range of permeabilities identified by Navarro (2019) as being compatible with field-scale tritium measurements (Figure 43), but slightly higher than permeabilities determined from calibration to cross-hole pumping test responses by Garcia et al. (2017) shown by the dotted green lines in Figure 43.

In addition to these estimates, Jackson et al. (2019) analyzed historical single-well transmissivity data by HSU. For a given HSU, transmissivity data typically spanned many orders of magnitude; however, geometric mean transmissivity values, converted to permeability using a typical test interval length of 200 ft, were about 4e-13 m^2 for the TSA and 2.e-13 m^2 for the TCA. These values are very similar to the mean East-West and North-South permeability values of 4.1e-13 to 9.6e-13 m^2 for the TSA and 1.1e-13 to 3.5e-13 m^2 for the TCA listed in Table 4. Lavas, including the CHLFA1, CHLFA3, CHLFA4, CHLFA5 and the BA, ranged from about 2.e-14 to 4.e-13 m^2, comparable to the mean East-West and North-South permeabilities of 2.5e-13 and 3.6e-13 m^2 listed for the LFA in Table 4.

a)

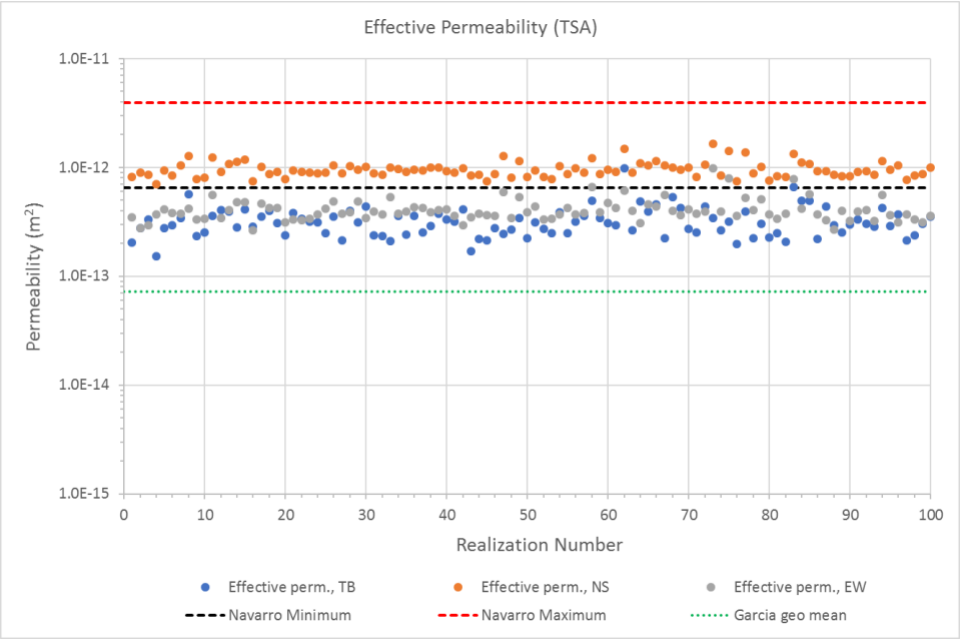
Effective Permeability (TSA)
1.0E-11
1.0E-12
1.0E-13
1.0E-14
1.0E-15
Permeability (m²)
0
10
20
30
40
50
60
70
80
90
100
Realization Number
Effective perm., TB
Effective perm., NS
Effective perm., EW
Navarro Minimum
Navarro Maximum
Garcia geo mean

b)

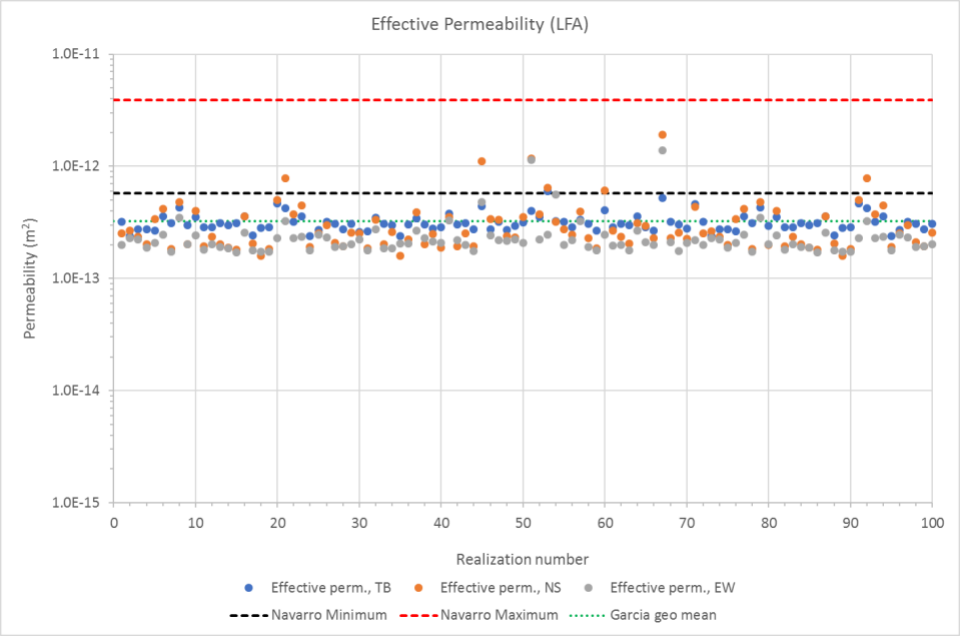
Effective Permeability (LFA)
1.0E-11
1.0E-12
1.0E-13
1.0E-14
1.0E-15
Permeability (m²)
0
10
20
30
40
50
60
70
80
90
100
Realization number
Effective perm., TB
Effective perm., NS
Effective perm., EW
Navarro Minimum
Navarro Maximum
Garcia geo mean

c)

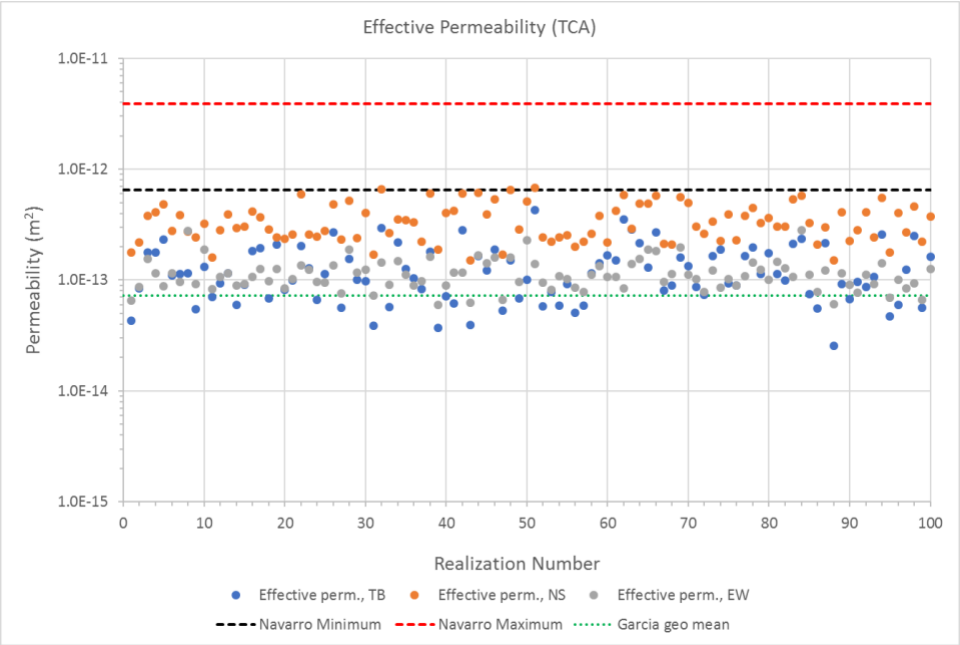

Figure 43 The comparison of effective permeability parameters calculated using DFN modeling (points) with the minimum (black dash line) and maximum (red dash line) values provided by Navarro team; a) effective permeability calculated for TSA; b) effective permeability calculated for LFA; a) effective permeability calculated for TCA. Also shown are the median values of permeability calculated from model calibration to cross-hole pump-test data by Garcia et al. (2017) (dashed green lines).

6.2 Transport and Volumetric Porosity

The upscaled transport porosities for the TSA identified from the DFN analysis plot toward the upper end of the range of transport porosities identified as compatible with the field-scale tritium data (Figure 44a). The transport porosities for the LFA and TCA plot near the middle of the ranges of transport porosities identified by Navarro (Figures 44b and 44c). For each aquifer, the total volumetric fracture porosity plot above the range of estimated transport porosities determined from the DFNs or field data, as would be expected based on the DFN transport model results.

a)

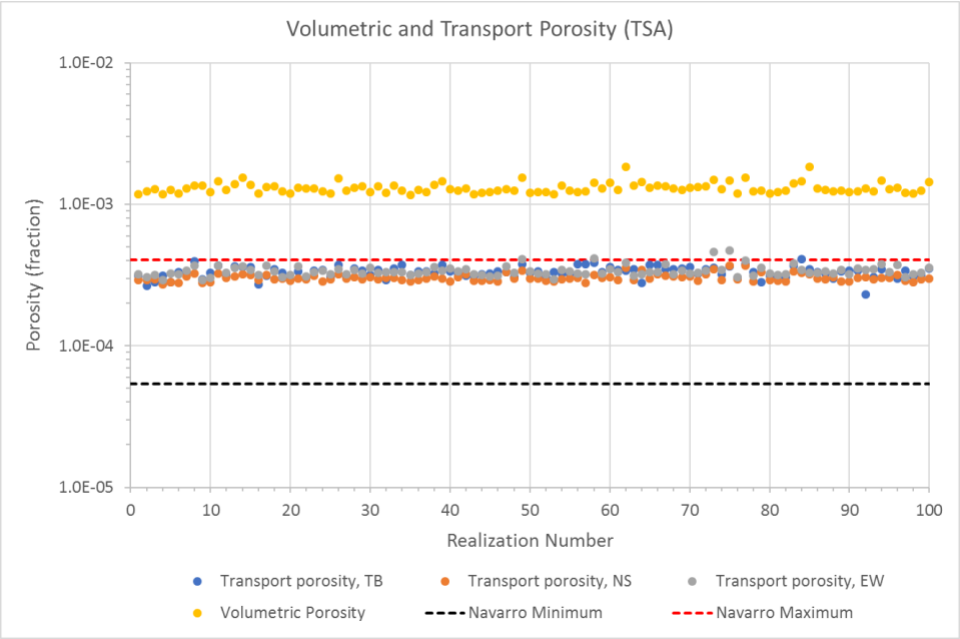
Volumetric and Transport Porosity (TSA)
1.0E-02
1.0E-03
1.0E-04
1.0E-05
Porosity (fraction)
0
10
20
30
40
50
60
70
80
90
100
Realization Number
Transport porosity, TB
Transport porosity, NS
Transport porosity, EW
Volumetric Porosity
Navarro Minimum
Navarro Maximum

b)

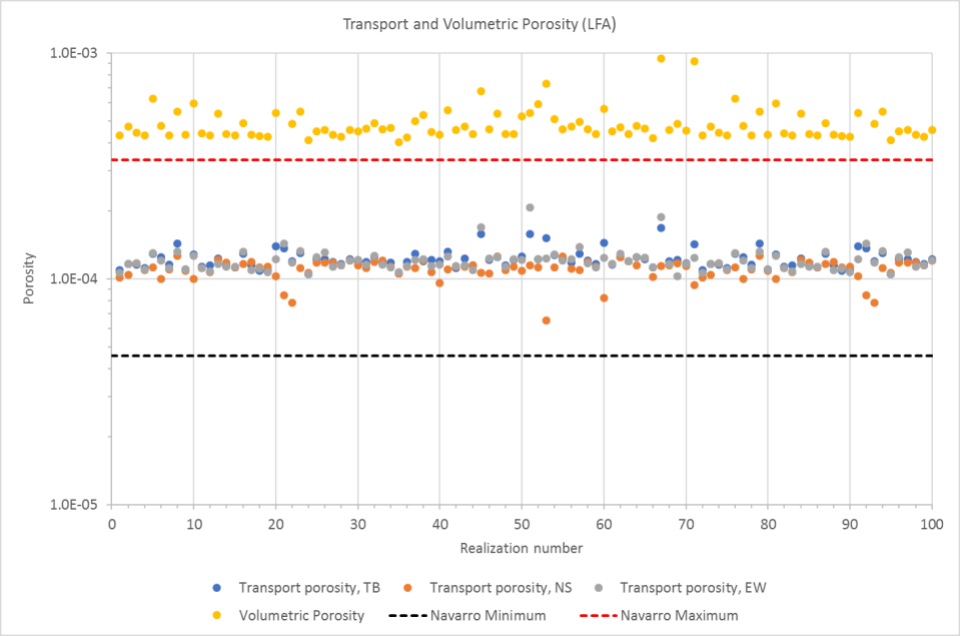
Transport and Volumetric Porosity (LFA)
1.0E-03
1.0E-04
1.0E-05
Porosity
0
10
20
30
40
50
60
70
80
90
100
Realization number
Transport porosity, TB
Transport porosity, NS
Transport porosity, EW
Volumetric Porosity
Navarro Minimum
Navarro Maximum

c)

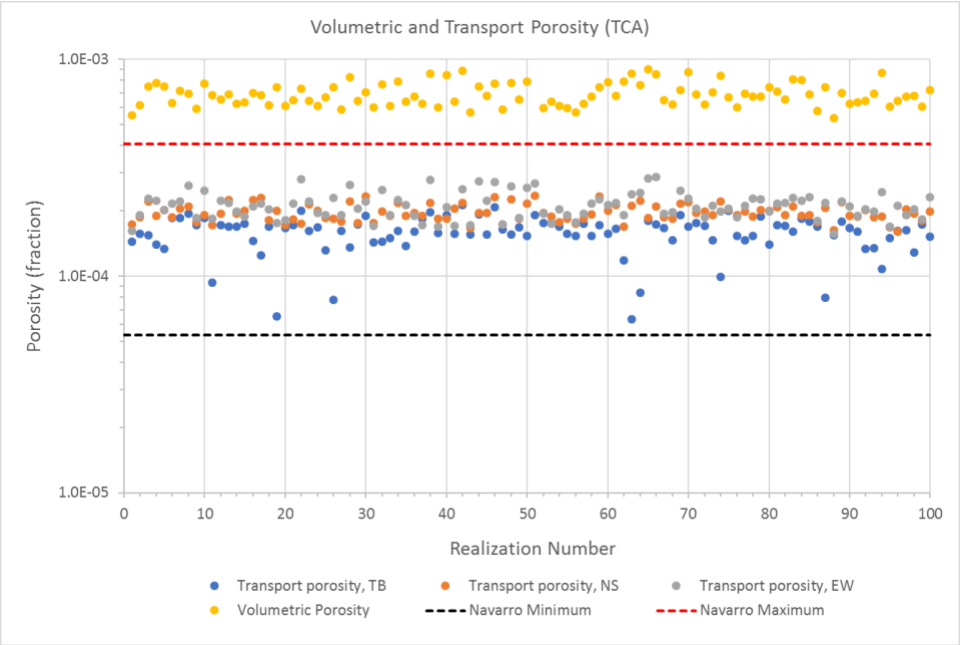

Figure 44 The comparison of effective volumetric and transport porosity calculated using DFN modeling (points) with the minimum (black dash line) and maximum (red dash line) values provided by Navarro team; (a) porosity calculated for TSA; (b) porosity calculated for LFA; and (c) porosity calculated for TCA.

6.3 Fracture Spacing

As indicated by Figure 45a, equivalent fracture spacing in both the North-South and East-West directions calculated from the DFN for the TSA is generally in the range of values estimated by Navarro from model fits to field tritium values. For a few realizations, the fracture spacing in the Top-Bottom direction is well outside the range estimated by Navarro for the horizontal direction. The same is also true for the LFA (Figure 45b), although a small number of realizations in the North-South direction also have very large fracture spacings, which reflects the presence of large, through-going north-south fractures in these realizations. In the TCA (Figure 45c), a substantial number of realizations in both the Top-Bottom and North-South directions have effective fracture spacings that are larger than the range of values identified by Navarro. The larger fracture spacings identified through the DFN analysis for the North-South direction are due to the preferred North-South orientation of long, tectonic fractures in the DFN which channelize flow and reduce the wetted surface area. The presence of large fracture spacings in the Top-Bottom direction of the TCA is also attributed to the dominance of just a few large tectonic fractures that cut across cooling unit boundaries and lithophysal zones where the cooling joints are discontinuous.

a)

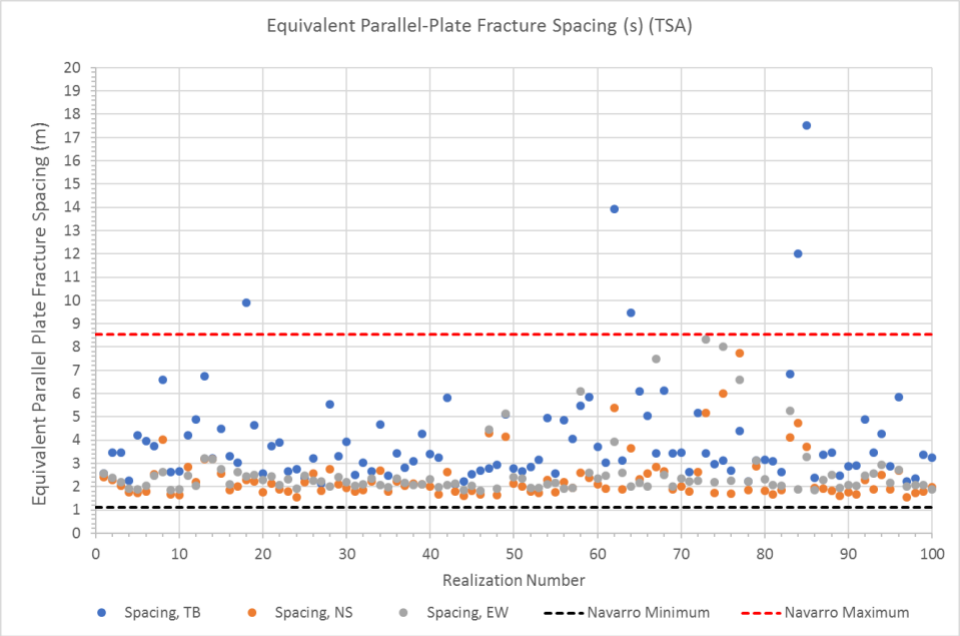
Equivalent Parallel-Plate Fracture Spacing (s) (TSA)
Equivalent Parallel Plate Fracture Spacing (m)
Realization Number
Spacing, TB
Spacing, NS
Spacing, EW
Navarro Minimum
Navarro Maximum

b)

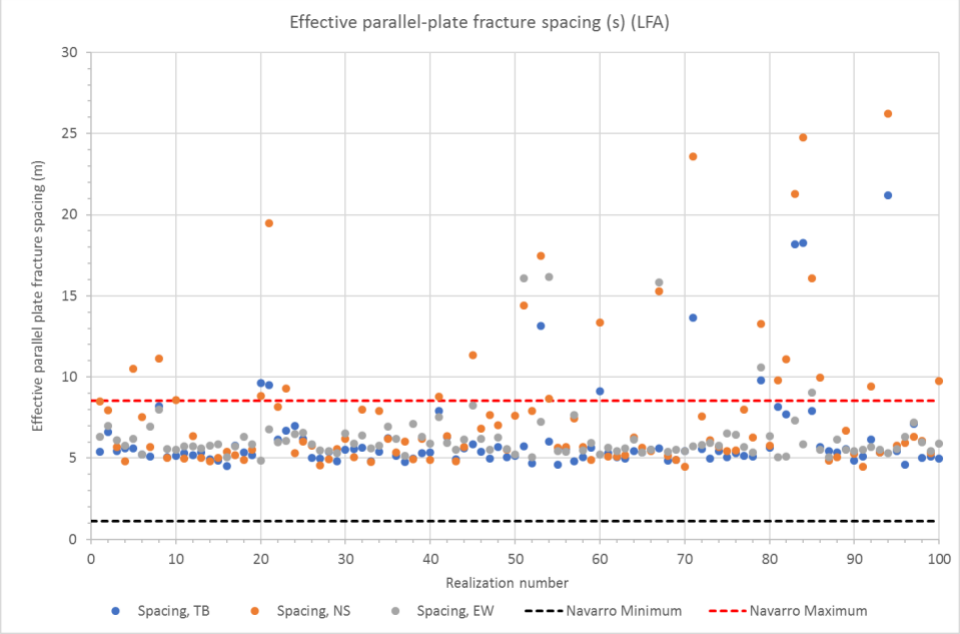
Effective parallel-plate fracture spacing (s) (LFA)
Effective parallel plate fracture spacing (m)
Realization number
Spacing, TB
Spacing, NS
Spacing, EW
Navarro Minimum
Navarro Maximum

c)

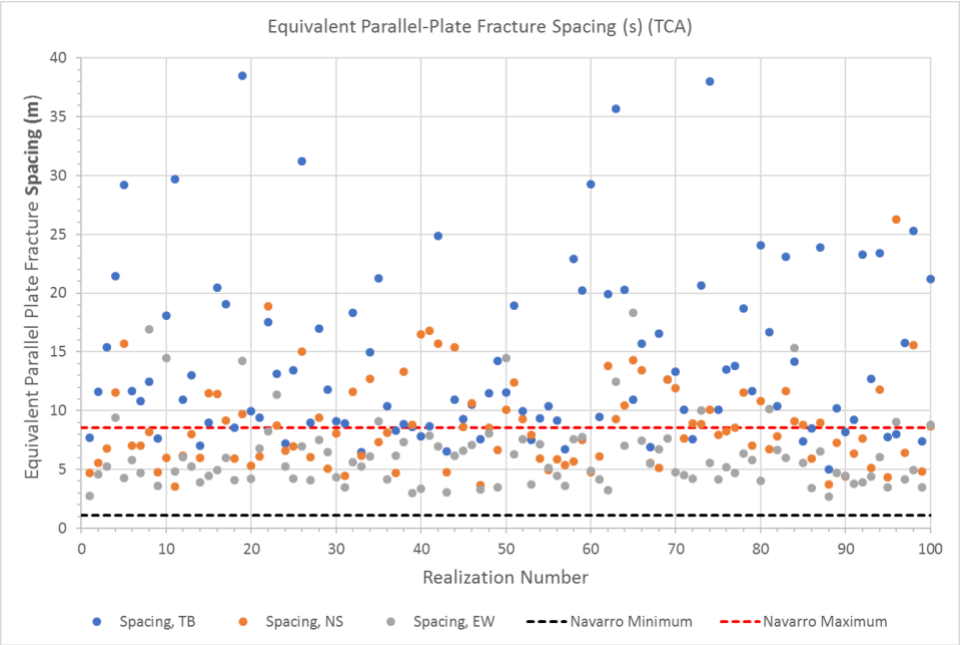

Figure 45 The comparison of fracture spacing using DFN modeling (points) with the minimum (black dash line) and maximum (red dash line) values provided by Navarro team (a) fracture spacing calculated for TSA; (b) fracture spacing calculated for LFA; and (c) fracture spacing calculated for TCA.

6.4 Fracture Aperture

In general, the equivalent parallel-plate fracture apertures calculated from the DFN models for the TSA, LFA and TCA plot in a band that is about twice the range of values identified by Navarro (2019) by fitting a 1-dimensional GOLDSIM model to the field-scale tritium data (Figure 46). This may reflect the modeling assumption in the DFNs that the mean physical aperture is a multiple (1 to 3 times) of the value of the hydraulic apertures calculated from the transmissivity versus length relationship defined by equation (1).

a)

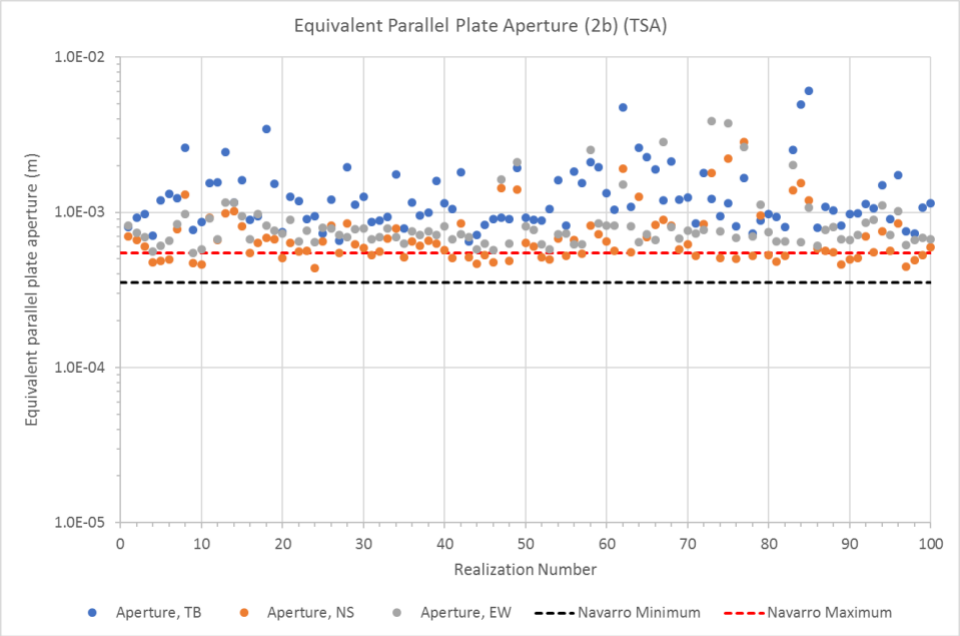
Equivalent Parallel Plate Aperture (2b) (TSA)
Equivalent parallel plate aperture (m)
1.0E-02
1.0E-03
1.0E-04
1.0E-05
0
10
20
30
40
50
60
70
80
90
100
Realization Number
Aperture, TB
Aperture, NS
Aperture, EW
Navarro Minimum
Navarro Maximum

b)

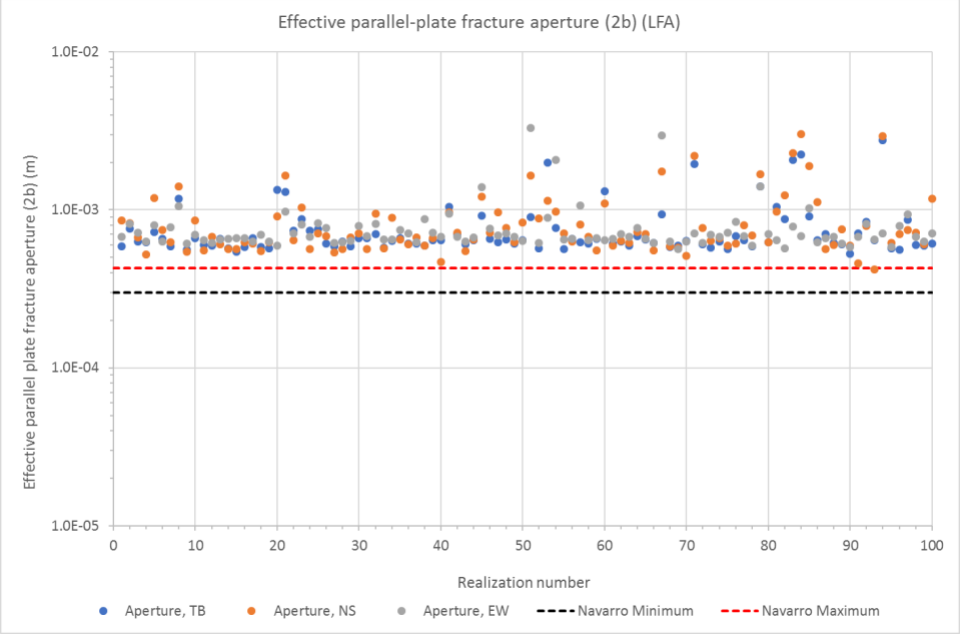
Effective parallel-plate fracture aperture (2b) (LFA)
Effective parallel plate fracture aperture (2b) (m)
1.0E-02
1.0E-03
1.0E-04
1.0E-05
0
10
20
30
40
50
60
70
80
90
100
Realization number
Aperture, TB
Aperture, NS
Aperture, EW
Navarro Minimum
Navarro Maximum

c)

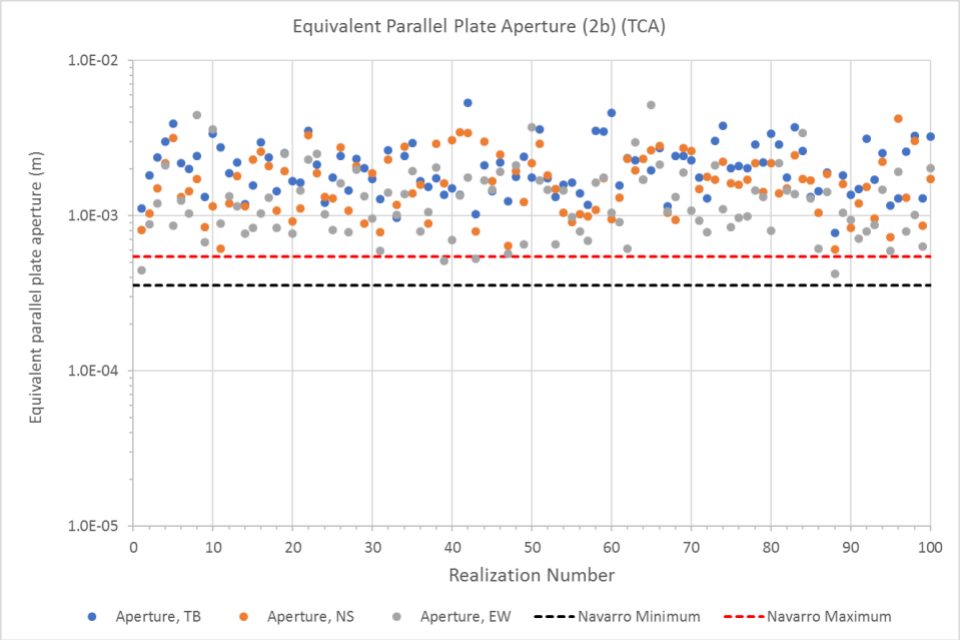

Figure 46 **The comparison of fracture aperture for equivalent parallel plate calculated using DFN simulations (points) with the minimum (black dash line) and maximum (red dash line) values provided by Navarro team; (a) fracture aperture calculated for TSA; (b) fracture aperture calculated for LFA; and (c) fracture aperture calculated for TCA.**

7 SUMMARY and CONCLUSIONS

Subsurface flow and contaminant transport through fracture networks representing the TSA, LFA and TCA at Pahute Mesa were simulated using the Discrete Fracture Network model, *dfnWorks*. One hundred independent DFN realizations were generated for each aquifer for a model domain of 250 x 250 x 100 m according to fracture characteristics acquired from field observations. A high-resolution numerical mesh was then created for each DFN for flow and particle tracking calculations. For each DFN, a steady state solution for fully saturated flow is obtained with PFLOTRAN in all three directions of flow (Top-Bottom, North-South, East-West) followed by Lagrangian particle tracking modeling to simulate solute transport. The upscaled parameters calculated from the steady-state flow and particle breakthrough results include directionally dependent permeabilities, transport porosities, dispersivities, and equivalent parallel-plate fracture apertures and spacing.

A novel approach was designed and implemented to calculate dynamic fracture network intensity (P'_{32}) to reflect flow channeling and is used to estimate fracture spacing and fracture aperture for an equivalent continuum model with a capability to simulate matrix diffusion for a set of parallel fractures. It was observed that fitted scaled dispersivities had a strong negative correlation with P'_{32}. For DFNs where flow and transport displayed strong channelization, indicated by low P'_{32} values, both early breakthrough through large transmissive fractures and slow transport through background fractures occurs, resulting in more dispersed particle breakthrough.

The Time Domain Random Walk (TDRW) capability has been added to the DFN particle tracking module *dfnTrans* to account for matrix diffusion into a finite half-space. Matrix diffusion significantly delayed particle breakthrough relative to the non-diffusive case.

A comparison of *dfnWorks* particle breakthrough for a realization of the TSA fracture network, both with and without diffusion, to an FEHM continuum model using the advection-dispersion equation, with or without a parallel-plate dual-porosity capability, demonstrates that the upscaled continuum parameters provide a good approximation to the DFN results at a fraction of the computational effort. The DFN particle tacking results did, however, show slightly more spreading (earlier initial breakthrough and longer tailing) than the equivalent continuum model using the advection-dispersion equation with matrix diffusion. The larger spreading in the breakthrough from the DFN is likely due to the wide range of fracture apertures and matrix block sizes in the DFN compared to the equivalent continuum model, where uniform apertures and fracture spacing are assumed.

A comparison between the upscaled permeability, transport porosities, and fracture spacing and apertures calculated from the DFN analysis with upscaled parameters previously obtained from 1D model fits to tritium plume migration at Pahute Mesa showed good agreement between the two sets of parameters. However, a successful comparison of the DFN results with the estimates based on field data required that the relationship between fracture transmissivity and length be modified from the original relationship defined by Golder (2014; 2015). The DFN models provide insight into the possible factors influencing transport through fracture networks conditioned on real-world observations from Pahute Mesa, such as flow channelization, and the upscaled parameters provide a starting point for estimating flow and transport parameters in both simple 1-D GOLDSIM models or more complex, large-scale three-dimensional flow and transport models of the Pahute Mesa groundwater system.

The DFN results for upscaled parameters the TSA, LFA and TCA have been generated at a scale (250 m x 250 m x 100 m) that may be relevant for regional groundwater flow and transport models with grid resolution at a comparable scale. However, depending on the aquifer, flow direction, and parameter of interest, the results may or may not be reflective of the parameter value at a theoretical Representative Elementary Volume (REV), which may, in fact, not exist in settings such as Pahute Mesa where heterogeneities exist at all scales. In hydrogeologic settings such as Pahute Mesa, larger models would inevitably incorporate larger-scale heterogeneities such as caldera boundaries, structural zones, and basin-and-range style faults, so that an REV might never be found. As described in Neuman (2005), these large-scale, mappable features are best represented as deterministic features in large-scale flow and transport models, whereas the DFN models presented here consider only smaller-scale features whose attributes are known only in a statistical sense, and hence, the stochastic nature of the DFN realizations. In the stochastic continuum framework described in Neuman (2005), the continuum parameters need not be scale-invariant, as expected if the domain equals or exceed the scale of the REV, so long as it is recognized that the upscaled values were calculated on a particular “support” (i.e. sample volume) and that the calculated parameter statistics pertain to that support. In the work presented here, the chosen support and resulting parameter variability are relevant to grid-scale variability in regional groundwater flow and transport models, so long as it is recognized that the upscaled parameters represent only the effects of features too small to map and that larger-scale features must be represented explicitly in the models.

8 ACKNOWLEDGEMENTS

This work was supported by the NNSS Underground Test Area Activity, administered by the U.S. Department of Energy, Environmental Management Office. Los Alamos National Laboratory is managed and operated by Triad National Security, LLC for the U.S. Department of Energy's National Nuclear Security Administration.

9 REFERENCES

Coxeter, H.S.M. (1969). Introduction to geometry. John Wiley and Sons, 216–221.

Fenelon, J.M., Halford, K.J., Moreo, M.T., 2016. Delineation of the Pahute Mesa–Oasis Valley groundwater basin, Nevada. U.S. Geological Survey Scientific Investigations Report 2015-5175, Version 1.1, 42 p.

Frampton, A., Hyman, J.D., and Zou, L. (2019). Advective transport in discrete fracture networks with connected and disconnected textures representing internal aperture variability. *Water Resources Research*, 55(7), 547-5501.

Garcia, C.A., T.R. Jackson, K.J. Halford, D.S. Sweetkind, N.A. Damar, J.M. Fenelon, and S.R. Reiner, 2017. Hydraulic characterization of volcanic rocks in Pahute Mesa using an integrated analysis of 16 multiple-well aquifer tests, Nevada National Security Site, 2009-14. U.S. Geological Survey Scientific Investigations Report 2016-5151.

Golder Associates (2014). Conceptual Model for Fracturing in the Topopah Springs Aquifer. Technical Memorandum developed for LANL.

Golder Associates (2015). Summary of Conceptual Model for Fracturing in Lava Flow Aquifers (LFA) at Pahute mesa. Technical Memorandum developed for LANL.

Hyman J. D., 2019. Verification of a Time Domain Random Walk Method to Include Matrix Diffusion into the High-Fidelity Three-Dimensional Discrete Fracture Network Simulations (submitted to ?)

Hyman J. D., Gable C. W., Painter S. L., and Makedonska N. (2014). Conforming Delaunay triangulation of stochastically generated three dimensional discrete fracture networks: A feature rejection algorithm for meshing strategy, *SIAM Journal of Scientific Computing*, 36(4), A1871–A1894.

Hyman, J.D., Jimenez-Martinez, J., Gable, C.W., Stauffer, P.H., and Pawar, R.J. (2020). Characterizing the Impact of Fractured Caprock Heterogeneity on Supercritical CO_2 Injection. *Transport in Porous Media*, 131(3), 935-955.

Hyman, J. D., Karra, S., Makedonska, N., Gable, C. W., Painter, S. L., & Viswanathan, H. S. (2015a). *dfnWorks*: A discrete fracture network framework for modeling subsurface flow and transport. *Computers & Geosciences,* 84, 10-19.

Hyman J. D., Painter S. L., Viswanathan, H. S., Makedonska, N., and Karra, S. (2015b). Influence of Injection Mode on Transport Properties in Kilometer-Scale Three-Dimensional Discrete Fracture Networks, *Water Resources Research*, DOI: 10.1002/2015WR017151.

Hyman, J., H. Rajaram, S. Srinivasan, N. Makedonska, S. Karra, H. Viswanathan, and G. Srinivasan (2019), Matrix diffusion in fractured media: new insights into power-law scaling of breakthrough curves, Geophysical Research Letters, DOI: 10.1029/2019GL085454.

Jackson et al. (2019) *Technical report in progress*

LaGriT (2013) *Los Alamos Grid Toolbox, (LaGriT)*, http://lagrit.lanl.gov, Los Alamos National Laboratory.

Lichtner P. C., Hammond G. E., Lu C., Karra S., Bisht G., Andre B., Mills R. T., and Kumar J. (2015). *PFLOTRAN user manual: A massively parallel reactive flow and transport model for describing surface and subsurface processes*, Technical report, Los Alamos National Laboratory.

Laczniak, R.J., J.C. Cole, D.A. Sawyer, and D.A. Trudeau (1996). Summary of hydrogeologic controls on ground-water flow at the Nevada Test Site, U.S. Geological Survey Water-Resources Investigations Report 96-4109, Carson City, Nevada.

Makedonska N., Painter S. L., Bui Q. M., Gable C. W., and Karra S. (2015). Particle tracking approach for transport in three-dimensional discrete fracture networks, *Computational Geosciences*, DOI: 10.1007/s10596-015-9525-4.

Makedonska, N., Hyman, J. D., Karra, S., Painter, S.L., Gable, C.W., and Viswanathan H. S. (2016). Evaluating the effect of internal aperture variability on transport in kilometer scale discrete fracture networks, *Advances in Water Resources* 94, p. 486-497.

Makedonska, N., Hyman, J. D., Kwicklis, E.M., Birdsell, K.H. (2018). Discrete Fracture Network Modeling and Simulation of Subsurface Transport for the Topopah Spring Aquifer at Pahute Mesa, *FY16-FY17 UGTA progress Report,* LA-UR-18-22264.

Makedonska, N., Gable, C. W., & Pawar, R. (2018a). Merging Discrete Fracture Network Meshes With 3D Continuum Meshes of Rock Matrix: A Novel Approach. In *2nd International Discrete Fracture Network Engineering Conference*. American Rock Mechanics Association.

Navarro (2019) *Technical report in progress*

Neuman, S.P., 2005. Trends, prospects and challenges of quantifying flow and transport through fractured rocks. Hydrogeology Journal v. 13, p. 124-147.

NSTec (draft November 2014). Phase II Hydrostratigraphic Framework Model for Corrective Action Units 101 and 102: Central and Western Pahute Mesa, Nye County, Nevada, DOE/NV/25946-xxx.

Painter S., Cvetkovic V., Mancillas J., Pensado O. (2008). Time domain particle tracking methods for simulating transport with retention and first-order transformation, *Water Resources Res*., 44.

Painter S., Gable C., Kelkar S. (2012). Pathline tracing on fully unstructured control-volume grids, *Comput. Geosci.*, 16, pp. 1125–1134

Painter, S., Mancillas, J., (2013). MARFA User's Manual: Migration Analysis of Radionuclides in the Far Field. *Posiva Working Report* 2013-01, Posiva Oy, Helsinki Finland

Pawloski, G.A. (1999). *Development of Phenomenological Models of Underground Nuclear Tests on Pahute Mesa, Nevada Test Site—BENHAM and TYBO*, UCRL-ID-136003. Livermore, CA: Lawrence Livermore National Laboratory.

Sauty, J. P. (1980). An analysis of hydrodispersive transfer in aquifers. *Water Resources Research*, *16*(1), 145-158.

Sherman, T., Hyman, J.D., Bolster, D., Makedonska, N., and Srinivasan, G (2019). Characterizing the impact of particle behavior at fracture intersections in three-dimensional discrete fracture networks. *Physical Review E*, 99(1), 013110.

SKB (2011), Long-term safety for the final repository for spent nuclear fuel at Forsmark, SKB TR-11-01. Swedish Nuclear Fuel and Waste Management Co., Stockholm.

SNJV (Stoller-Navarro Joint Venture). 2007. *Phase I contaminant transport parameters for the groundwater flow and contaminant transport model of Corrective Action Unit 97: Yucca Flat/Climax Mine, Nevada Test Site, Nye Counry, Nevada*, Rev. 0., S-N/99205-096.

Tsang, Y.W. 1992. Usage of “equivalent apertures” for rock fractures as derived from hydraulic and tracer tests. *Water Resources Research*, vol. 28, no. 5, p. 1451-1455.

U.S. Department of Energy, National Nuclear Security Administration Nevada Field Office, (2015). *United States Nuclear Tests, July 1945 through September 1992,* DOE/NV--209-REV 16. Las Vegas, NV

Zheng, Q., S.E. Dickson, and Y. Guo (2008). On the appropriate “equivalent aperture” for the description of solute transport in single fractures: Laboratory-scale experiments. *Water Resources Research*, vol. 44, W04502, doi:10.1029/2007WR005970.